NASA Graduate Student Fellowship NGT-30099-01
and NASA Grant NAG5-2692
National Aeronautics and Space Administration

THE VERTICAL STRUCTURE AND MODULATION OF TOGA COARE CONVECTION:

A RADAR PERSPECTIVE

by Charlotte A. DeMott

Steven A. Rutledge, P.I.

Colorado State University

DEPARTMENT OF ATMOSPHERIC SCIENCE

PAPER NO. **602**

THE VERTICAL STRUCTURE AND MODULATION OF TOGA COARE CONVECTION: A RADAR PERSPECTIVE

by

Charlotte A. DeMott

Department of Atmospheric Science

Colorado State University

Fort Collins, CO 80523-1371

Research Supported by

National Aeronautics and Space Administration

under Graduate Student Fellowship NGT-30099-01

and Grant NAG5-2692

April, 1996

Atmospheric Science Paper No. 602

ABSTRACT OF DISSERTATION

THE VERTICAL STRUCTURE AND MODULATION OF TOGA COARE CONVECTION:

A RADAR PERSPECTIVE

Tropical convection is an important component of the general circulation due to its role in driving large scale circulations which redistribute energy received at the equator to higher latitudes. The behavior of these large scale circulations is sensitive to the vertical distribution of diabatic heating produced by mesoscale precipitation systems, which are driven by precipitation formation processes. Convection that occurs in the western Pacific warm pool plays a particularly important role in driving large scale circulations such as the Walker circulation and the inter-annual El Niño-Southern Oscillation (ENSO), which is influenced by the 30-60 day intraseasonal oscillation (ISO).

Budget studies of diabatic heating profiles reveal two basic modes of heating: one with positive heating throughout the depth of the troposphere associated with convective precipitation, and another with positive heating in the upper troposphere and negative heating (cooling) in the lower troposphere associated with stratiform precipitation. Because stratiform heating profile shapes vary little from region to region and case to case, variations in total (convective plus mesoscale) heating profile shapes are thought to be linked to variations in the shape of convective heating profiles (Houze, 1989). However, long-term observations of convective vertical structures in the tropics—particularly the western Pacific warm pool—are either non-existent or limited to a few locations.

As a component of the recently completed Tropical Ocean Global Atmosphere (TOGA) Coupled Ocean-Atmosphere Response Experiment (COARE), the MIT 5-cm Doppler radar, mounted aboard the NOAA Research Vessel John V. Vickers, was deployed to a fixed location within the warm pool region for three approximately 30-day periods and continuously monitored the three-dimensional structure of

precipitating systems. In this study, radar data were partitioned into convective and stratiform components in order to address two main goals: 1) to determine the characteristic distributions of convective vertical structure during COARE and their variability over time, and 2) to relate observed variations of convective vertical structure to larger scale environmental variables.

Distributions of convective feature heights and 30 dBZ contour heights (an indicator of convective vigor) reveal that convective activity is modulated by the phase of the ISO as well as by intrusions of low-level dry subtropical air. However, at least some deep convection was nearly always present. The most intense convection—as observed by convective feature reflectivity profiles—occurred in environments with the greatest thermal buoyancy (the vertical distribution of CAPE) experienced by a parcel lifted from the mixed layer. However, these periods were also characterized by strong inhibitors to convective development which limited intense convective activity to just a few days. Convective heating profiles—computed from a combination of budget-derived total heating, radar-derived rainfall characteristics, and ideal and computed radiative heating profiles—varied in a manner consistent with the variations in vertical reflectivity and thermal buoyancy profiles. Namely, less vertically intense convection was associated with a lower altitude convective heating maximum than was observed for those days with convective reflectivity profiles indicative of more vigorous convection.

Possibilities for future research include a rigorous comparison of convective characteristics between the COARE and GATE regions, modeling studies of the influence of low-level dry air on convective activity and its relation to tropospheric drying, and testing a refinement of passive microwave rainfall retrieval algorithms.

Charlotte A. DeMott
Atmospheric Science Department
Colorado State University
Fort Collins, CO 80523
Spring 1996

ACKNOWLEDGMENTS

I would like to thank my advisor, Dr. Steven A. Rutledge, for his guidance and patience during my time as his student. I would particularly like to thank him for giving me the opportunity to participate in TOGA COARE—the insights and motivation derived from that experience have been enormously useful. I would also like to gratefully acknowledge the assistance of and numerous discussions with Dr. Richard Johnson, Xin Lin, and Paul Ciesielski concerning the construction and interpretation of the interpolated sounding data set. This work benefited from discussions with my fellow students Rob Cifelli, Walt Petersen, Terry Schuur, and Tom Rickenbach.

I also thank my father for kindling my interest in science and technology, and my mother for encouraging me to push the limits of my academic abilities. Finally, I thank my wonderful husband, Paul, and daughter, Maggie, for giving my life balance and meaning as I pursued this degree. No matter how good or bad the day at work was, it always got better when I came home.

This work was supported by NASA Graduate Student Fellowship #NGT-30099-01 and NASA grant #NAG5-2692.

TABLE OF CONTENTS

LIST OF TABLES

LIST OF FIGURES

Chapter 1

INTRODUCTION

1.1 Motivation

The process of redistributing radiant energy that is intercepted at tropical latitudes about the globe is one of the most long-standing, intriguing and complex problems faced in understanding global circulations. In simplest terms, most of the earth's incoming solar radiation is intercepted at tropical latitudes which heats the moist tropical boundary layer. This heating results in convection which then heats the tropical atmosphere, primarily through the release of latent heat. Although convection occurs at all tropical longitudes, it is concentrated at three preferred longitudinal areas: the equatorial regions of the African continent, the Amazon Basin, and the broad Maritime Continent and Western Pacific warm pool region, together spanning from approximately 100°E to 160°E. This non-uniform heating of the tropical atmosphere results in global scale circulations, such as the longitudinal Walker and latitudinal Hadley circulations. The strength and relative locations of these circulations with tropical origins affect the general circulation of the entire globe. Therefore, factors that influence the behavior of these tropical circulations are of interest in the study of the earth's entire general circulation.

One of the outstanding problems of tropical meteorology is understanding the interactions of tropical circulations over a large range of temporal and spatial scales. For example, most of the diabatic heating in tropical latitudes is accomplished by mesoscale convective systems, or MCSs (Houze, 1982). These systems are dominated by both meso- and convective-scale circulations, but their resultant heating profiles affect synoptic and larger scale circulations. Furthermore, the vertical structure of the heating profile, which is in part dependent on MCS vertical velocities, moisture contents, and microphysics, can

have a substantial impact on large scale tropical circulations (Hartman *et al.*, 1984; DeMaria, 1985; Lau and Peng, 1987).

Recognizing the role of MCSs in tropical circulations, many authors (i.e., Yanai *et al.*, 1973; Houze, 1982; Johnson and Young, 1983) have studied how MCS convective and mesoscale components influence the system-total heating. In general, mesoscale heating (associated with stratiform precipitation) enhances the upper level convective heating maximum but diminishes lower level heating through melting and evaporative cooling. To a first approximation, the overall shape of an MCS heating profile is determined by the relative amounts of convective and mesoscale heating, which are proportional to the relative amounts of convective and stratiform precipitation. However, convective and stratiform precipitation produce heating profiles that may vary both in magnitude and in the vertical distribution of heating and/or cooling. These variations on the basic MCS convective/stratiform partition will influence the vertical shape of the heating profiles and thus impact the larger scale circulations.

In addition to diabatic heating, MCSs also exert a strong influence on radiative heating profiles, particularly the stratiform cloud component of these systems (Webster and Stephens, 1980). For example, Ackerman *et al.* (1988) have demonstrated radiative heating rates as high as 20 to 30 K/day in tropical anvil clouds, which may be a source of turbulence (Lilly, 1988). Furthermore, Gray and Jacobson (1977) have argued that differences between clear-air and in-cloud radiative heating rates lead to the diurnal modulation of tropical rainfall.

Variations in the vertical distributions of diabatic and radiative heating profiles may both be discussed in terms of microphysical processes and other properties of the MCS. Positive diabatic heating results from various combinations of condensation, deposition, and freezing (riming) associated with rainfall production, while diabatic cooling is caused by melting, evaporation, and/or sublimation. Therefore, processes that lead to enhanced ice processes in convective precipitation will lead to more heating in the middle and upper levels of the systems, while systems characterized by significant condensation below the freezing level should have more heating concentrated in the lower levels. These variations in the convective region may also affect stratiform precipitation, since stratiform precipitation results either from decaying convection (Leary, 1984), or is formed when ice particles are ejected from

convective towers, giving rise to precipitating anvil clouds (Rutledge and Houze, 1987). These same convective-stratiform interactions also impact the radiative heating profiles by changing the optical properties and total water paths experienced by the radiant energy as it passes through the system. For example, Wong *et al.* (1993) have shown that systems with stratiform anvils characterized by decaying convective elements and high hydrometeor mixing ratios result in stronger mid-level net heating than those with anvils characterized by lower hydrometeor mixing ratios.

Observations of the distribution of convective and stratiform rainfall, the vertical distribution of heating associated with these two rainfall types, and radiative properties of tropical MCSs have come primarily through field programs such as the GARP (Global Atmospheric Research Program) Atlantic Tropical Experiment (GATE), Winter and Summer Monsoon Experiment (MONEX), the Australian Monsoon Experiment (AMEX; Holland *et al.*, 1986), the Equatorial Monsoon Experiment (EMEX; Webster and Houze, 1991), the Stratosphere-Troposphere Exchange Program (STEP), the Taiwan Area Mesoscale Experiment (TAMEX; Cunning, 1988; Jorgensen and LeMone, 1988), the Down Under Doppler and Electricity Experiment (DUNDEE; Rutledge *et al.*, 1992), and the Tropical Ocean Global Atmosphere Coupled Ocean-Atmosphere Response Experiment (TOGA COARE; Webster and Lukas, 1992). These field programs have provided detailed information on tropical MCS structure and its variability over spatial scales extending up to thousands of kilometers and ranging up to several months in time. The expense and logistics of these programs, however, prohibit extension of these types of observations to larger areas or greater time periods. The result is highly detailed observations of phenomena occurring within the study area and time frame, but insufficient data over annual cycles and limited sampling of intraseasonal oscillations.

To fill in some of these gaps in our knowledge, the Tropical Rainfall Measuring Mission (TRMM; Simpson *et al.*, 1988) is the first large-scale project designed to assess the amount and variability of tropical rainfall from a space-borne platform. Equipped with an array of passive and active microwave sensors and other remote sensing devices, the TRMM payload will allow researchers to construct a climatology of tropical rainfall from 35°S to 35°N and over a period of approximately three years. In

addition to estimating rainfall, TRMM seeks to improve knowledge of the vertical distribution of precipitation and, more importantly, the inferred heating arising from the distribution. The orbital characteristics of the satellite will be such that each 5×5 degree grid box within the sampling domain will be visited at least twice during each hour of the day over an approximately one-month period (Shin and North, 1987). This arrangement allows the variability of rainfall to be studied over diurnal, intraseasonal, and annual time scales.

While the TRMM project has the advantage of large area and time sampling, it's principal challenges will be 1) remote estimation of rainfall and 2) using this information to infer the vertical structure of heating. Many algorithms being designed to estimate rainfall rely on the TRMM Microwave Imager (TMI) since its five wavelengths can be used to infer a "profile" of precipitation. Recent advances in the understanding of how upwelling microwave radiation interacts with both liquid and ice cloud elements have allowed the development of several sophisticated rainfall retrieval algorithms (e.g., Olson, 1989; Smith *et al.*, 1992; Kummerow and Giglio, 1994). A shortcoming that is common to all of these algorithms, however, is insufficient knowledge of the vertical structure of tropical precipitating systems. While some work has been done concerning the vertical structure of individual convective systems (Szoke *et al.*, 1986; Rutledge *et al.*, 1992; Zipser and Lutz, 1994), little is known about the overall vertical structure of tropical MCSs (i.e., the vertical distribution and phase of both cloud and precipitation particles) and how these structures may vary with time (for example, over the course of 3-5 day easterly waves, or monthly time scales associated with the intraseasonal oscillation).

The research described in this dissertation has several specific objectives, all aimed at improving our knowledge of the vertical structure (and its variability) of tropical precipitation. The objectives of this work are:

1. Radar echo characteristics

    a) What is the shape of the mean convective and stratiform reflectivity profiles during the COARE Intensive Observing Period (IOP)?

b) What is the distribution of convective features during COARE by area, height, and 30 dBZ contour height (an indicator of convective vigor)? What is the distribution of rainfall production by these features?

c) How do these distributions vary with time?

2. Relationship to large-scale flow and heating profiles

a) What large-scale variables are correlated to surface rainfall and convective vertical structure?

b) What factors modulate variations in convective vertical structure?

c) How do observed variations in vertical structure relate to variations in diabatic heating profiles?

Results of previous studies describing the characteristics and vertical structure of tropical convection are summarized in the remainder of this chapter, while studies of the modulation of convective activity and its relationship to large-scale flow will be discussed in the sections of the thesis that address these topics. An overview of the TOGA COARE field program and a discription of the data and analysis methods used in this study are discussed in Chapter 2. Distributions of convective features, their vertical structure, and rainfall production are presented in Chapter 3. Variations in rainfall production and vertical structure in terms of large-scale observables and its relation to diabatic heating profiles are discussed in Chapter 4, and a summary and discussion of future research is presented in Chapter 5.

1.2 Scientific background

Studies of the vertical structure of tropical convection first arose from efforts to describe the overall structure of MCSs in statistical terms. It was hoped that these statistical descriptions of precipitating systems could be used to improve convective parameterizations in general circulation models. Early efforts during the 1970's focused on describing the horizontal distribution of radar echoes, while the vertical structure was often addressed in terms of the distribution of echoes by height. Later work (late 1970's to mid-1980's) concentrated on separating convective echo from stratiform echo and

assessing the relative amounts of rainfall associated with each precipitation type, as well as the distribution of rainfall by convective cloud top heights. In the mid-1980's, studies of convective vertical updraft velocities in tropical systems revealed updraft speeds noticeably weaker than those found in mid-latitude systems of similar depth, suggesting fundamental differences between the vertical structure of MCSs in these two regimes. In the late 1980's through the present, efforts have focused on developing conceptual models of tropical convection that are consistent with observations of vertical updraft speeds, microphysical characteristics, and lightning production. This section describes some of the findings of this body of work.

Summarizing results from several previous studies, Lopez (1977) discussed the lognormal distribution of radar echo heights, horizontal dimensions and durations observed in several different geographic locations. This distribution reflects the fact there are large numbers of shallow, small, and short-lived echoes and that the number of features decreases with increasing depth, area, and lifetime. Houze and Cheng (1977) presented similar findings for radar echoes studied during GATE, as well as how these distributions varied over the summer season. They also reported that the number and size of convective "cores" embedded within large echo structures increased with increasing echo area. In each of these studies, no attempt was made to discriminate between convective and stratiform rainfall.

Leary and Houze (1979a) described the evolution of a tropical MCS observed during GATE in terms of the interactions between convective elements and stratiform rainfall. The formative stage is characterized by discrete but linearly organized convective cells. During the intensifying stage, the individual cells merge to form a continuous line. At this stage, an anvil cloud forms as a result of hydrometeors being detrained from the cloud tops, but it produces no precipitation. During the mature stage, the influence of convective elements on the stratiform cloud deck is at its greatest. This stage is characterized by new convective elements forming at the "leading edge" of the system, a process which is partly responsible for the propagation of the system. Older cells then decay behind the leading line and become part of the stratiform cloud deck. Sometime during the mature and dissipating stages, the stratiform cloud deck develops a mesoscale circulation pattern distinct from that associated with decaying convective cells. As hydrometeors fall through the freezing level and experience melting and evaporation,

a broad area of low-level descent develops. Above the freezing level, the release of latent heat through depositional growth results in a broad area of weak ascent.

In an effort to separate the effects of stratiform rain on radar echo statistics, Cheng and Houze (1979) divided 4×4 km gridded GATE radar echoes into convective and stratiform populations using a set of subjective guidelines. They estimated that approximately 40% of the rainfall during GATE was stratiform. They also examined the contribution of convective rainfall by echoes of various heights and found that only a small portion of the convective rainfall originated from echoes less than 5 km in depth. Most of the rainfall was associated with echo heights between 10 and 13 km, with a secondary peak associated with "overshooting tops" near the 16 km level.

Leary (1984) used the partitioning rules of Cheng and Houze (1979) to study convective rainfall rates and the time variation of convective and stratiform rainfall during the 4-5 September 1974 GATE system. Her findings also indicate that nearly 40% of the rainfall was stratiform, with a similar distribution of convective rainfall by echo top height. Area mean rainfall rates computed for all convective echoes revealed an increase in rainfall rate with increasing echo top height. Leary also noted that errors in these results may arise in two ways. First, some subjectivity is involved in defining the boundaries between convective and stratiform precipitation. Second, the rather large spatial (4×4 km) and temporal (1-hour) resolution of the analyzed data will not resolve all of the convective rainfall, which may occur on spatial and temporal scales smaller than those used in this study. Both of these factors may artificially inflate the fraction of rainfall from stratiform cloud.

In one of the first papers to present variations in precipitation vertical structure, Leary and Houze (1979b) calculate melting rates associated with the radar bright bands in five MCSs. Vertical profiles of stratiform radar reflectivity reveal noticeable differences in profile shape from one system to the next. These differences lead to storm-to-storm variations in ice and water mass contents up to a factor of three and four, respectively, while cooling rates associated with melting varied by a factor of nearly 10. Although these variations were not the focus of their paper, such differences may result from variations in 1) water vapor mixing ratio profiles, 2) ice mass above the freezing level, 3) hydrometeor size

distributions, and 4) uncertainties in the reflectivity-water content (Z-M) relationship. Given the influence of decaying convective elements on stratiform cloud, variations in ice mass and size distributions may be closely linked to the vertical structure properties of convective elements.

LeMone and Zipser (1980) and Zipser and LeMone (1980) presented findings on *in situ* measurements of vertical updraft and downdraft cores within GATE MCSs. They reported that core diameters, average and maximum vertical velocities, and mass fluxes were also approximately lognormally distributed. Most interestingly, however, was that only about 10% of updraft cores had mean vertical velocities as great as 5 m s^{-1}, which is less than the median mean updraft velocity of continental thunderstorm updrafts observed during the Thunderstorm Project (Byers and Braham, 1949). Zipser and LeMone attributed this difference to differences in convective available potential energy (CAPE) between the GATE environment (approximately 1500 J kg^{-1}) and the mean Thunderstorm Project environment (about 3000 J kg^{-1}), as well as the narrow diameter of the GATE updrafts, which would decrease their buoyancy by entrainment. Subsequent studies of tropical convective vertical updraft structure from the TAMEX (Jorgensen and LeMone, 1989) and EMEX (Lucas *et al.*, 1994) projects reveal profiles of updraft velocities remarkably similar to those observed in GATE.

One of the most important points discussed in Zipser and LeMone (1980) is the implication of weak updraft structures on microphysical processes and vertical profiles of radar reflectivity. For even the strongest updrafts observed during GATE, the time required for a parcel to travel from cloud base to the freezing level is about one hour. Assuming a maritime droplet spectrum, this is a sufficiently long enough time for rainfall to grow from collision-coalescence processes, acquire fallspeeds greater than the updraft velocity, and fall back to the surface. Similarly, the weak updrafts above the freezing level allow conversion from liquid water to ice particles over a relatively short distance, due to the long time period required for those drops to ascend above the freezing level and the probablistic nature of drop freezing. The authors attributed the large amount of water mass confined below the freezing level, combined with the relative scarcity of supercooled liquid water, to the rapid decrease in radar reflectivity with height above the freezing level.

To further investigate the correlation between convective reflectivity profile and vertical updraft velocities, Szoke *et al.* (1986) compared convective core reflectivity profiles from nearly 300 GATE cells to profiles of convective cores in hurricane rainbands and eyewalls, as well as those in continental storms producing rain, hail, and tornadoes. The GATE profiles exhibit a nearly constant reflectivity value up to the freezing level; above the freezing level, reflectivity drops off sharply. Profiles from hurricanes are similar. In contrast, the more vigorous continental storms exhibit profiles characterized by higher reflectivity values below the freezing level, and a more gradual decrease in reflectivity with height. Tornadic storms often have peak reflectivities well above the freezing level. Examination of a larger number of profiles and environmental soundings also lead to a revised theory concerning what governs updrafts strength and reflectivity profile shape. Szoke *et al.* (1986) argue that differences between tropical and continental updraft strengths are likely due less to the total CAPE than to differences in the distribution of buoyancy with height. For example, the GATE and hurricane soundings are nearly moist adiabatic, so CAPE is distributed over a large depth, whereas continental thunderstorms are often characterized by large CAPE over limited depth.

In a companion paper, Szoke and Zipser (1986) addressed the question of how the mean GATE reflectivity profile relates to the life cycle of individual convective cores. Using a subset of 42 cores from the Szoke *et al.* (1986) paper, they computed time-height cross sections of reflectivity for each cell. Their analysis revealed that all cells, regardless of maximum height, have an initial echo well below the freezing level and an early rainout period likely dominated by warm rain processes. For all but the shortest-lived (and usually isolated cells), cloud top height extended well above the freezing level during the mature and dissipating stages. The mean GATE reflectivity profile is typical of the profiles observed in individual cells during these stages, although the rate of reflectivity decrease above the freezing level varied from day to day, and from one cell to the next.

Further support for the theory relating vertical reflectivity structure to updraft velocities came from lightning observations during DUNDEE (Rutledge *et al.*, 1992). During the 1988-1989 wet season, lightning flash rates were observed to increase during periods of high environmental CAPE when the monsoon trough was north of Darwin, and decrease during the periods where the monsoon trough was

located south of Darwin and CAPE values decreased. Lightning production is thought to be most efficient in a cloud environment between 0°C and -20°C that is characterized by both ice particles and liquid water. Therefore, convective updrafts must be of sufficient strength to loft millimeter-sized water drops above the freezing level (thus producing ice particles via freezing) and allow supercooled cloud water to exist in the presence of ice. The fact that lightning rates increase during periods when CAPE is higher suggests that the higher CAPE regime results in updrafts of sufficient strength to lead to lightning production. The lower CAPE periods apparently do not produce many updrafts of sufficient strength to produce these mixed-phase microphysical conditions. Reflectivity profiles from an MCS occurring in each regime (high and low CAPE) reveal structures that are consistent with the vertical velocity-reflectivity structure arguments presented in Zipser and LeMone (1980). Namely, the MCS occurring in the low CAPE environment had few convective cores with 30 dBZ reflectivities extending above the freezing level, while the high CAPE MCS had 30 dBZ cores extending up to 15 km.

Zipser and Lutz (1994) analyzed the reflectivity "lapse rate" (rate of reflectivity decrease with height) above the freezing level of convective cores from break period and monsoonal convection observed during DUNDEE and compared these lapse rates to those of lightning-producing mid-latitude cores. They found that mid-latitude cores had low reflectivity lapse rates above the freezing level, implying large amounts of supercooled liquid water, graupel, and/or ice above the freezing level, which is consistent with the high lightning flash rates of these storms. Monsoonal cores, on the other hand, had much larger lapse rates. Lapse rates of cores from break period cases were centered between the continental and monsoonal populations, with the extrema of the population spreading into both the continental and monsoonal regimes. The authors, however, point out that many of the break period systems were sampled during their decaying stages, and suggest that a sample of mature cells would have lapse rates resembling those of the continental cells, which would be more consistent with the high flash rates observed in these systems. The results of this paper support the notions of Rutledge *et al.* (1992) that monsoonal systems produce less lightning due to the frequent absence of mixed-phase microphysical conditions above the freezing level.

Using observer reports, Zipser (1994) performed an analysis of rainfall and lightning occurrence in the GATE region and several West African stations. He concluded that periods of onshore flow in the tropics were often associated with high rainfall amounts but little lightning, consistent with the observations of monsoon precipitation near Darwin, Australia (Rutledge *et al.*, 1992; Williams *et al.*, 1992; Zipser and Lutz, 1994). Furthermore, the propensity of lightning flashes to continental regions and island locations combined with the global distribution of rainfall (i.e., large rain amounts occurring over both land and oceanic regions) suggests two rainfall regimes—one of high rainfall and high lightning counts, and one with high rainfall and low lightning counts. Based on the results of the two previously discussed papers, these two regimes would also be characterized by different convective reflectivity profiles.

Petersen *et al.*, (1996) examined the diurnal evolution of CAPE, lightning production, rainfall, and infrared (IR) cloud signatures observed during TOGA COARE. Their results indicate that over the diurnal cycle, cloud-to-ground lightning and convective precipitation maximize near the same time as the CAPE maxima. They note, however, that the IR brightness temperature areas associated with these systems (in a composite diurnal cycle sense) reach their maximum values about 2 hours after peak lightning and rainfall, with the greatest increase in cold cloud area occurring at the time of peak rainfall and lightning. This suggests that diurnal studies that relate cold cloud signatures to intense convection should consider the time rate of change of cold cloud area rather than cold cloud area itself.

Chapter 2

TOGA COARE OVERVIEW AND DATA ANALYSIS METHODS

2.1 Overview of TOGA COARE

2.1.1 Climatological background

The western Pacific warm pool region during the boreal winter is characterized by ocean sea surface temperatures (SSTs) exceeding 28°C. These warm waters provide ample fuel for deep convection, and therefore strong diabatic heating, which feeds the rising branch of the east-west oriented Walker circulation, illustrated in Fig 2.1. Fig. 2.2 shows the average SST, outgoing longwave radiation (OLR), and vertically integrated heating for the month of December through February, 1985-1990 (Vincent and Schrage, 1995). Fig. 2.3 presents the mean and variance of the 850 mb wind field during this same period. Mean winds in the warm pool region are light, often less than 3 m s^{-1}, and usually from the east. However, the wind speed in this region can be quite variable. Most of the prolonged wind events are associated with the 30–60-day intraseasonal oscillation (ISO), which is discussed in the next paragraph.

The tropical intraseasonal oscillation was first described by Madden and Julian (1971; 1972). The ISO is characterized by periodic variations in wind direction and speed, surface pressure, and cloudiness over time scales of 30 to 60 days. Fig. 2.4 is schematic presentation of the ISO which emphasizes the fact that the convective component of this circulation is most clearly defined over the Maritime Continent. Convection associated with the ISO is composed of large eastward-moving super cloud clusters, each of which contain several smaller cloud clusters which propagate towards the west (Nakazawa, 1988). As such, there is a significant interaction between motions on various spatial and temporal scales. Strong low-level westerly winds usually follow passage of the convective component of the ISO, as illustrated in Fig. 2.5, leading to enhanced surface fluxes and often producing wind shear

profiles that are unfavorable for organized convection (Lin and Johnson, 1996a). Origins of the oscillation remain unclear, but it is typically described as a coupled Kelvin-Rossby mode interacting with a variable heat source (see Madden and Julian (1994) for specific references).

In addition to the ISO, westward propagating disturbances with 4–5-day periods are also quite common in the western Pacific. Reed and Recker (1971) studied the composite properties of 18 such disturbances observed in the Intertropical Convergence Zone (ITCZ) region of the western Pacific in 1967. They found negative temperature deviations in the vicinity of the wave trough at low and high levels, but positive deviations at mid-levels. Highest relative humidities, strongest upward motion, and greatest rainfall and cloud amount were also centered on the trough axis. The mid-level heating in the trough vicinity is likely due to diabatic heating associated with rainfall formation, while the upper- and lower-level cooling signatures are associated with radiational cooling and convective and mesoscale downdrafts, respectively. Maximum heating was centered at the 300 mb level. The diabatic heating difference between trough and ridge locations maximized at 400 mb where it reached nearly 10°C day^{-1}.

2.2.2 Description of program goals and observing platforms

A thorough description of the Tropical Ocean-Global Atmosphere (TOGA) Coupled Ocean-Atmosphere Response Experiment (COARE) is provided in Webster and Lukas (1992), and is summarized herein. The TOGA program was a decadal-long program (1985-1995) that sought a description of the tropical oceans and global atmosphere as a time-dependent system, with the ultimate goal being to successfully model the coupled ocean-atmosphere system and predict its variations on time scales of months to years. A major achievement of TOGA has been the improved understanding of the onset of the interannual El Niño-Southern Oscillation (ENSO), which originates in the vicinity of the anomalously warm ocean temperatures of the western Pacific warm pool region. However, questions remain concerning the physical processes that maintain the mean and transient states of the warm pool and how these processes affect ENSO and other large-scale circulations. Specifically, information

concerning the processes that link the ocean to the tropical atmosphere have limited the success of efforts to model phenomena with ties to this region.

COARE was designed as a process study focused on studying couplings between the tropical ocean and atmosphere. Its scientific goals were to describe and understand:

1. the principal processes responsible for the coupling of the ocean and the atmosphere in the western Pacific warm pool system;
2. the principal atmospheric processes that organize convection in the warm pool;
3. the oceanic response to combined buoyancy and wind-stress forcing in the western Pacific warm pool; and
4. the multiple-scale interactions that extend the oceanic and atmospheric influence of the western Pacific warm pool system to other regions and vice versa.

To ensure that these topics were completely addressed, three observational components were developed: an interface component, which focused on interfacial fluxes between ocean and atmosphere; an atmospheric component, which focused on the state of the boundary layer and convective organization; and an oceanic component, which focused on the response of the upper ocean to varying fluxes.

Numerous observing platforms were deployed in order to meet the scientific goals of the project. A complete discussion of the observing platforms can be found in Webster and Lukas (1992) and in those publications specifically mentioned. An enhanced atmospheric sounding network (Fig. 2.6) that was integrated with World Meteorological Organization (WMO) sounding sites (already in place) was developed consisting of Integrated Sounding Systems (ISS; Parsons *et al.*, 1994; Johnson *et al.*, 1996) and rawinsondes which were deployed from both land and ship sites. Soundings were launched at either 12- or 6-hour intervals, depending on their priority. Oceanic monitoring (as well as measurement of some atmospheric quantities) was accomplished through a large-scale array of moorings and drifters (e.g., Hayes *et al.*, 1991; Weller and Anderson, 1995) and survey ships, which also collected data relevant to interfacial fluxes. Point observations of precipitation occurring with the IFA was accomplished through a series of rain gages mounted on buoys, drifters, and ships, while areal precipitation patterns were recorded by two 5-cm Doppler radars mounted aboard two ships stationed within the IFA (Rutledge *et al.*, 1993).

In situ sampling of convective systems was accomplished though the NOAA P-3, NCAR Electra, and NASA DC-8 aircraft. The P-3s and the Electra were each equipped with radar systems to monitor the structure and evolution of precipitation. Satellite observations over the TOGA COARE region from the Geostationary Meteorological Satellite (GMS) and Special Sensor Microwave/Imager (SSM/I) aboard the Defense Meteorological Satellite Program (DMSP) were also collected.

2.1.3 Synoptic overview of Intensive Observing Period

Using infrared (IR) brightness temperatures from the GMS satellite, Chen *et al.* (1995) analyzed the variability of convection during COARE over a range of time scales. They found that most of the variability in cold cloudiness was explained by the intraseasonal oscillation. Within this envelope of convection associated with the ISO were westward-propagating 2-day disturbances, which Chen *et al.* argue are associated with westward-propagating inertio-gravity waves (Matsuno, 1966; Gill, 1982). In a separate analysis of IR data from the COARE region, Indian Ocean, and Indonesia, Velden and Young (1994) also found evidence for oscillations on the 4–5-day time scale. Oscillations on this time scale have also been observed by Nakazawa (1986), Hendon and Liebman (1991), Sui and Lau (1992) and Numaguti *et al.* (1995) and are likely associated with mixed Rossby-gravity waves, as described by Takayabu and Nitta (1993).

Lin and Johnson (1996) have reviewed the kinematic and thermodynamic properties of the flow over the warm pool during COARE, and the following discussion is based on the analysis presented in their paper. Mean IR brightness temperatures over the COARE large-scale domain (10°S to 10°N, 140°E to 180°W) during the IOP reveal that the maximum area of cold cloud (and most frequent deep convection) was situated to the east of the Intensive Flux Array (IFA) by approximately 15 degrees longitude, while a secondary maximum was present to the south and west of the IFA (Fig. 2.7). However, within the four month IOP there were several instances of deep convection situated over the IFA, with considerable cold cloud amounts being situated over the IFA during the month of December.

Three phases of the ISO were observed during the IOP. A Hovmöller-type diagram of percent high cloudiness tracks the passage of the convective portion of the ISO over the IFA (Fig. 2.8). These passages occurred in early November, late December, and late January (although the convective portion of this last ISO seemed to "skip" over the IFA). Each convective maxima of the ISO was followed by a "westerly wind burst" at low levels and the presence of deep zonal shear (Fig. 2.9). Time series of surface wind speed (which is well-correlated with the surface latent heat flux and anti-correlated to surface sensible heat flux), rainfall and mean tropospheric vertical motion (Fig 2.10) illustrate the behavior of these variables during COARE. In general, surface wind speed, upward vertical motion, and precipitation increase as the convective portion of the ISO approaches from the west. Upon its passage, wind speed increases noticeably, rainfall decreases, and mean vertical motion reverses its direction (from upward to downward). These westerly wind burst periods are also characterized by a rapid decrease in SST.

Evidence of higher frequency variability was also observed during COARE. Numaguti *et al.* (1995) present evidence of 4–5-day easterly waves, which they describe as westward-moving mixed Rossby-gravity waves, possibly transitioning to tropical depression-type disturbances, as described in Takayabu and Nitta (1993). Occasionally these disturbances would advect dry air of subtropical origins into the COARE region (see discussion of Mapes and Zuidema, 1996, below). Characteristics of 2-day disturbances are summarized by Takayabu *et al.* (1996) and Haertel and Johnson (1996). Convection associated with these disturbances cycles through shallow, deep, and stratiform stages. The 2-day cycle is believed to be linked to the time required by the lower tropospheric moisture field to recover from the drying caused by deep convection.

Finally, Mapes and Zuidema (1996) studied variations in the profile of water vapor in the COARE region and found that dry layers were often present during the IOP, with frequency peaks near 550 mb (the 0°C level), 800 mb, and 950 mb. They conclude that nearly all of the dry "tongues" consist of filaments of low moist static energy air advected into the column, often from the subtropics. The low-level dry tongues can prevent deep convection and/or cause convection to detrain mass in preferred layers.

2.2 Data and Analysis Methods

2.2.1 MIT 5-cm radar data

The MIT 5-cm Doppler radar was mounted aboard the NOAA Research Vessel John V. Vickers during COARE. Configuration and deployment of the MIT radar are described in Rutledge *et al.* (1993). Table 2.1 summarizes the characteristics of the radar. Since ship motion (roll, pitch, and yaw) is not negligible even in very calm seas, it was necessary to insulate the radar platform from ship motions. Stabilization was accomplished through an Inertial Navigation Unit (INU) mounted directly underneath the radar antenna. Latitude, longitude, and time information were provided by a Global Positioning System (GPS). Roll, pitch, and yaw information from the INU were fed to the antenna controller at high frequency (200 Hz) to provide rapid updates of the antenna position in order to maintain the desired azimuth and elevation angles. This design was able to maintain the prescribed angles to within approximately 0.1° for a large range of sea states.

The R/V Vickers was deployed to the IFA for three approximately 30-day cruises during COARE. The dates of each cruise are shown in Table 2.2. The Vickers was assigned to a point near the center of the IFA (2.08°S, 156.25°E) and was allowed to drift no more than 15 km from this point. When the ship drifted beyond this radius, it was repositioned. Repositioning typically occurred about twice per day, depending on surface wind and ocean current speeds. The similarly equipped and installed 5-cm TOGA radar was also deployed for three cruises during COARE aboard the Peoples Republic of China #5 vessel (PRC5). The PRC5's deployment schedule was such that both ships would be on station for approximately 20-day overlapping periods, with one ship on station for intervening 10-day periods. Except for a brief period in early December, this scedule was well-maintained.

The MIT radar was operated continuously during COARE in both surveillance and full-volume scanning modes. The scanning strategy of the radar was such that a surveillance scan and a full volume scan were collected every 10 minutes. These two scans completed in approximately 8.5 minutes, leaving about 90 seconds for optional RHI scans to be made. Nearly 13,000 full-volume scans were collected during the three cruises. For the purposes of expediency and data storage concerns, this study utilizes every other full-volume scan (20-minute resolution). Raw data were stored in the IRIS data format

(developed by SIGMET, Inc.) and converted to Universal Format using software developed in house. Data were interpolated to a 240×240 km Cartesian grid with 2×2×0.5 km resolution using the Reorder package developed by the Research Data Program of NCAR's Atmospheric Technology Division. Because only every other beam of data was stored in the IRIS format (a fact not discovered until the project was nearly completed), azimuthal resolution of the raw data set is 2°, rather than the intended 1°. Therefore, the Cressman interpolation used in the Reorder step required radii of influence of 2 km in the horizontal and 1 km in the vertical. These relatively large radii of influence may have the result of decreasing the magnitude of local reflectivity maxima beyond what might have been obtained with 1° azimuthal resolution. However, during the one instance when both the Vickers and the PRC5 ships were in Honiara data were collected and distributions of data collected by the MIT radar were compared to those of the TOGA radar with every other beam eliminated from the TOGA sample. The two distributions were quite similar, suggesting that the MIT dataset was not seriously compromised by dropping every other beam.

Table 2.1 Characteristics of the MIT C-Band radar

Operating frequency	5590 MHz
Minimum Detectable Signal	-115 dbm
Peak Power	155 kW
Pulse Width	1.0 microsecond
Antenna Gain	40.5 dB
Beamwidth	1.6 degrees (3 dB)
Antenna scan rates	$30°\cdot s^{-1}$ (Azimuth and Elevation)
Antenna Accelerations	$>40°\cdot s^{-1}$
Elevation Upper Limit	50°
Elevation Lower Limit	-18°
Pulse Repetition Frequency	250-1500 Hz

Table 2.2 Dates of the three cruises of the R/V Vickers during TOGA COARE.

Cruise	Dates	Julian Days*
1	10 Nov 92 - 10 Dec 92	315 - 345
2	21 Dec 92 - 19 Jan 93	356 - 385
3	29 Jan 93 - 25 Feb 93	395 - 412

* for 1993 dates, 366 has been added to the Julian day.

Once the data were interpolated to a Cartesian grid, they were partitioned into convective and stratiform components using an adaptation of the technique presented in Steiner and Houze (1993) and Steiner *et al.* (1995). An explanation of the partitioning processes explored in this study is presented in Appendix A. It should be clearly emphasized that partitioning radar reflectivity data into convective and stratiform components without the aid of vertical velocity information entails subjective judgments concerning the nature of the two precipitation types. The basic definition of stratiform rainfall relates precipitation particle fallspeeds to the magnitude of the vertical velocity as follows:

$$v_t \gg |w| \tag{2.1}$$

where v_t is hydrometeor terminal fallspeed and w is vertical air motion. In these conditions, ice particles detrained from the tops of convective towers and falling through stratiform cloud therefore have ample time to grow by depositional and aggregational processes. As the ice particles fall through the freezing level, they acquire a coating of liquid water, which results in an increase in reflectivity due the higher refractive index of water compared to ice. Complete melting results in a reduction of reflectivity since the hydrometeor is composed completely of water and "collapses" into a spheroidal or oblate spheroidal shape (thereby reducing its geometric cross section). The result of many precipitation particles undergoing this ice-to-water conversion process results in a shallow layer of enhanced reflectivity just below the freezing level, known as the radar bright band.

The presence of a reflectivity bright band structure just below the freezing level is a strong indication of stratiform precipitation, but this feature cannot be resolved farther than about 100 km from the radar for a 1° beamwidth (Steiner *et al.*, 1995). Therefore, the presence of a bright band can only be used to "tune" an algorithm that partitions echo into convective and stratiform components. Partitioning is therefore based on the horizontal variability of radar echo, which is where the subjective assessments are introduced. In almost any given radar volume, an observer familiar with precipitating systems can identify regions of convective and stratiform echo. The area of greatest subjective impression arises in trying to determine how much echo beyond an easily-identifiable convective core should be classified as convection. When available, vertical velocity information has been used to improve reflectivity-only

partitioning algorithms (DeMott *et al.*, 1995) and can also be used to explore the question of how to classify echo at the "edges" of convective clouds based on the variability of the vertical velocity in these regions (Willis *et al.*, 1995). It is important to note that the assumptions one makes concerning the nature of convection in these "gray" areas may result in differences on the order of 10–15% in convective-stratiform rainfall totals (Cheng and Houze, 1979; Rickenbach, 1996, personal communication). Furthermore, because different sets of assumptions may lead to more or less "joining" of convective cells into a single convective feature, the assumptions made will also influence statistics on the number of convective features identified, the size of the features, their shape and orientation.

Optimum assumptions for partitioning the MIT radar data set were based on close inspection of contoured frequency by altitude diagrams (CFADs; Yuter and Houze, 1995) of stratiform vertical velocity for a few cases where simultaneous reflectivity and vertical velocity information were available. In this technique, the method that produced the narrowest distribution of stratiform velocities was deemed the best, based on the conditions described in Eq. 2.1. An example of a constant altitude plan position indicator (CAPPI) at 2 km of a volume before and after partitioning is shown in Fig. 2.11. Note that several individual convective cores merge together to form a few large convective features. In all subsequent discussions, *a convective feature is defined as a cluster of convective echo that may be composed of one or more convective cores.* The issues concerning this clustering of cores into one feature is discussed in the next chapter.

Once a volume was partitioned into convective and stratiform components, a database of all identified convective features was compiled. For each identified feature, the feature area, height, mean rainfall rate[1], and 30 dBZ contour height were recorded. Feature heights and 30 dBZ contour heights were defined as the highest occurrence of these values. Mean heights and the variability of these heights within a given feature are discussed in the next chapter. For the three cruises of the R/V Vickers, approximately 200,000 individual convective features were identified. It should be noted that features

[1] Rainfall rate-reflectivity equations used in this study are based on the work of Thiele *et al.* (1994) who derived separate rainfall rates for convective and stratiform rainfall observed with a disdrometer on Kapinga. The rainfall rates are $Z = 139R^{1.43}$ for convective rain and $Z = 374R^{1.43}$ for stratiform rain.

were not tracked in time, so a feature with a lifetime of 3 hours would be surveyed and recorded a maximum of nine times (at 20-minute resolution), providing it did not advect out of the radar volume during that period. Since this study focuses on the evolution of the *distribution* of features, rather the life cycle of individual features, multiple samplings of features does not bias the results.

2.2.2 Sounding network

The Large Scale Array (LSA; Fig. 2.6) of atmospheric sounding stations observed the atmospheric structure on the synoptic scale, while the Outer Sounding Array (OSA) and Intensive Flux Array (IFA) monitored conditions on the mesoscale. Stations composing the OSA and LSA launched soundings four times per day, while the remaining stations launched them twice per day.

This study uses results of the objective analysis of COARE sounding data described in Lin and Johnson (1996). In their paper, the authors describe the steps taken to interpolate the individual soundings to a Cartesian grid (spanning 130°E to 170°W, and 20°S to 20°N). Rawinsonde data (temperature, specific humidity, zonal and meridional wind components, and height) were interpolated to a common vertical resolution of 25 mb (from 1000 mb to 25 mb) and then smoothed with a 1-2-1 filter. To obtain data at 6-hour resolution, soundings at those stations that launched balloons only every 12 hours were interpolated to 6-hour resolution. Interpolation onto the 1°×1° Cartesian grid was accomplished via a Barnes analysis scheme (Barnes 1964, 1973) using interpolation from the six stations closest to the gridpoint of interest. Therefore, the variable spacing of soundings in the analysis area implies a varying radius of influence in different areas of the grid. Divergence profiles were calculated using a finite centered-difference method. The mass continuity equation in p-coordinates was integrated from the surface to the tropopause to obtain vertical velocity estimates. A constant correction was applied to the divergence at all levels to satisfy mass continuity (O'Brien, 1970).

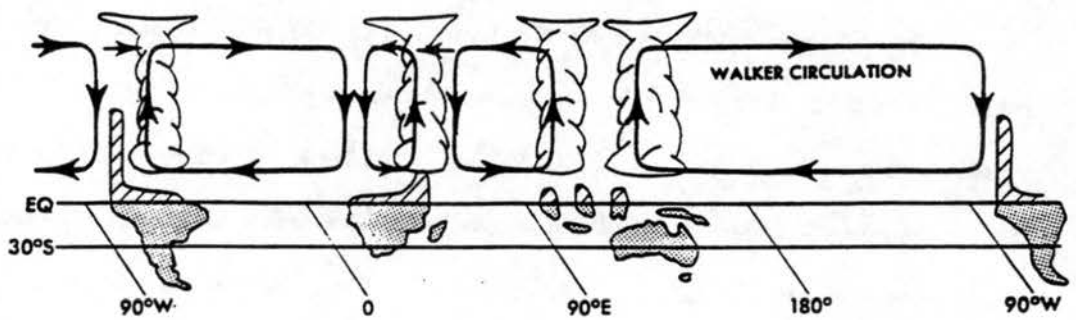

Fig. 2.1. Schematic illustration of the Walker circulation during non-ENSO conditions. Rising air and heavy rains tend to occur over Indonesia and the western Pacific, southeast Africa, and the Amazon basin. Sinking air and desert conditions are found over the eastern equatorial Pacific and southwest Africa. The strongest branch of the Walker circulation over the Pacific is related to the warm SSTs in that area (from Peixoto and Oort, 1992).

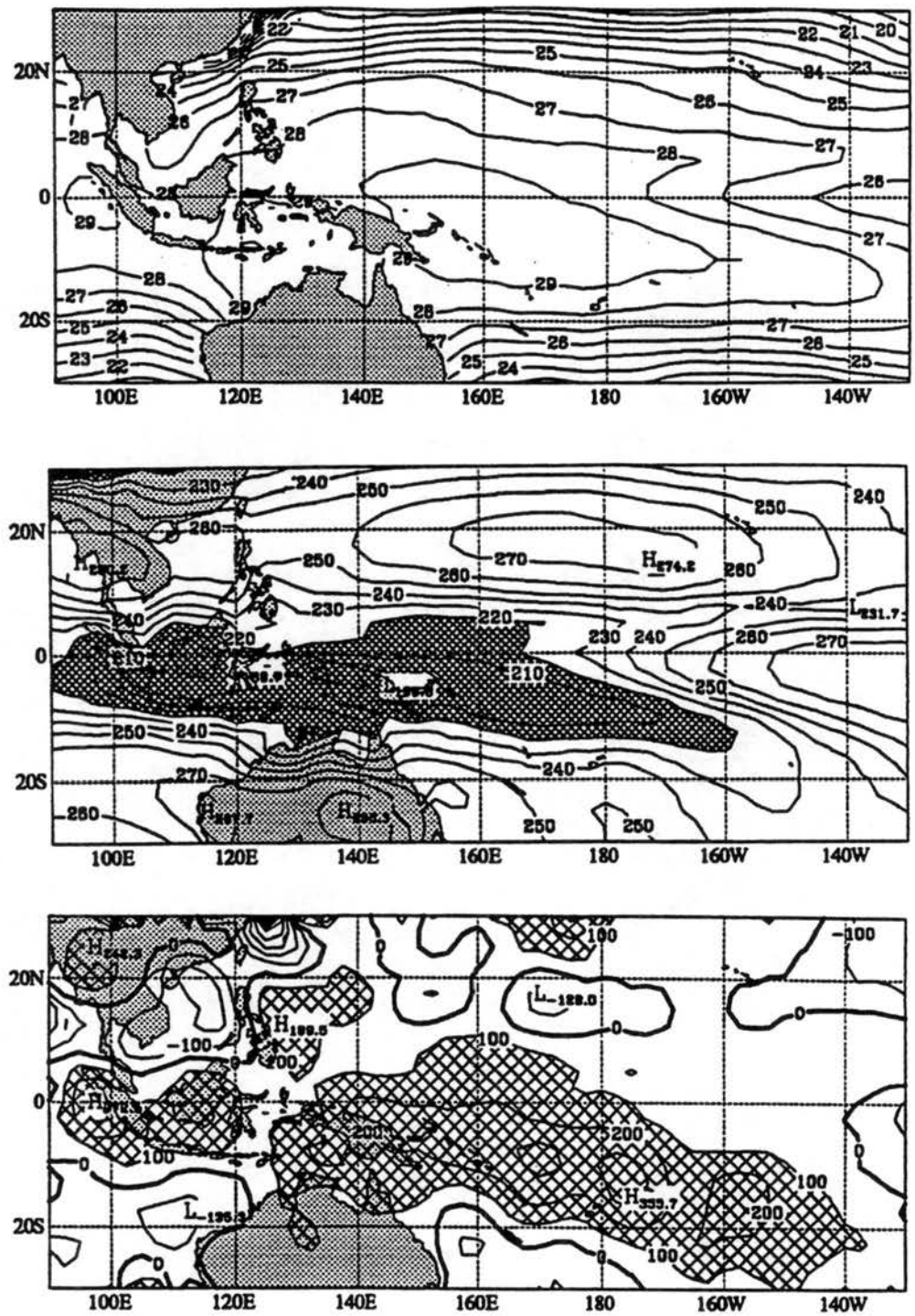

Fig. 2.2. Distribution of mean a) sea surface temperature, b) outgoing longwave radiation, and c) column-integrated diabatic heating in the western Pacific for December through February, 1985–1990 (from Vincent and Schrage, 1995).

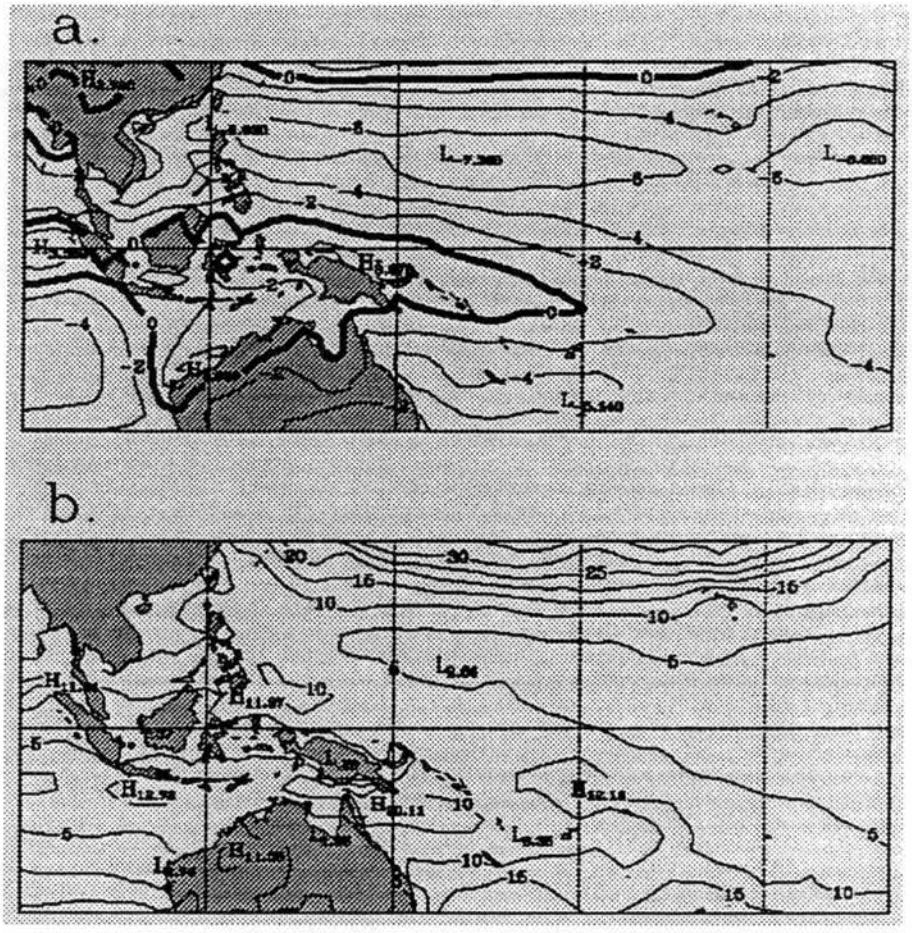

Fig. 2.3. Distribution of a) mean and b) variance of the western Pacific 850-mb zonal wind for the December through February season, 1985–1990 (from Vincent and Schrage, 1994).

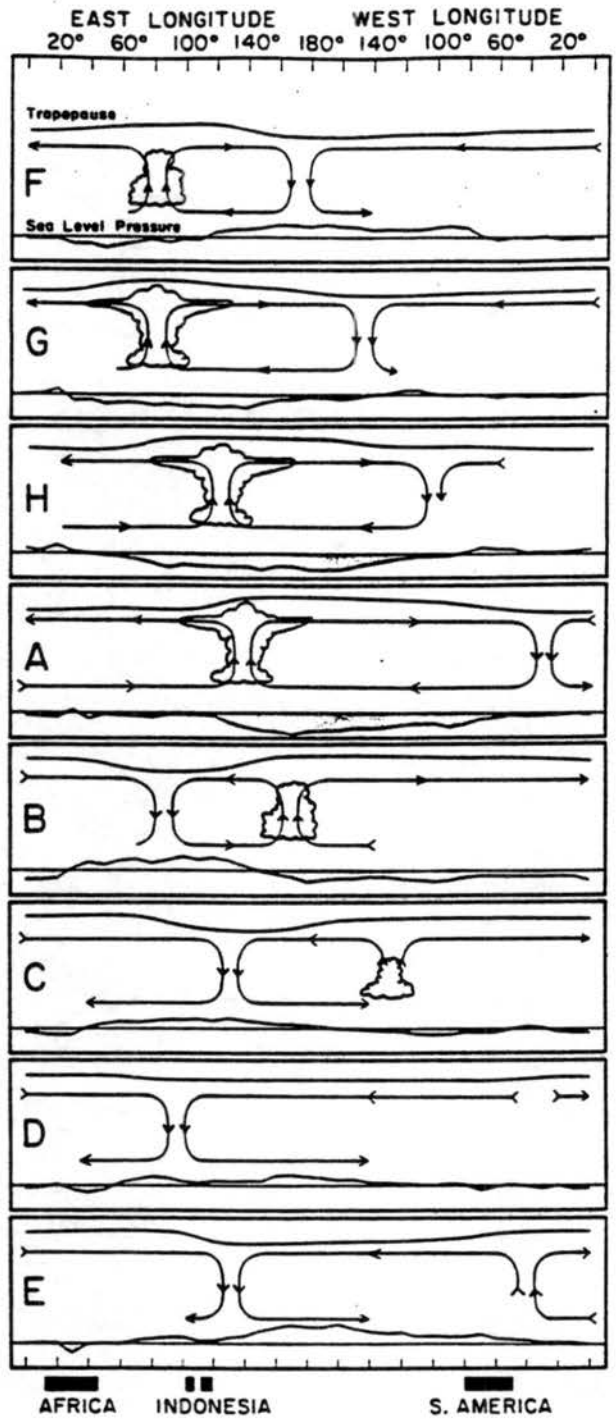

Fig. 2.4. Schematic illustration of the variations of zonal winds and convective activity associated with the intraseasonal oscillation. Letters in the left-hand portion of each pane correspond to surface pressure measured at Canton island (A corresponds to minimum pressure, E corresponds to maximum pressure). (From Madden and Julian, 1972).

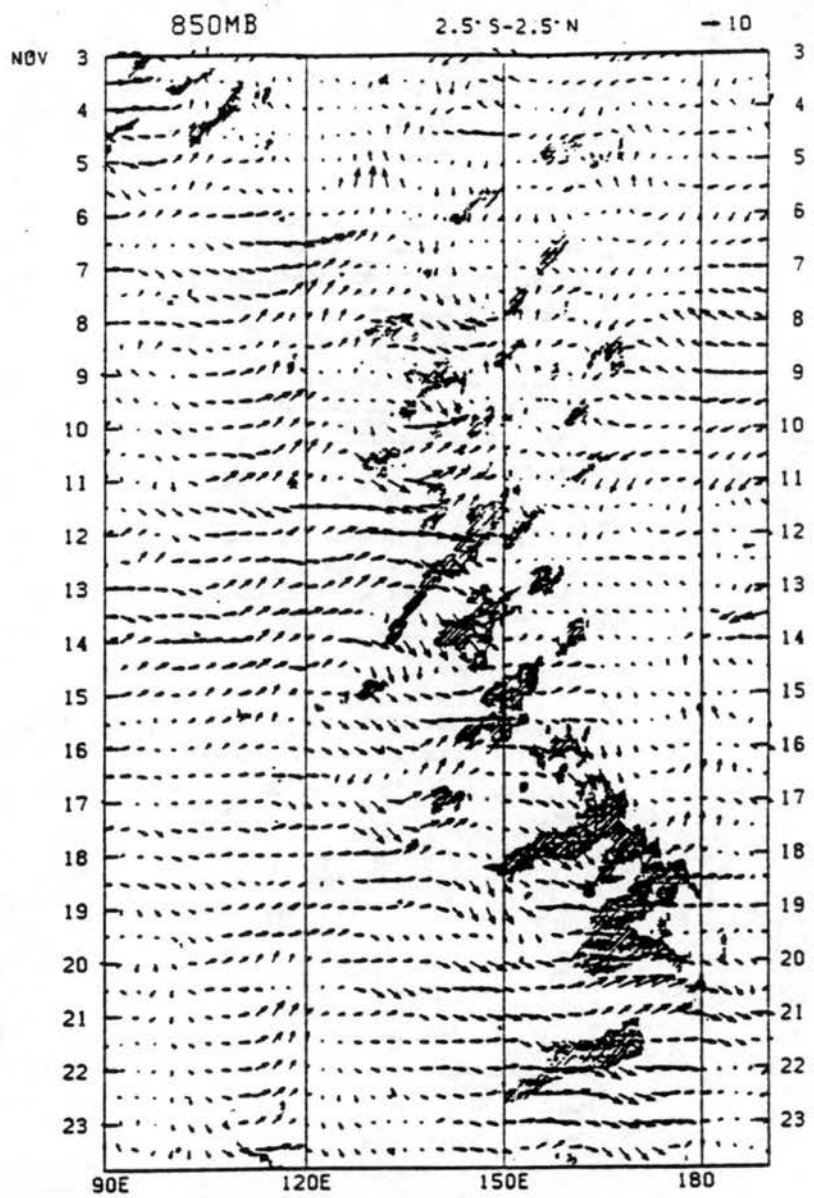

Fig. 2.5. Time-longitude diagram of the variation of a cold IR brightness temperature index (shaded region) and 850-mb winds derived from the European Centre for Medium Range Weather Forecast objective analysis for the latitude strip 2.5°s to 2.5°N (from Lau *et al.*, 1989).

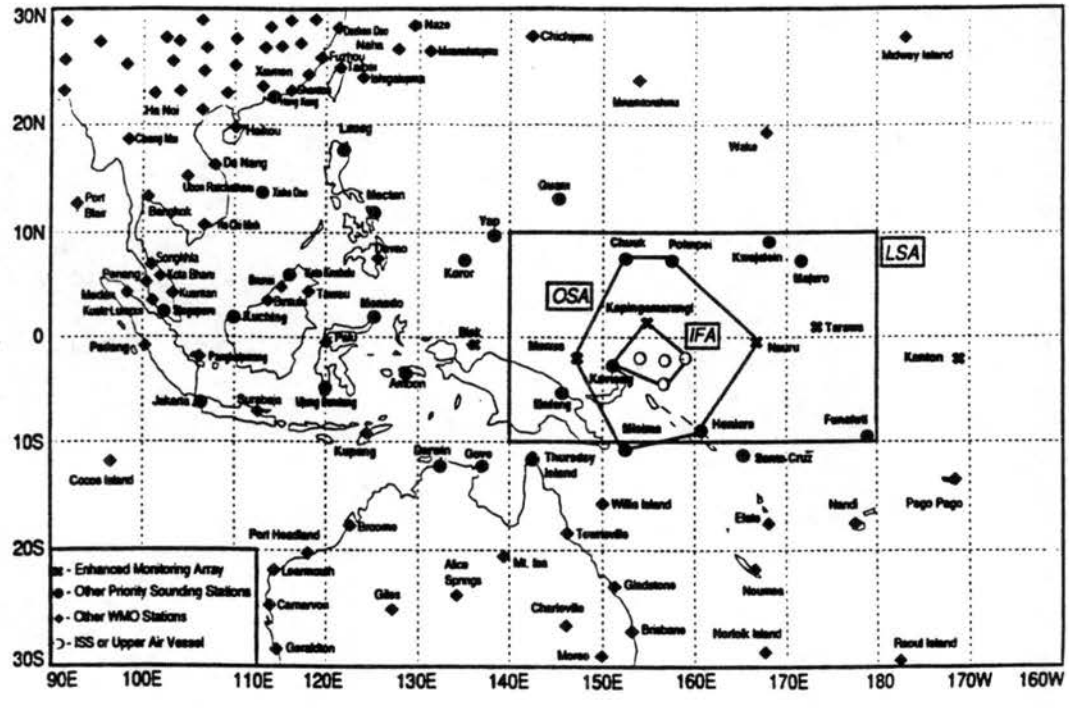

Fig. 2.6. The TOGA COARE sounding network. Locations of the Large Scale Array (LSA), Outer Sounding Array (OSA), and Intensive Flux Array (IFA) are also shown.

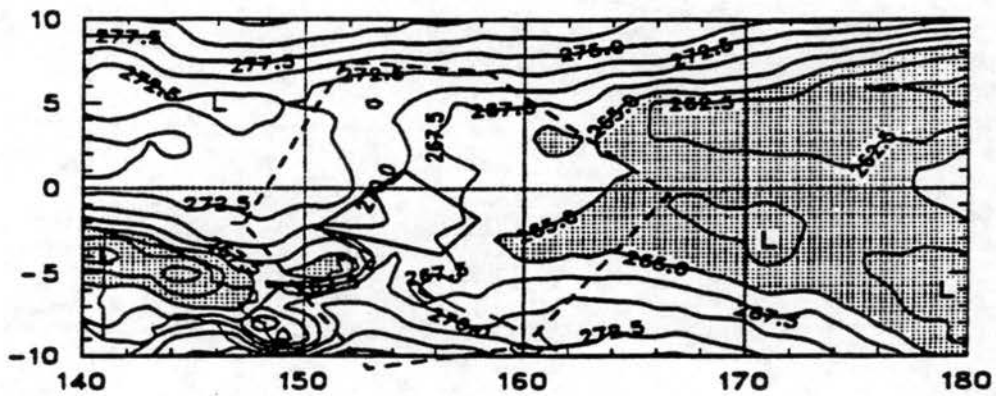

Fig. 2.7. IOP-mean mean brightness temperatures over the Large Scale Array. Areas with temperatures less than 265 K are shaded (from Lin and Johnson, 1996).

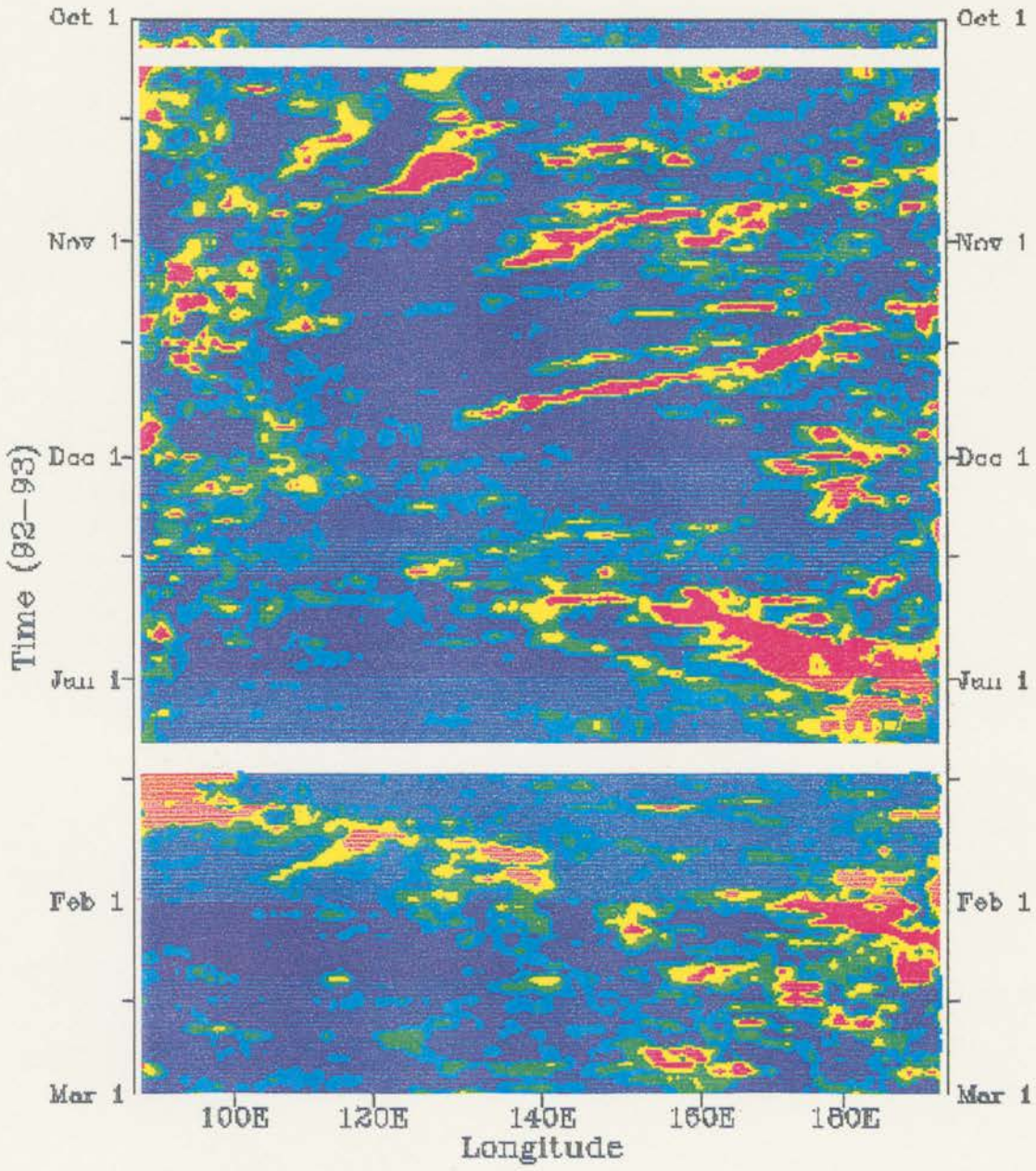

Fig. 2.8. Time-longitude diagram of percent high cloudiness (PHC, the fractional time coverage of cloud with infrared temperature less than a given threshold) index for the 20°S to 20°N latitude strip during TOGA COARE. The PHC index is the meridional summation of one-day×0.5° grid points with daily PHC values > 25% (from Chen *et al.*, 1995).

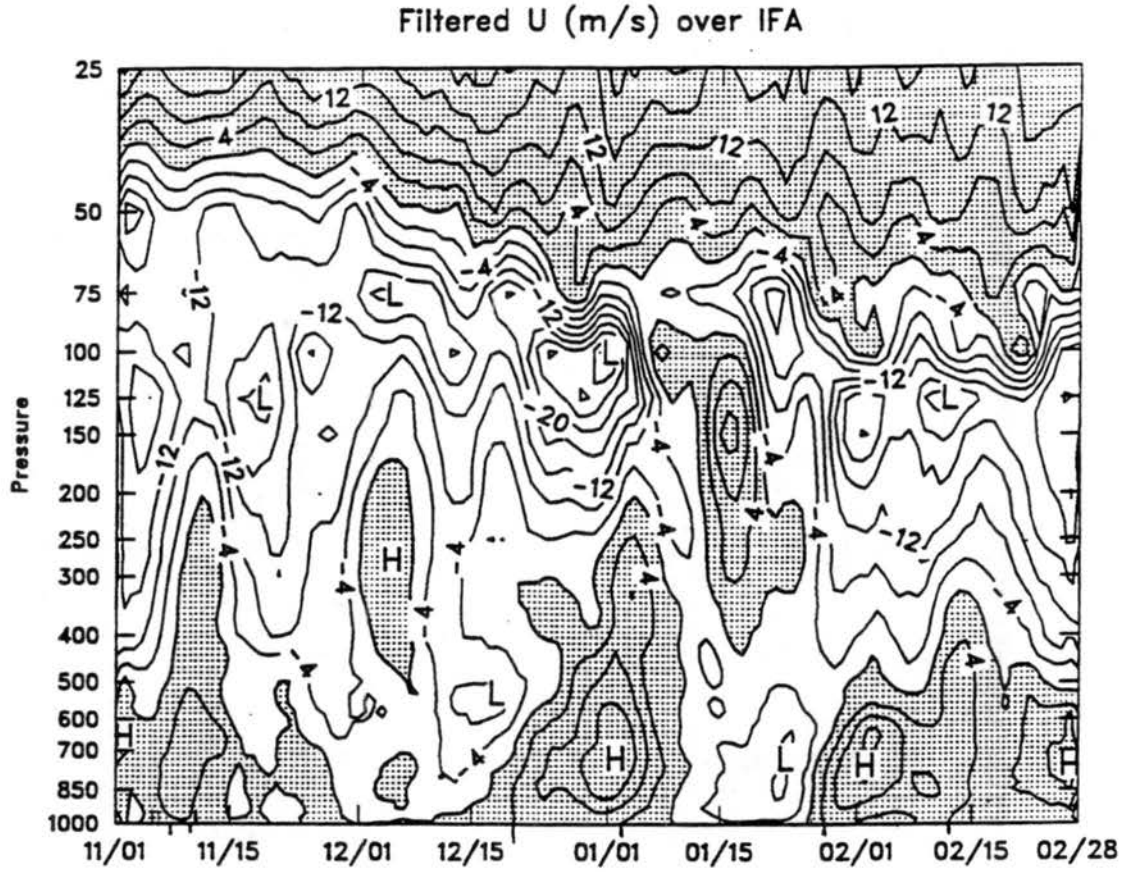

Fig. 2.9. Time-height cross section of IFA-mean zonal wind during COARE (5-day running mean applied). Contour interval is 4 m s^{-1}, with westerly winds shaded (from Lin and Johnson, 1996a).

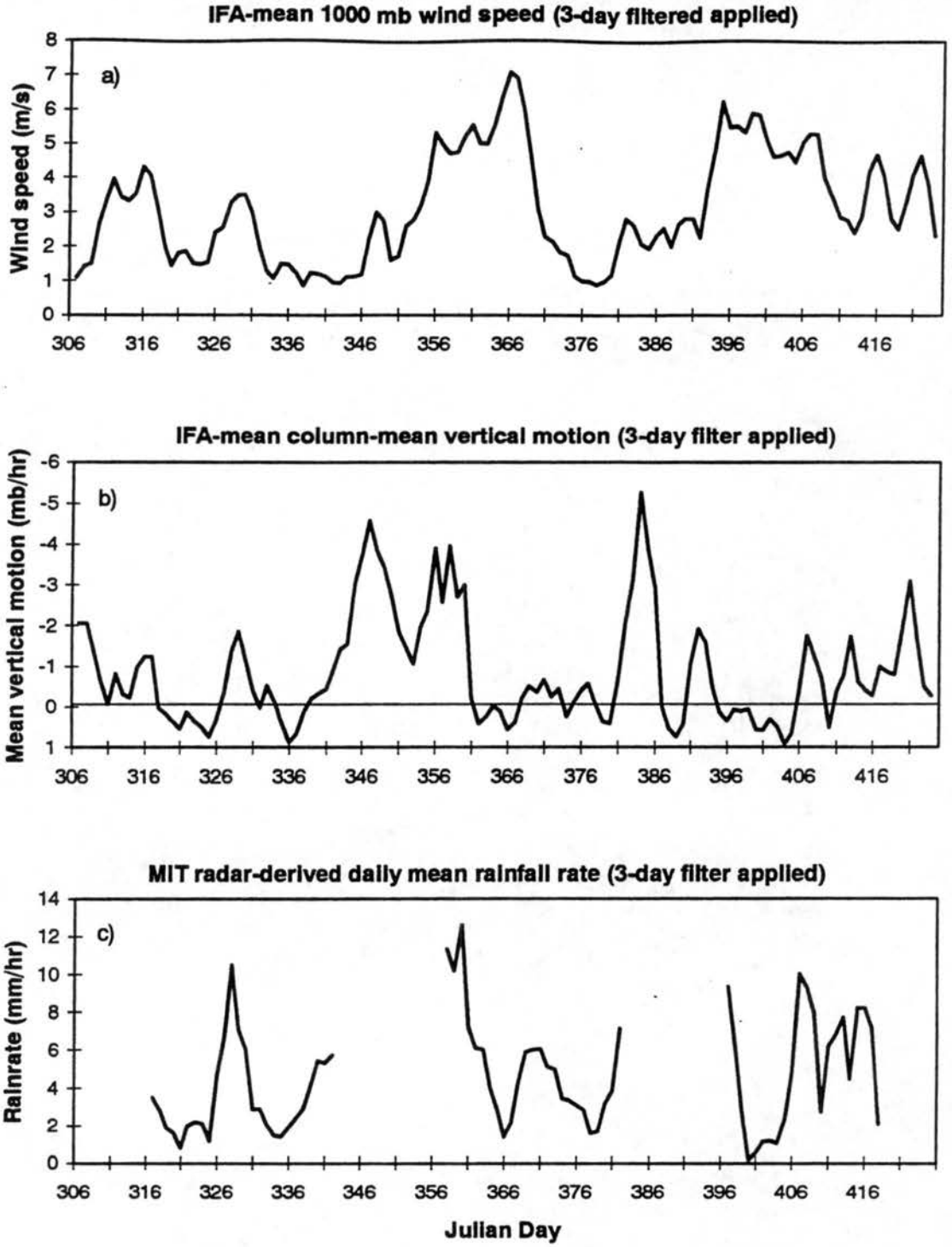

Fig. 2.10. Time series of a) daily mean surface wind speed, b) column-mean vertical motion, and c) MIT radar-derived rainfall. Surface wind speed and vertical motion curves are based on the objective sounding analysis provided by Lin and Johnson. Daily mean rainfall estimates were provided by T. Rickenbach.

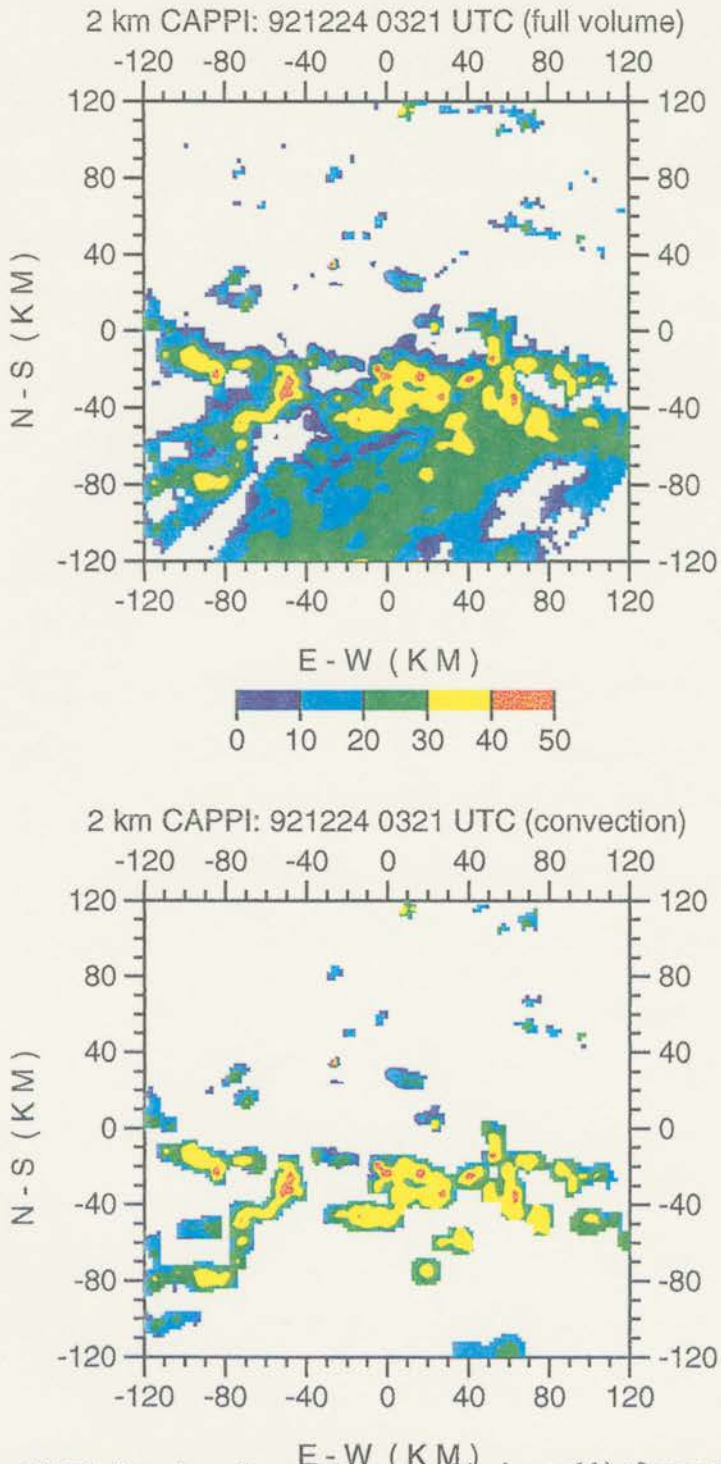

Fig. 2.11. 2-km CAPPI of a radar volume a) before partitioning and b) after partitioning into convective and stratiform components. Only the convective portion of the reflectivity field is shown b). Contour intervals are 10 dBZ.

Chapter 3

MEAN CHARACTERISTICS OF CONVECTIVE ECHO DURING COARE

There is no simple way to describe a population of convective clouds. Each cell has a height, an "internal" vertical structure, an area, and an associated rainfall rate. How convective features are distributed according to these variables influences the distribution of total convective area and rainfall production as classified by these variables. This chapter seeks answers to the following questions:

1. What are the distributions of convective echo during COARE as described by echo height, 30 dBZ contour height, area, and rainfall rate? How do these distributions compare to observations from other parts of the world?
2. How do variables such as echo top height, 30 dBZ contour height, and rainfall rate vary within individual convective features?
3. Which convective elements are the most important in terms of convective rainfall production?
4. Which convective elements produce the most intense rainfall rates?
5. Which convective elements have the most vertically intense internal structures?

These questions are addressed by constructing various distributions of the convective features identified by the partitioning process described in Chapter 2. Each section of this chapter addresses one of the questions posed above.

3.1 Characteristics and distributions of convective echo

3.1.1 Mean reflectivity profiles

Mean reflectivity profiles for each of the three Vickers's cruises are presented in Fig. 3.1a. The profiles were computed by summing the linear reflectivity values at each Cartesian grid level in each volume analyzed during each cruise. These sums were then divided by the corresponding total number of grid points with echo at each level, and then converted to dBZ. Following the discussion of reflectivity profile shape in Chapter 1, the magnitudes of the profiles will be compared both below the freezing level (approximately 5 km) and above. Below the freezing level, the profiles from Cruises 1 and 3 are the most intense, with a mean value of about 26 dBZ. The low-level profile during Cruise 2 was only about 24 dBZ. Above the freezing level, the reflectivity profile of Cruise 1 is most intense—about 1 dB greater than the profiles of Cruises 2 and 3. Note that during Cruise 3, the mean reflectivity decreases rapidly above the freezing level. Although the mean reflectivity profiles differ by no more than 1-2 dBZ at any given level, these differences are significant at the 95% confidence interval. In other words, there is only a 5% chance that the differences arise by chance.

Fig. 3.1b presents mean reflectivity profiles of the partitioned fields. The stratiform partition from all three cruises exhibit distinct bright band structures, demonstrating the general effectiveness of the partitioning algorithm. The convective profiles are very similar to the volume-mean profiles—which is expected since the volume-mean profiles are biased towards the higher reflectivities—but with slightly higher magnitudes. Again, the low-level convective profiles from Cruises 1 and 3 are about 2 dB greater than that of Cruise 2. Above the freezing level, the Cruise 1 profile is about 1-1.5 dB greater than the Cruise 2 and Cruise 3 profiles. The shapes of the convective profiles suggest that the convection during Cruise 2 was the least intense in terms of vertical air motions and water mass above the freezing level. In contrast, the convective profile shape from Cruise 1 suggests that convection during this period was more vigorous and characterized by greater water content above the freezing level than the other two cruises. Finally, convection during Cruise 3 was characterized by large reflectivities below the freezing level, but the rapid decrease in reflectivity with height indicates that there was less water mass above the freezing level than in Cruise 1, suggesting less vigorous updrafts during this period.

What are the causes for differences in convective reflectivity profile shapes from one cruise to the next? Considering the relatively quiescent conditions that were prevalent during Cruise 1, the vertically

intense reflectivity profile (i.e., comparatively higher reflectivity values above the freezing level compared to Cruises 2 and 3) is somewhat surprising. However, it should be kept in mind that the reflectivity profiles observed during COARE are not equally weighted in computing the mean for any given cruise. Rather, those periods that were characterized by widespread convection are more heavily weighted, simply because they contain more convective data points than inactive days. Therefore, even though extensive periods of Cruise 1 were characterized by nearly suppressed conditions, the few days that had active and widespread convection will have a disproportionate influence on the mean reflectivity profile.

Several previous studies (Jorgensen and LeMone, 1989; Zipser and LeMone, 1980; Zipser and Lutz, 1994; Lucas et al, 1994) have argued that reflectivity profile shape is in part tied to the vertical distribution of thermal buoyancy (see discussion in Chapter 1). The increased vertical updrafts that are possible in a more convectively unstable or higher CAPE environment should result in the lofting of larger quantities of water mass to greater heights, resulting in greater reflectivities aloft. To determine if this theory is consistent in a mean sense with the reflectivity profiles observed during COARE, mean thermal buoyancy profiles were computed for each cruise from the interpolated sounding data. For each 6–hourly interpolated sounding at 2°S, 156°E, the thermal buoyancy distribution was computed as follows: a parcel with temperature and moisture properties determined by averaging virtual temperature and specific humidity from 1000 mb to 960 mb was lifted dry-adiabatically to the lifted condensation level (LCL), at which point it was lifted moist-adiabatically until it reached its level of neutral buoyancy (LNB). The irreversible assumption (all condensate falls out as precipitation) was used. The difference between the temperature of the parcel and the environment at a given level is the thermal buoyancy available at that level. Buoyancy profiles were averaged over time to compute the mean profile for each cruise, shown in Fig. 3.2a. A second set of profiles was also computed using only those days where the daily rainfall rate exceeded 5 mm day^{-1}, as determined by the radar-derived rainfall time series (Fig. 3.2b). This set of profiles is, like the reflectivity profiles, also biased to the days that experienced greater rainfall. By averaging buoyancy from the heaviest raining days, the buoyancy in the 750 mb to 550 mb layer is increased by about 0.5°C, while the rest of the profile is nearly unchanged.

The resulting buoyancy profiles are generally consistent with the reflectivity profile shapes. Most noticeably, thermal buoyancy during Cruise 2 is approximately 0.5°C less at all altitudes than in Cruises 1 or 3, which is consistent with its less intense reflectivity profile of Cruise 2 and the more intense profiles of Cruise 1 and Cruise 3. The more subtle variations in profile shape between Cruise 1 and Cruise 3 are not so well explained by the buoyancy profiles, however. Although Cruise 1 has about 0.25°C more buoyancy above the freezing level than Cruise 3, it is the buoyancy profile just beneath the freezing level that is important for generating updrafts of sufficient strength to carry millimeter-sized drops above the freezing level, thereby increasing the reflectivity in this region. In this layer beneath the freezing level (800-600 mb), Cruise 3 has approximately 0.5°C more buoyancy than Cruise 1, yet the Cruise 1 reflectivity profile is more intense than that of Cruise 3 above the freezing level. Reasons for this apparent paradox are not clear. It is possible that local forcing (i.e., interactions between adjacent convective downdrafts) played a more important role in determining convective reflectivity structures in Cruise 1 than in Cruise 3, but this cannot be addressed with cruise-mean profiles. Another potential explanation for this discrepancy may lie with the fact that towards the end of Cruise 3, the ships that served as the eastern and southern corners of the IFA were off station, so soundings taken much farther east of the IFA impacted the resulting temperature and moisture profiles of the interpolated sounding dataset during these periods.

Large-scale vertical motion may also play a role in determining the shapes of the convective reflectivity profiles. The time series of column-mean vertical motion as determined by the interpolated sounding network were presented in Fig. 2.10. The average column-mean vertical motion for all days with rainfall rates exceeding 5 mm day^{-1} are presented in Table 3.1. The vertical motion values, which are derived from the interpolated wind fields, are consistent with the buoyancy profiles, which are derived from the interpolated thermodynamic quantities. Apparently, on the days that experienced moderate to heavy rainfall (greater than 5 mm hr^{-1}) during COARE, the distribution of thermal buoyancy resulted in the strongest vertical motions during Cruise 1 and the weakest vertical motions during Cruise 2. The enhanced vertical motions during these raining days of Cruise 1 are reflected in the more vertically intense profile of radar reflectivity for this cruise as compared to Cruises 2 and 3.

Table 3.1 Mean vertical motion by cruise.

Cruise	Column-mean vertical motion (mb hr^{-1}) for days with rainfall rate $\geq$ 5 mm day^{-1}.	Number of days
1	-1.497	7
2	-0.558	12
3	-0.901	9

3.1.2 Classification of convective echo

Although much can be inferred from the mean convective reflectivity profile, this approach masks all of the variability present within convection. Describing the variability of convection is important for the development of cumulus parameterization schemes, testing cumulus ensemble model output, and designing precipitation retrieval algorithms based on remotely sensed radiative properties of clouds.

Several previous studies of radar echo distributions have been reported by López (1977), hereafter L77), while Houze and Cheng (1977, hereafter HC) have presented similar results for GATE convection. The echo classification methods of these two studies differs from the method used herein in two important ways. First, the L77 and HC papers did not partition the radar echo into convective and stratiform components, so both precipitation types are present in their distributions. Second, echo height and area are defined as the maximum values obtained by these variables during the echo lifetime. In other words, echoes are tracked through time in the L77 and HC studies and classified by the maximum observed height and area, whereas the COARE convective feature database is composed of "snapshots" of convective distributions at 20-minute intervals. Furthermore, HC only examined a subset of GATE echoes. Their sample consisted of all echoes that were present at 12Z; the echoes were tracked forwards and backwards in time to determine their maximum height, area, and duration. One of the first questions to be answered, then, is what effect does partitioning the echo and the "snapshot" approach have on the resulting distributions? Specifically, L77 and HC both found that echo heights, areas, and durations were

all lognormally distributed. Distributions of convection using the classifications described below will be tested in terms of how well they fit the lognormal distribution.

3.1.2.a Vertical structure classification. Historically, the vertical structure of convection has been classified by echo top height. This approach is particularly useful to studies of convection that use IR brightness temperature as an estimate of cloud top height. However, any variations in the "internal" vertical structure of convection are masked using this approach. To illustrate this point, a schematic of two convective cells with similar heights, but different internal structures, is presented in Fig. 3.3. The outline of the 30 dBZ contour is highlighted, and the 0°C level is indicated. Because the two cells are the same height, they would have the same IR brightness temperature. However, their microwave emission characteristics are quite different. As Zipser (1994) and Petersen *et al* (1996) have pointed out, the presence of $\geq$30 dBZ reflectivity above the freezing level is often associated with lightning production and presumably larger water and/or ice contents above the freezing level. Since ice is a strong scatterer at short microwave wavelengths (85 GHz, for example) the larger quantities of supercooled liquid water and/or ice above the freezing level in the left-hand cell in Fig. 3.3 would cause upwelling microwave radiation to be scattered in many directions, thereby reducing the amount of radiation traveling in the direction of the satellite sensor (above). This enhanced scattering in the left-hand cell would result in a colder 85 GHz brightness temperature than would be observed from the cell on the right.

Because both echo top height and 30 dBZ contour height vary from cell to cell, convective features identified by the partitioning algorithm are described both in terms of their echo top heights, and in terms of their 30 dBZ contour heights (when reflectivity of this magnitude is present).

3.1.2.b Horizontal area classification. L77 and HC also classified echo by its areal extent. HC examined the relationship of (maximum) echo height and (maximum) echo area, and found that echo height increased with the log of echo area. This approach has the benefit of illustrating how feature area can impact the "vigor" of convective elements, namely by protecting the main updraft from the weakening effects of entrained low-θ_e air. A drawback to this approach, however, is that an echo composed of several convective cells must be classified by a single height, regardless of whether or not this height is

representative of *all* of the cells composing the echo. This problem is still encountered even when echo is partitioned into convective and stratiform components, since larger convective features are usually composed of several convective cores. The problem is illustrated in the schematic vertical cross section of radar echo in Fig. 3.4. The figure may be thought of either as a cross section of partitioned echo or as a cross section of unpartitioned echo at its maximum height and areal extent. Several convective cells of varying height and internal structure are shown in the cross section, yet the entire echo is described by the maximum height (and 30 dBZ contour height, in this study), which may be several kilometers taller than the mean height.

This approach also has the unfortunate characteristic of biasing the distribution of rainfall production (for example) towards the taller features. Furthermore, feature areas and the degree of feature merging is sensitive to subjective assumptions made in the partitioning algorithm. Another drawback to studying feature areas is that the effects of feature area are not obvious (and sometimes not realized by readers) when distributions of rainfall as a function of feature height are presented. In fact, there is a tendency for readers to interpret such plots as referring to individual convective *cells* rather than to groupings of cells. Despite these drawbacks, examining convective characteristics as a function of feature area has merit, particularly if one wishes to study vertical momentum transports as a function of feature area, or in determining what percentage of convective features can be resolved by satellite sensors.

An alternative approach to describing convection utilizes Cartesian "grid columns" and focuses on the "texture" of convective echo rather than the size of individual features. In this approach, echo height, 30 dBZ contour height (when present) and rainfall rate are determined for each grid column of convective echo, thereby eliminating the biases (and benefits) introduced by feature area. The main disadvantage of this approach is the decrease in certainty that convective rainfall observed at the 2 km level was produced by the processes taking place at higher levels. For example, in the 2×2 km horizontal grid spacing used in the study, even the slightest wind shear can advect raindrops or ice particles through several grid columns over just a few kilometers of depth. Because of this, rain falling through the 2 km level should be thought of as being "associated with", rather than "produced by" a grid column with

certain height characteristics. In contrast, stating that rainfall is "produced by" a convective *feature* is physically reasonable, since it is unlikely that a large portion of the rain falling underneath a convective feature was advected from a location beyond the feature limits.

Because each of these approaches have advantages and disadvantages, each will be used in this study in order to obtain a more complete picture of the distribution of convective echo during COARE.

3.1.3 Distributions of convective echo

3.1.3.a Distributions by height and 30 dBZ contour height. Convective rainfall production by feature height is a function of the number of features present within a given height bin, the areas of those features, and their rainfall rates. In this subsection, the number distribution of convective feature heights and 30 dBZ contour heights, and their contribution to convective area and rainfall are presented. The distributions of grid column heights and 30 dBZ contour heights and their contribution to convective rainfall is also presented.

Figures 3.5 through 3.7 show the distributions of feature height (top panels) for each cruise, the contribution to total convective area as a function of feature height (middle panels), and the contribution to convective rainfall as a function of feature height (bottom panels). The height distributions varied somewhat from cruise to cruise. Cruise 1 feature heights were strongly peaked in the 5-7 km height range, while the distributions of Cruise 2 and Cruise 3 were more broadly distributed among height bins.

The contribution to total convective area plots (panels b) also show variations from one cruise to the next. Convective area was broadly distributed among height bins during Cruise 1, with the main peak in the 6-9 km height range. During Cruise 2, convective area was also broadly distributed over all height bins, but peaked in the 10-11 km range. Finally, Cruise 3 convective area also peaked in the 10-11 km range, but with a more pronounced peak than is seen in Cruise 2. The convective area peak at shallower heights during Cruise 1 resulted from the relatively greater number of shallow features present during this cruise. By comparing panels a) and b) in Figs. 3.5 through 3.7, one concludes that the taller features were, on average, areally more extensive than shallow features, since the areal coverage distribution was

shifted towards taller features compared to the number distributions. During Cruise 1, however, the large number of shallow features present were sufficient to shift the area peak to shorter height bins.

How do these convective area distributions compare to those observed during GATE? Leary (1984) partitioned 25 hours of radar data from the 4–5 September 1974 GATE cloud cluster into convective and stratiform components using the technique of Churchill and Houze (1984), which is the manual partitioning technique upon which the partitioning employed herein is derived. Although this is a small temporal sample of convection, Leary states—based on comparisons with the results of Cheng and Houze (1979)—that her results are representative of typical GATE convection. Percent of *total* area values from Leary's Fig. 8 were divided by 0.63 (the fraction of area covered by convective echo) so they could be directly compared to Figs. 3.5 through 3.7. The resulting figure is presented as Fig. 3.8. Although there is a bias towards identifying features with even-numbered heights in the Leary paper, Fig. 3.8 suggests that features in the 11.5-12.5 km range contribute the most to convective area. This is approximately 1.5 km taller than the 10-11 km peak observed during Cruises 2 and 3 of COARE. If Leary's results are indeed representative of GATE convection, this suggests that a greater fraction of convective area in COARE is associated with shallower clouds than in GATE.

There are several possible explanations for the difference in convective area distributions. First, and probably foremost, the 4–5 September 1974 GATE case occurred in the trough of an easterly wave and represents only a 25-hour period, whereas the data from COARE is sampled over all conditions and over approximately 90 days. Another possible reason for the differences in convective area distribution by height may be linked to differences in sea surface temperatures (SSTs) between the two regions. SSTs in the COARE region are, on average, 3-4°C higher than those in the GATE study area. This difference results in higher water vapor mixing ratios in the boundary layer air the COARE region than in GATE (e.g., Williams and Renno, 1993). Given similar cloud condensation nuclei (CCN) populations, the drops in COARE would grow to larger sizes faster than those in GATE, the result being that drag forces from the larger water mass in COARE would reduce updraft strengths sooner (i.e., at lower levels) than would be experienced in GATE, potentially reducing the maximum attainable growth of the COARE convection.

Differences in radar sensitivity are not a likely factor in contributing to the area distribution differences, since the MIT radar was more sensitive than the radar aboard the *Oceanographer* (minimum detectable signal was -115 dbm compared to -100 dbm; Hudlow, 1979). Unfortunately, the Leary (1984) paper is the only one in the literature that presents convective area as a function of feature height, so a more thorough comparison of the two regions is not possible.

Panels c) of Figs. 3.5 through 3.7 present the contribution to total convective rainfall as a function of feature height. As with the area contributions, the rainfall distribution of Cruise 1 is also bimodal, with one broad peak in the 8-10 km height range and another in the 15-16 km height range. Rainfall distributions during Cruises 2 and 3 are both unimodal and peak at 16-17 km and 15-16 km, respectively. Cheng and Houze (1979) present convective rainfall distributions as a function of feature height for the GATE region. Their distribution for the entire period of GATE is also bimodal, but not in the same sense as the Cruise 1 rainfall distribution. Fig. 3.9 is adapted from their Fig. 2 for comparison. Contribution to total convective rainfall increases almost linearly with height up to the 12 km height bin, at which point it decreases rapidly and is followed by a second peak in the 15-16 km height range. Cheng and Houze attribute this bimodal distribution to one population of features whose tops do not extend above the level of neutral buoyancy (LNB; about 14 km for GATE), and one that does. During COARE, this bimodal distribution of rainflux in the tallest height bins is not seen. The LNB in COARE was typically located at a height of about 16 km, so it appears that some overshooting did occur. However, because the COARE analysis is based on "snapshot" distributions of echo height, rather than maximum height, as was done in Cheng and Houze (1979), there is a smooth transition from rainfall produced by features that do not and those that do ascend above the LNB. In general, convective rainfall contribution during COARE peaks in the 15-17 km height range, which is several km higher than the 12-13 km peak of GATE, possibly reflecting the approximately 2 km greater depth of the troposphere in the western Pacific compared to the eastern Atlantic.

In contrast to the distributions as a function of feature height, the number distributions and contributions to convective area and rainfall as a function of feature 30 dBZ contour height are strongly unimodal, exhibit narrower peaks, and show less variation from one cruise to the next. This more stable

behavior of convective distributions as a function of 30 dBZ contour height from one cruise to the next should make this an attractive variable for estimating convective rainfall rates from the TRMM satellite because, as will be demonstrated later in this chapter, near-surface rainfall rates are better correlated with 30 dBZ contour height than with echo top height.

As discussed in section 3.1.2.b, the distributions of Figs. 3.5 through 3.7 are all biased towards the tallest height bins. To study the effects of this bias, number and rainfall distributions based on convective grid column analysis are presented in Figs. 3.10 through 3.12. In these plots, number distributions and area distributions are identical, since all grid columns have the same area. In all three cruises, there are relatively more grid columns in the taller height bins compared to the feature distributions. This is simply a consequence of the fact that shallower features, while greater in number, tend to be smaller in area than taller features, so taller features represent a larger number of grid points. With the exception of the relative increase in taller height bins, the general shapes of the number distributions between feature and grid column perspectives are not drastically different.

The same cannot be said for the distribution of convective rainfall by height, however. In all three cruises, the height of peak rainfall contribution has decreased by several height bins, which emphasizes the fact that the maximum height of a given feature is often not representative of the heights of all convective cells contained within that feature. A similar shift in the height of peak rainfall contribution is seen in the 30 dBZ grid column height analysis, although the shift is not as dramatic as that for echo top height. Number distributions of 30 dBZ contour heights in Figs. 3.10 through 3.12 are only slightly different than those in Figs. 3.5 through 3.7.

Figs. 3.10 through 3.12 can be used to estimate the fraction of convective precipitation associated with a given IR brightness temperature and test assumptions made concerning what fraction of rainfall is associated with a given threshold. For instance, in constructing a climatology of precipitating systems over the maritime continent region, Mapes and Houze (1993) focused on IR brightness temperatures less than or equal to 208K which they state "matches the instantaneous precipitation area in radar-sampled mature MCSs fairly well." In the COARE region, 208K corresponds to an altitude of about 13-13.5 km. Considering that radar-estimated cloud top heights can be 1-2 km less than those observed by IR sensors

(Cifelli *et al.*, 1996), the total convective rainfall contributed by grid column heights less than 11 km were summed to determine how accurately 208K estimates rainfall. This procedure reveals that the percentage of convective rainfall associated with cloud tops warmer than 208K is 58.1, 56.0, and 68.0% for Cruises 1, 2, and 3, respectively. Therefore, the presence or absence of very cold cloud is not always a reliable indicator of convective activity.

3.1.3.b Distributions by feature area. The distributions of and rain contributions by feature area (at the 2 km height level) are presented in Fig. 3.13. In general there is a greater number of small features than large features. However, there are relatively few features in the 10-15 and 25-30 km diameter bins. This behavior may result from the particular partitioning assumptions made, or there may be some physical basis for it. Based on the partitioning process described in Appendix A, however, there is no obvious reason why this behavior would result from the partitioning process.

A *possible* physical explanation of this behavior may be found by considering the maximum possible dimension of any individual convective core. A cursory visual inspection of several horizontal cross sections (not shown) reveals that there are very few individual convective cells with diameters in excess of about 20-25 km, suggesting that this is an upper limit to the areal dimension of single cells (this hypothesis is examined further in section 3.2). Features composed of more than one cell tend to be associated with mature and intense convection, which are probably close to this maximum possible dimension. Therefore, equivalent diameters of such features would tend to occur in multiples of 20-25 km. By the same reasoning, features with equivalent diameters in the 10-15 and 25-30 km range would contain approximately 1.5 and 2.5 mature convective cells—an unlikely scenario, since the partitioning algorithm does a good job of capturing entire convective cells in the convective partition. As features become larger, there is a greater tendency for smaller developing cells to be included in the features, thereby somewhat smoothing out the "sawtooth" behavior of the distribution with increasing feature size.

The contribution of rainfall as a function of feature area reveals that the largest features make a disproportionate contribution to total convective rainfall. This is a consequence of both their larger area and the tendency for harder raining cells to be contained in larger features.

3.1.3.c Quantitative characterization of convective distributions. Through the analysis of L77 and HC, it has been demonstrated that distributions of maximum radar echo height and area (over the course of the *unpartitioned* echo lifetime) are lognormally distributed. These distributions, then, should be thought of as representing the distribution of *maximum possible* echo height and area. It may be more meaningful, however, to consider the distributions of *instantaneous* convective echo heights and areas. For example, convective towers diabatically heat the atmosphere during all stages of development—not just when they reach their maximum height or area. Furthermore, passive microwave rainfall estimates are based on instantaneous—not maximum—distributions of cloudiness. Determining an appropriate model to describe the observed distributions of convective cloudiness should be of use both for developing convective parameterizations and for improving passive microwave rainfall retrieval algorithms.

Cumulative frequency distributions of convective feature top height and 30 dBZ contour height are plotted in log-probability format in Figs. 3.14 and 3.15, respectively. In this depiction, the closer the data points come to lying on a straight line, the closer the distribution is to normal. The straight lines are the cumulative probability curves for a normal distribution having the same mean and standard deviation of the logarithm of height as the observed distributions. The observed distributions are very close to lognormal up to heights of about 11.5 km, where they begin to deviate from the normal curve. This is essentially the same height where the data presented in L77 and HC began to deviate from lognormal. Performing the Chi-squared test for goodness of fit indicates that the feature height distributions from all three cruises fit the lognormal distribution at the 95% confidence level. Therefore, the monthly average instantaneous distributions of partitioned feature height are adequately described by the lognormal distribution. Table 3.2 compares the means and standard deviations of the logarithm of height between the GATE and COARE. The COARE means are slightly higher than the GATE means, since the troposphere is deeper in the COARE region than in GATE. The standard deviations are somewhat larger for COARE, most likely due to the greater number of data points that make up the COARE data set (i.e., with more data points, there is a greater chance of sampling extreme outliers than with a subset of convective features, as was done in HC).

Table 3.2 Means and standard deviations of the logarithms of maximum echo height (GATE) and instantaneous feature height (COARE).

Vickers cruise or GATE phase	GATE (values from HC)		COARE	
	mean	standard deviation	mean	standard deviation
1	0.55	0.17	0.72	0.27
2	0.61	0.24	0.75	0.27
3	0.63	0.21	0.72	0.28

As described in subsection 3.1.3.a, the distribution of features as a function of 30 dBZ contour height appears to be approximately normal. The cumulative frequencies as a function of this variable, then, are not transformed to logarithmic height coordinates before plotting on the probability axis. For all three cruises, the 30 dBZ contour heights fit the normal distribution quite well up to a height of about 10.5 km at which point they begin to deviate from a true normal distribution. Data from all three cruises pass the Chi-squared test for goodness of fit at the 5% level of significance. There is little variability in the distributions from one cruise to the next.

Finally, distributions of grid column heights and 30 dBZ contour heights are examined (not shown). The grid column height distributions are also well described by the lognormal distribution (passing the Chi-squared test at the 5% significance level), but with a slightly larger mean (3-cruise average of 0.85), reflecting the relatively higher "concentration" of tall grid columns as compared to features, and smaller standard deviation (3-cruise average of 0.20). As with the feature height distributions, the grid column heights begin to deviate from a truly lognormal distribution at about 11.5 km. Grid column 30 dBZ contour heights are again nearly perfectly normally distributed, but exhibit smaller deviations from a straight line at the tallest heights.

This quantitative analysis of echo height distribution shapes suggests that, despite differences in analysis techniques, convective echo heights—both maximum and instantaneous—are lognormally distributed, and that such a distribution adequately describes convective heights for both partitioned and unpartitioned echo.

Whereas partitioning radar echo into convective and stratiform components seems to have little effect on the distribution of echo heights, the same cannot be said concerning echo area distributions, as

was suggested in subsection 3.1.2.b. Cumulative frequency distributions of feature area are not presented since only those of Cruise 3 were approximately lognormal (passing the Chi-square test at the 5% level of significance). Unlike feature height, feature area is quite sensitive to the assumptions made regarding the areal extent of convection in the partitioning algorithm. For example, increasing the assumed radius of convective echo surrounding a convective core by as little as 1 km can lead to noticeable increases in the degree to which individual convective cells are merged together into a single feature. The effects of convective echo merging on area distributions will be discussed further in subsection 3.3.3.

3.2 Variability of convective properties within individual features.

Differences in the shapes of distributions between feature attributes and grid column attributes underscores the fact that, for convective cells grouped into areally extensive convective features, the maximum height or 30 dBZ contour height is not necessarily representative of all the cells contained within that feature (see schematic illustration in Fig. 3.4). It is of interest, then, to examine how properties such as height, 30 dBZ contour height, and rainfall rate vary within individual convective features. This is accomplished by computing the mean and standard deviation of height, 30 dBZ contour height, rainfall rate, and fractional area exceeding 30 dBZ *within each identified feature*, and plotting these results as a function of the features equivalent diameter.

3.2.1 Variability of echo top height

The distributions of mean and standard deviation echo top height for each cruise are presented in Fig. 3.16. These plots are similar to scatter plots in which each feature that is characterized by an equivalent diameter and a mean (or standard deviation) height would represent a single point on the plot. However, the approximately 60,000 features catalogued in each cruise would result in so many points being plotted as to obscure the distribution of features. Therefore, contours of the percent of total features are drawn instead. Discussion of these plots will focus on the "envelope" of data points (the 0.1% contour) and the modal mean or standard deviation (not plotted), which follows the axis of maximum relative frequency.

For all three cruises, the 0.1% contour reveals that the maximum mean height within any given feature is about 13-14 km *regardless of feature area*. For equivalent diameters greater than about 30 km, the maximum mean height decreases slightly, suggesting that features in this size range may be composed of several convective cells in various stages of development and characterized by a variety of heights. On average, however, mean echo top height tends to increase as a function of feature area, suggesting that larger features are better able to protect their main updrafts from entraining drier environmental air, and therefore attain greater heights. To a first approximation, it appears that modal mean feature height increases logarithmically with equivalent diameter.

Variability of echo top height (represented by the standard deviation) reveals a strong increase in this variability from 0 to 25 km equivalent diameter features. Beyond this range, the mean standard deviation levels off to approximately 1.5 km. This behavior can also be approximately described as a logarithmic increase of standard deviation with increasing diameter. The envelope of variability as a function of equivalent diameters also increases up to about 25 km, then decreases somewhat. The decrease in the size of the variability envelope is most likely due to the dominance of a few tall and large cells contained within the largest features. In other words, while the features may include several small and shallow cells, they contribute fewer data points to the total, so their influence on the standard deviation calculation is small.

3.2.2 Variability of 30 dBZ contour height

The distributions of mean and standard deviation feature 30 dBZ contour height are presented in Fig. 3.17. These distributions are in marked contrast to those of feature height. Whereas the mean feature height distributions are broad and increase with feature size, mean 30 dBZ height distributions are narrow and nearly invariant over the spectrum of feature sizes. The modal mean is centered at the 3-4 km height bin for all cruises and feature sizes, while the maximum observed mean height is 5-6 km—approximately the same height as the 0°C level. The fact that the distributions are so similar for each cruise—particularly for Cruises 1 and 2 which experienced different phases of the intraseasonal

oscillation—suggests that, on average, atmospheric conditions over the western Pacific warm pool are not conducive to the generation of widespread vertically intense convection, as suggested by the height of the 30 dBZ contour. Furthermore, the location of the 0°C level with respect to the mean 30 dBZ contour height distribution is consistent with the rather infrequent observations of lightning in this region compared to continental regions.

The distributions of the standard deviations of 30 dBZ contour height are similar to those for feature height. Namely, the variability of 30 dBZ contour height tends to increase approximately logarithmically with feature area. The conclusion drawn from the both the mean and standard deviation of 30 dBZ contour height plots is that even though large-scale conditions may not be favorable to for the formation of vertically intense and electrified convection, convective-scale circulations may produce conditions that allow for the development of vertically intense convection.

3.2.3 Variability of rainfall rate

Distributions of mean and standard deviation rainfall rate as a function of feature size are presented in Fig. 3.18. Unlike the distributions of mean feature height, which increase logarithmically with increasing feature diameter, the distributions of mean rainfall rate appear to increase exponentially with increasing diameter, with the exponential curve becoming nearly vertically oriented in the 25 to 30 km diameter range. In further contrast to the mean feature height distributions, there is significantly more scatter of data points about this axis of maximum relative frequency for the rainfall rate distributions.

Why should rainfall rates maximize for features with 25 to 30 km equivalent diameters? As discussed in subsection 3.1.3.b, the distribution of feature diameters appear to be quantized in multiples of 20-30 km, suggesting a maximum convective cell dimension somewhere in this size range. The fact that mean rainfall rates tend to maximize in the 25 to 30 km size range provides additional support to this argument, since features composed of several convective cells should contain relatively larger amounts of weaker "connective" echo between the main convective cores, whereas individual cells would have less, thereby increasing their area mean rainfall rate. The similar distribution of standard deviation rainfall

rate (exponential increase, with axis of maximum relative frequency nearly vertically oriented in the 25 to 30 km diameter range) is consistent with these arguments.

3.2.4 Variability of fractional area with intense rainfall

The distribution of the fraction of echo area at the 2 km height level with reflectivity in excess of 30 dBZ is shown in Fig. 3.19. The lack of any obvious trend as a function of feature size indicates that convective feature size has little effect on the intensity of rainfall. This point will be addressed further in section 3.4.

3.3 Cumulative frequency distributions of convective rainfall by feature attribute

Although the relative frequency distributions of convective rainfall presented in section 3.1 illustrate the breadth and shape of these distributions, they are not as well suited to answering the question of which features are the most important to convective rainfall production as are cumulative frequency distribution plots.

3.3.1 Rainfall production as a function of height

Fig. 3.20 presents the cumulative frequency distribution of accumulated convective rainfall as a function of feature height and grid column height. These plots are constructed by computing the cumulative frequency distribution of the *number* of features contained in each height bin and the cumulative frequency distribution of *convective rainfall* contained in each height bin. Each height bin then has two cumulative frequencies associated with it, which are then plotted as a scatter plot, with a line joining each data point to resemble a continuous distribution. A common method for assessing the relative importance of a subset of features as defined by a certain attribute is to determine the cumulative distribution of the feature attribute that corresponds to the median rainfall value (i.e., 50%).

For rainfall production as a function of feature height, the tallest 5% of features produce half of the convective rainfall. This corresponds to features as tall or taller than 13.0, 13.5, and 12.9 km for Cruises 1, 2, and 3, respectively. In contrast, when rainfall production is classified by grid column height,

the median rain volume corresponds to the tallest 27% of grid columns, or grid columns as tall or taller than 10.1, 11.0, and 9.6 km for Cruises 1, 2, and 3, respectively. The differences in median rainfall height between the feature and grid column distributions further highlights the bias of the feature analysis towards taller heights.

One advantage of studying the contribution to convective rainfall as a function of grid column height is that the effects of feature area that are present in the top panel of Fig. 3.20 have been eliminated. For example, in Fig. 3.20a (the *feature* height analysis), it is not clear whether tall features produce more rain because they are raining harder or because they are more areally extensive. The fact that less than half of the tallest grid columns produce half of the convective rainfall suggests that taller features do indeed rain harder, as will be seen in the next section.

3.3.2 Rainfall production as a function of 30 dBZ contour height

The cumulative distributions of accumulated convective rainfall as a function of 30 dBZ contour height are presented in Fig. 3.21. Cumulative convective rainfall is less than 100% because some convective rainfall is produced by features with 2 km reflectivity values less than 30 dBZ (see captions of Figs. 3.5 through 3.7 and 3.10 through 3.12). To find the 30 dBZ contour height that corresponds to 50% of rainfall production by the *tallest* contours, 50% is subtracted from the percentage of *total* convective rainfall represented by features with 2 km reflectivity in excess of 30 dBZ. For example, from Fig. 3.5, such features account for 93% of convective rainfall, so the median rainfall percentage associated with the tallest 30 dBZ contour heights for Cruise 1 is 43%. Following this procedure for all three cruises reveals that the tallest 13, 17, and 19% of feature 30 dBZ contour heights were associated with production of half the convective rainfall for Cruises 1, 2, and 3, respectively. These fractions correspond to 30 dBZ contour heights of 8.0, 7.3, and 7.4 km for each cruise.

For the distribution of grid column 30 dBZ contour heights, half the *total* convective rainfall (from all columns, regardless of their reflectivity value at 2 km) corresponds to cumulative rainfall totals of 23.1, 16.7, and 19.1% for Cruises 1, 2, and 3, respectively. From these figures, it is seen that the tallest 50, 64, and 58% of 30 dBZ columns produced half of the rainfall, corresponding to 30 dBZ contour

heights as tall or taller than 4.2, 3.5, and 3.3 km for Cruises 1, 2, and 3, respectively. The fact that the *grid column* 30 dBZ heights that are associated with 50% of the convective precipitation are only half as tall as the *feature* 30 dBZ heights suggests that extensions of the 30 dBZ contour to heights several kilometers above the freezing level occur over just a few grid columns, which corresponds to convective scale vertical motions. Therefore, even though large scale atmospheric conditions may not favor widespread vertically intense convection, favorable circumstances for intense convection are apparently generated on the convective scale.

3.3.3 Convective area and rainfall production as a function of feature area

For the purposes of comparison to other studies, cumulative convective area is presented in this section as well as cumulative convective rainfall. Fig. 3.22a presents cumulative frequency distributions of accumulated convective area and rainfall as a function of feature area. The plots of accumulated convective area allow comparison of the partitioned feature areas obtained from this study to those of unpartitioned echo areas of L77 and HC.

Somewhat surprisingly, the COARE accumulated area distributions are very similar to those presented by L77 (Fig. 3.22a), with the largest 15-17% of feature areas accounting for half of the total convective area. In contrast, the largest 4% of GATE echoes composed half of the echo area. HC have attributed the difference between their results and those of L77 to different sensitivities of the radar used in each study. The radar aboard the *Oceanographer* during GATE was quite sensitive to low rainfall rates, so "pockets" of convective echo were connected by large areas of weak stratiform rainfall. In contrast, the radars used in the work of L77 were less sensitive to low rainfall rates, so there tended to be a greater number of smaller and disconnected echoes, since the weakest rainfall rates that would have connected these echoes were not detectable. While the MIT radar deployed in COARE was comparably sensitive to that aboard the *Oceanographer* in GATE, the partitioning processes eliminated the "connecting" stratiform rainfall, leaving a population of features similar to those studied by L77. These differences in the curves of accumulated area from one experiment to the next highlight the sensitivity of convective echo calculations to radar sensitivity and to assumptions made in the partitioning process, and

make it difficult to asses if any of the differences are the result of differences in the environments of the systems studied.

Cumulative rainfall distributions as a function of feature area are presented in Fig. 3.22b. The effects of quantized feature areas depicted in Fig. 3.13 can be seen as "kinks" in the accumulated rainfall curves. From this plot, it is seen that the largest 17, 20, and 22% of convective features account for 50% of the total convective rainfall. These percentages correspond to equivalent diameters of 55.5, 52.0, and 50.0 km for Cruises 1, 2, and 3, respectively. This type of analysis is useful in estimating what percentage of convective rainfall can be resolved by satellite sensors with various surface footprint sizes. For example, the 11 km footprint size of IR channel of the Geostationary Meteorological Satellite (GMS) can easily resolve more than half of the convective precipitation. However, features of this size are often accompanied by a large cirrus anvil, which greatly hinders identification of convective and stratiform cloud from IR methods. Microwave channels are better able to discriminate between convective and stratiform cloud, but typically have larger footprints than the GMS IR channel. The influence of feature area on passive microwave rainfall retrievals will be discussed more completely in Chapter 5.

3.4 Rainfall intensity as a function of feature attribute

In the previous section, the contribution to monthly rainfall totals by features of various heights and areas was studied. This type of information is useful for studies of heating budgets of precipitating systems and for Area-Time-Integral (ATI) techniques of estimating rainfall (i.e., Doneaud *et al.*, 1984; Atlas and Bell, 1992). Passive microwave retrieval algorithms however, such as those that are being developed for use with the TRMM satellite, require information on rainfall *rate*. The purpose of this section is to examine which features rain the hardest, and how rainfall rate varies among features of a given vertical structure.

3.4.1 Rainfall rate variations by height and 30 dBZ contour height

The distributions of rainfall rate as a function of feature and grid column height for each cruise are presented in Fig. 3.23 (note the difference in scale for rainfall rate in each panel). For each height

bin, rainfall rates were weakest during Cruise 2, consistent with the less intense vertical reflectivity and thermal buoyancy profiles of this cruise (see Figs. 3.1 and 3.2). Rainfall rates increase gradually with height up to the 12-13 km height bin, at which point they increase at a faster rate. Note that rainfall rates in the 6-11 km range during Cruise 1 were approximately 50% higher than those during Cruises 2 and 3. As will be discussed in the following chapter, this is likely related to subtropical dry tongues being advected in the IFA and phase of the ISO.

The distribution of rainfall rate as a function of grid column height increases similarly to the distribution by feature height. Mean rainfall rates are higher since no areal averaging is performed in this analysis. Note that rainfall rates decrease dramatically in the tallest height bin. This is most likely the result of wind shear, which would result in the tallest grid columns not being located directly over maximum surface reflectivity grid points, but may also be a consequence of side lobe contamination. A random sample of 100 volumes revealed that side lobe effects were present in 3% of the volumes, and artificially increased echo top heights by 2-4 km. This effect was most often seen when intense convection was within 40 km of the radar and affected only a few cells within the same range. Therefore, only a small fraction of the convective echo analyzed in these volumes were actually affected by side lobe effects. The margin of error in this random sample is ±3%, so side lobe effects may be present in as many as 6% of the volumes analyzed.

Fig. 3.24 shows mean rainfall rate as a function of feature and grid column 30 dBZ contour heights. Again, rainfall rates from Cruise 2 are less than those observed for either Cruise 1 or Cruise 3. For Cruise 1, rainfall rate continually increases with height, but it begins to decrease in the 9-11 km height bins for Cruises 2 and 3. This behavior is most likely tied to differences in the horizontal organization of precipitating systems between Cruise 1 and Cruises 2 and 3. Rickenbach (1995) has shown that Cruise 1 was characterized by more days of isolated convective features while Cruises 2 and 3 observed more systems with linearly organized convective elements. When the partitioning is applied to each of these situations, the linearly organized systems contain more features that are composed of several convective cells compared to the systems of Cruise 1. Therefore, there is a greater likelihood that the maximum 30 dBZ contour height is not representative of the other cells composing a clustered, linear

feature compared to that of an isolated feature composed of only one to a few cells. Rainfall rate as a function of *column* 30 dBZ height also decrease slightly in the 9-11 km height range, but not as drastically as is seen in the feature analysis. As with rainfall rate as function of echo top height, this decrease is most likely due to the effects of shear and/or side lobes.

Upon seeing the systematic increase of rainfall rate with echo top height or 30 dBZ contour height, it is tempting to conclude that individual convective cells follow this same trend. It should be kept in mind, however, that the rainfall rates in Fig. 3.24 are *averages* computed from thousands of convective features. The *distribution* of rainfall rates as a function of feature height and 30 dBZ contour height are presented in Fig. 3.25. Although the general trend of increasing rainfall rate as a function of feature height can be seen, the distributions of rainfall rate are quite broad. It is most broad for feature heights greater than 5 km and narrows somewhat with decreasing feature height. Based on the widths of these distributions, there is probably almost no correlation between feature height and rainfall rate for features greater than 5 km tall, and only weak correlation for features shorter than this. Therefore, cloud top height, especially for tops greater than about 5 km, is not a very reliable indicator of surface rainfall rate for individual features.

Interestingly, the distributions of rainfall rate as a function of feature 30 dBZ height are much more peaked than those by height, suggesting that the correlation between rainfall rate and 30 dBZ contour height may be higher than that for echo top height. This is potentially useful information for TRMM, which will use a 3-cm radar to profile tropical precipitation. Attenuation at this wavelength can be extreme, so the radar may not be able to measure rainfall rates close to the surface in heavily raining convective systems. However, if it is used to estimate the height of the 30 dBZ contour, it may at least be able to provide some constraints on the rainfall rates calculated by the passive microwave retrieval algorithms.

3.4.2 Rainfall rate variations by feature area

Fig. 3.26 shows the relationship of mean rainfall rate to feature area. Rainfall rate generally increases with increasing area, but not as rapidly as it does with height or 30 dBZ contour height. Also,

the mean rainfall rate for each feature bin is about an order of magnitude less than those classified by height. This lower mean rainfall rate suggests that the distribution of rainrates as a function of feature area is quite broad, and that feature area plays only a minor role in enhancing rainfall intensity compared to height or 30 dBZ contour height.

3.5 Characteristics of vertically intense convection

Up until now, the vertical structure of convection has been discussed either in terms of its height, or in terms of its 30 dBZ contour height. Fig. 3.3 illustrated two possible combinations of these two variables within a single convective cell. But what combination of echo top height and 30 dBZ contour height is most prevalent over the warm pool? The answer to this question should provide some insight into the vertical distribution of convective heating and provide constraints for and insights into the passive microwave rainfall retrieval problem.

To study the distribution of vertical structures observed during COARE, contoured relative frequency plots (analogous to scatter plots) of the distribution of features as a function of feature height *and* 30 dBZ contour height were constructed. These frequency plots are presented in Fig. 3.27a-c. Grid column distributions are presented in Fig. 3.27d-f. Presented in this manner, intensity of vertical development increases as one moves from the lower left corner of the plot to the upper right corner.

Despite the clustering of points in the 6-8 km height and 3.5-4.5 km 30 dBZ height ranges, any given feature or grid column height is associated with a wide range of 30 dBZ contour heights. Considering the close relationship between rainfall rate and 30 dBZ contour height (Fig. 3.25), this broad range of 30 dBZ contour heights for a given echo top height in part explains the large variability of rainfall rate as a function of feature height. Note that the axis of maximum relative frequency is nearly horizontally oriented for 30 dBZ heights less than 5 km, then becomes nearly vertically oriented for 30 dBZ heights greater than 5 km. Physically, this implies that there is almost no preferred height for the 30 dBZ contour when it is located below the freezing level, but it rarely exceeds heights greater than 6-7 km when it does extend above the freezing level.

Fig 3.28 presents the fraction of convective rainfall produced by features and grid columns of a given vertical structure. The bias towards taller heights in the feature analysis (panels a-c) is quite apparent. Comparison of the grid column distributions (Fig. 3.27) with the rainflux figures reveals that the offset between maximum relative frequency and maximum rainfall production is less than it is in the feature analysis. The differences in rainfall production as a function of feature height for each cruise that were seen in Figs. 3.5 through 3.7 are also present in this analysis. For example, the feature analysis (panels a-c) reveal that the bulk of the convective rainfall is produced by features with cloud top heights in the 12-16 km range and 30 dBZ contour heights in the 6-8 km range. However, Cruise 1 rainfall production has a distinct tail extending into regions of shallower and less vertically intense rainfall, reflecting the greater numbers of shallow convection present during this cruise. Although less distinct, a similar tail is seen in the grid column analysis. Comparing the distributions of rainflux from one cruise to the next reveals that rainfall production as a function of vertical structure varies over time scales at least as short as one month. These variations should therefore be taken into consideration when using satellite data to estimate monthly rainfall totals.

It is now evident that the vertical intensity of convection (as observed by the height of the 30 dBZ contour) varies widely with cloud top height. A follow-up question to ask at this point is: How does the vertical structure of convection vary as a function of feature area? To answer this question, the mean equivalent diameter of all features contained within each height-30 dBZ height bin was computed. Contours of mean equivalent diameter are presented in Fig. 3.29. . On average, the more vertically developed features are associated with areally larger features, presumably because a larger feature is better able to protect its main updraft core from entraining environmental air. Alternatively, more intense features may be associated with larger (in a cross section sense) updraft columns, and therefore produce larger features. However, given the likelihood that features with diameters greater than about 25 km are composed of multiple cells, the first explanation (larger features being better able to protect individual updraft cores) is the more likely scenario.

3.6 Summary of findings

Statistics of mean reflectivity profile, height, 30 dBZ contour height, rainfall rate, and area of nearly 200,000 convective features were compiled to determine the mean state of convection during TOGA COARE and to determine how mean properties varied over monthly time scales. The vertical structure of the mean convective reflectivity profiles appears to be related to the magnitude of thermal buoyancy, and therefore upward motion, during raining events. The more convectively unstable environment during precipitation events during Cruise 1 allowed for the development of a more vertically intense reflectivity profile than was observed for Cruises 2 or 3, even though more rain fell during Cruises 2 and 3.

The distribution of convective echo heights varied from cruise to cruise, with Cruise 1 being characterized by proportionately more shallow echoes than were present during Cruises 2 and 3. This resulted in shallower cells contributing more to total convective area and rainfall during Cruise 1 than in the other two cruises. The greater contribution to rainfall by shallow cells during Cruise 1 combined with the greater degree of thermal buoyancy suggest that factors other than CAPE often controlled the vertical development of convection during this cruise. More than half of the convective rainfall was associated with echo with cloud top temperatures warmer than 208K—a finding that is inconsistent with the assertion of Mapes and Houze (1993) that the area of 208K reasonably matches the area of radar-observed precipitation.

As is true with echo from a variety of locations and conditions, the distribution of echo top height is well described by a lognormal distribution. This is true despite the fact that previous work on this topic dealt with unpartitioned echo and classified echo top height by its maximum value over the course of the echo lifetime, whereas this study deals with *instantaneous* distributions. The distributions of 30 dBZ contour height are approximately normal. The distribution of partitioned convective echoes were only approximately lognormally distributed during Cruise 3. Slightly different assumptions made in partitioning radar echo into convective and stratiform populations can and do result in very different distributions of features by area due to increases or decreases in the degree of merging of several cells into a single large feature. This sensitivity to partitioning assumptions should be considered when discussing such distributions.

The variability of echo top height within a given feature generally increases with increasing area, although the distribution of mean heights is quite broad. In contrast, mean 30 dBZ heights show essentially no variation as a function of feature area and are narrowly distributed. Deviations from this mean, however, tend to increase with increasing area. Mean and standard deviation rainfall rates maximize for features in the 20-30 km diameter bin, which roughly corresponds to the maximum attainable area for any single convective cell, as determined by the partitioning technique employed herein.

On average, the intensity of rainfall increases with increasing echo top height, but varies considerably from one feature to the next. Mean rainfall rate also increases with increasing 30 dBZ contour height, but this distribution of rainfall rates is much narrower than it is for feature top height, suggesting that the height of the 30 dBZ contour may be a better proxy for instantaneous surface rainfall rate than echo top height.

Analysis of the vertical structure of convective features reveals that vertical development, or intensity (for which 30 dBZ contour height is a proxy), varies considerably with echo top height. Furthermore, the 8 km height appears to be a "soft" limit on the height of the 30 dBZ contour for most warm pool convection. Convection that does reach tall heights with intense internal vertical structures are typically associated with areally more extensive echo.

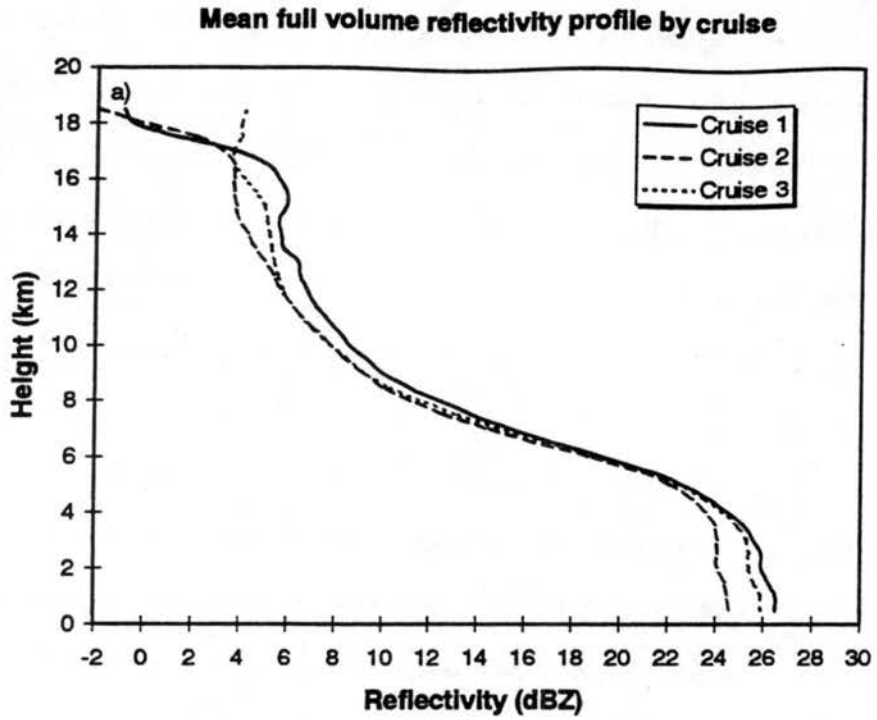

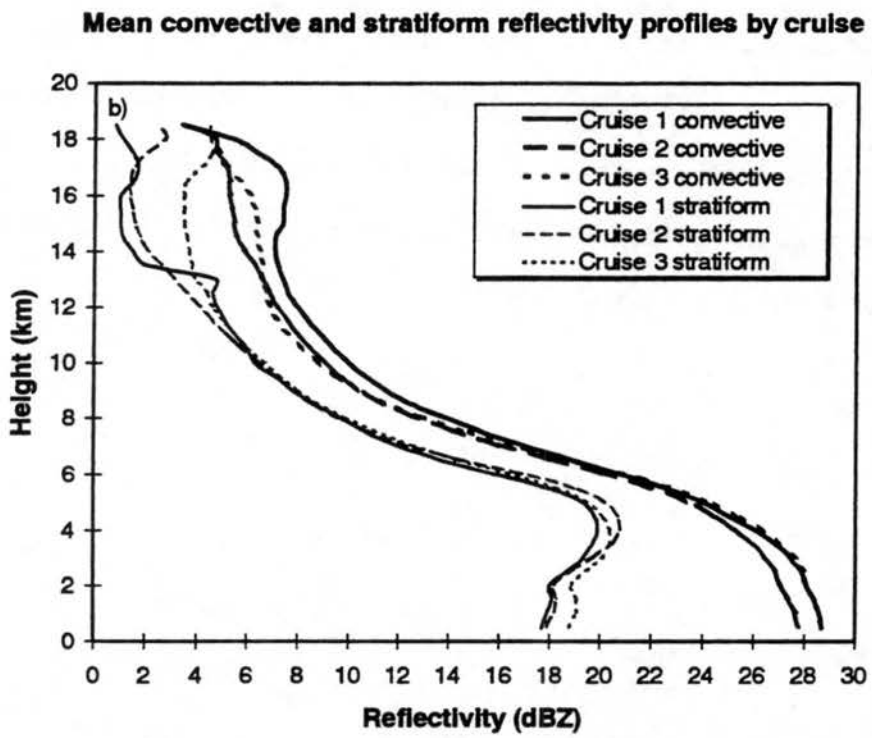

Fig. 3.1. Mean reflectivity profiles averaged by cruise for a) full (unpartitioned) volumes and b) convective and stratiform volumes. Side lobe effects can be seen above 14 km.

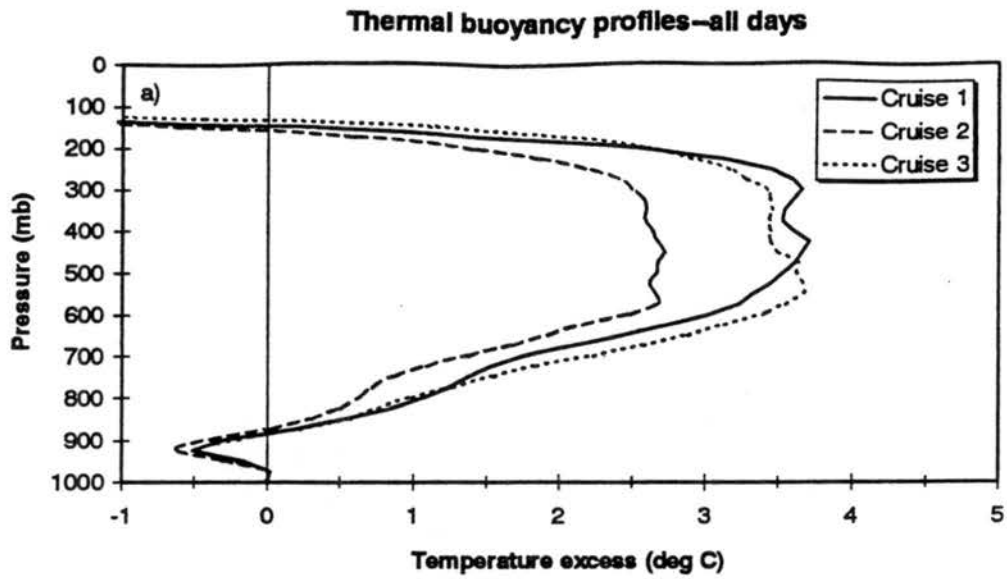

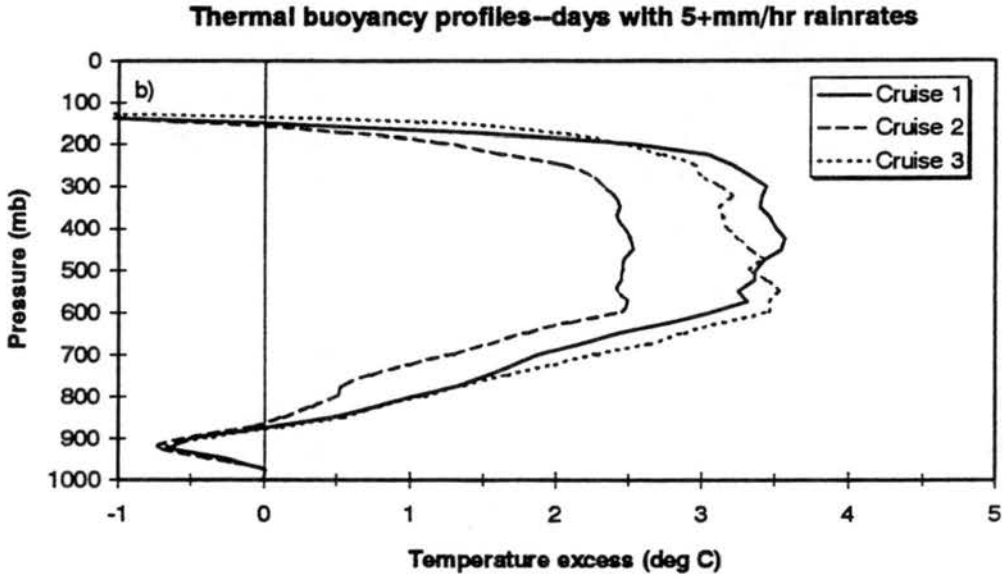

Fig. 3.2 Profiles of mean thermal buoyancy (defined as the difference between parcel and environmental temperatures) during COARE for a) all days, and b) days with precipitation rates $\geq$ 5 mm/day.

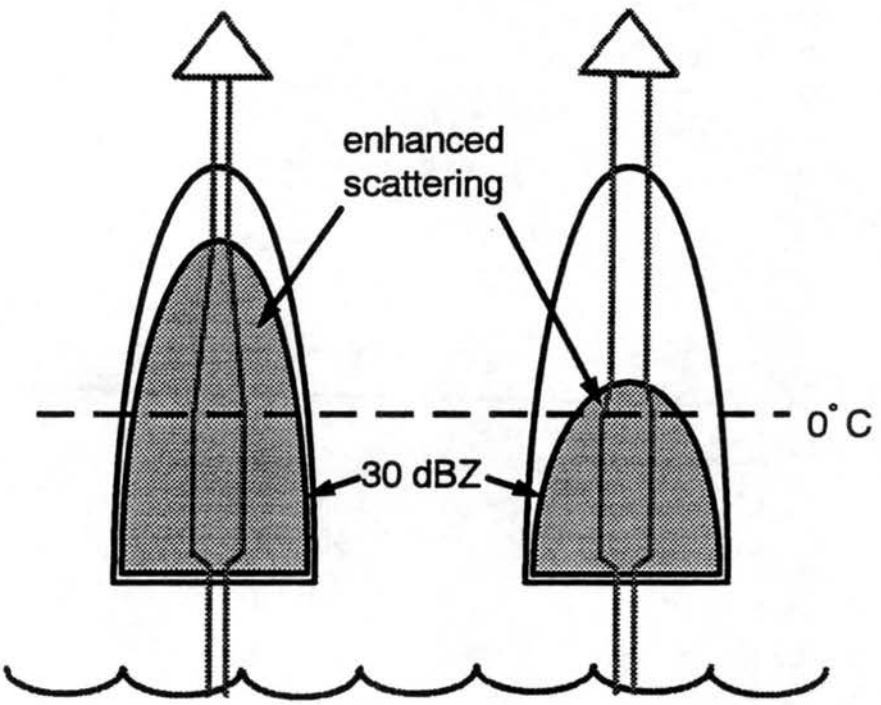

Fig. 3.3. Schematic illustration of two convective features interacting with upwelling 85 GHz radiation (radiant energy at this frequency is proportional to the width of the open gray arrows). The features are the same height, yet have different internal structures. The left-hand feature has a higher 30 dBZ contour than the right-hand feature, corresponding to greater liquid and ice water masses above the freezing. Because ice is a strong scatterer at 85 GHz, the left-hand feature produces a colder 85 GHz brightness temperature than the right-hand feature.

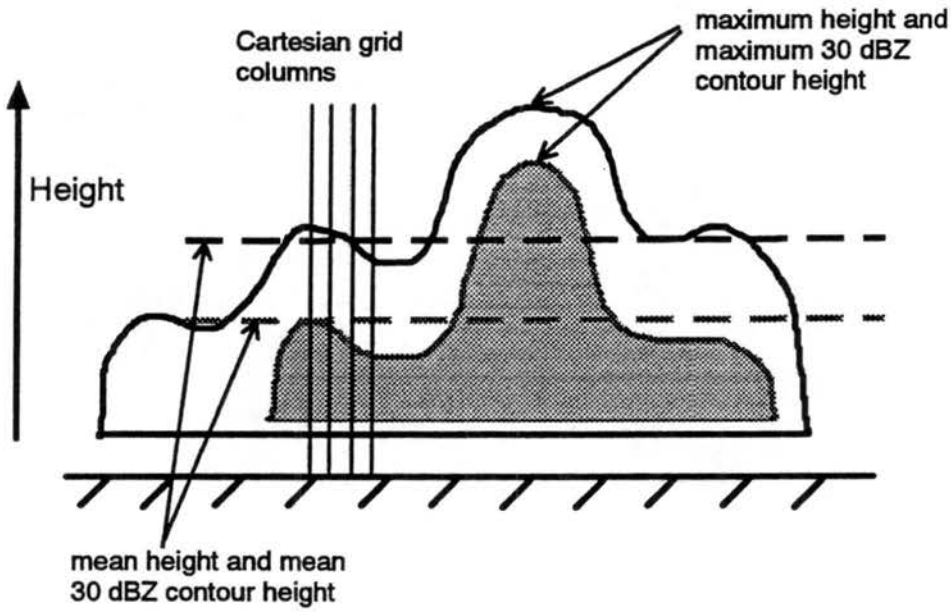

Fig. 3.4. Schematic vertical cross section of a convective feature composed of four convective cells. Black line corresponds to the 0 dBZ contour; gray line corresponds to 30 dBZ. Reflectivity greater than 30 dBZ is shaded in light gray. Convective feature heights, 30 dBZ contour heights, and rainfall associated with convective features are categorized by their *maximum* height, which may be several kilometers higher than their mean heights (heavy dashed lines). An alternative method of describing convective echo is to record the height, 30 dBZ contour height, and rainfall of each Cartesian grid column, samples of which are illustrated by thin vertical lines.

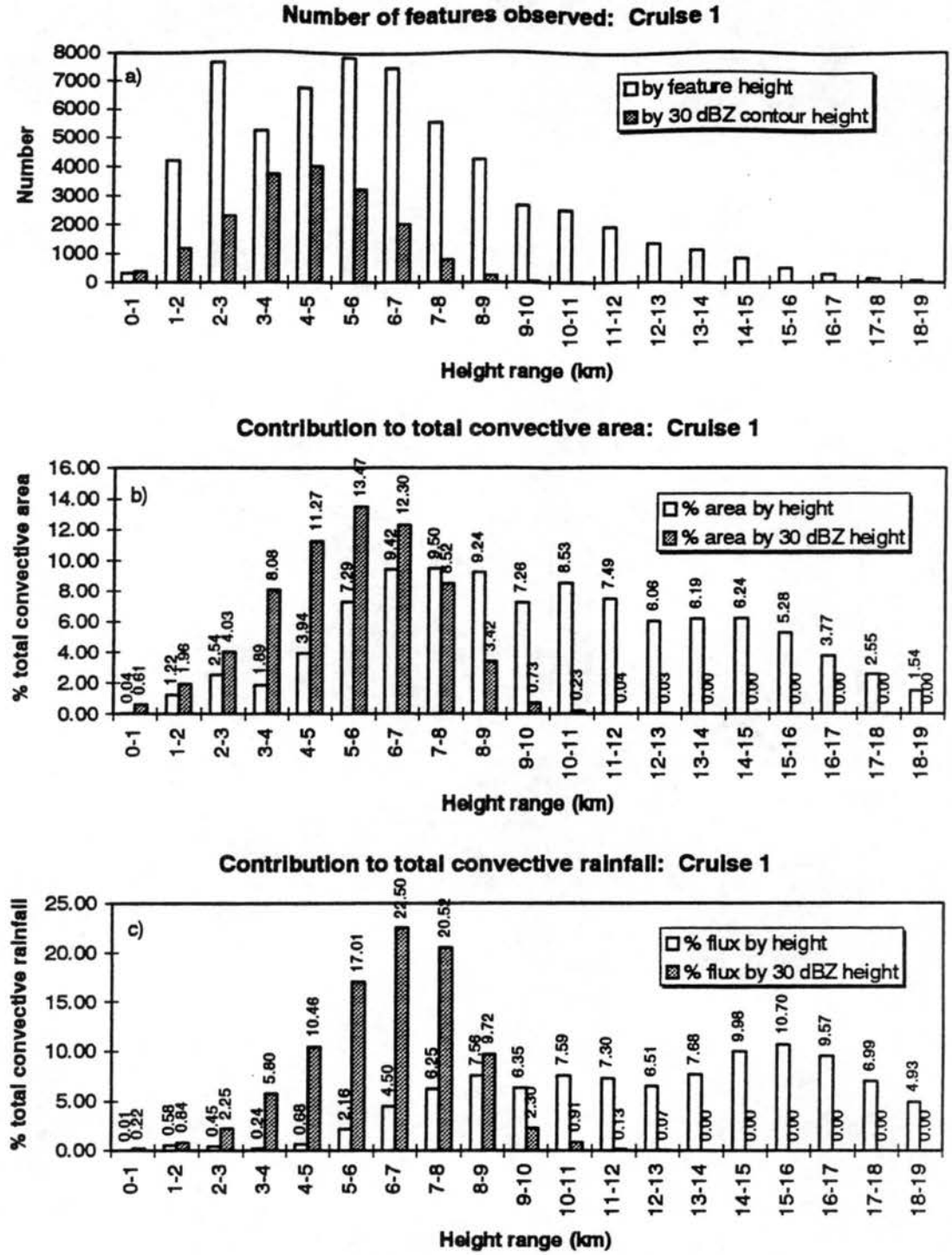

Fig. 3.5. Distribution of a) number count, b) percent of total convective area, and c) percent of total convective rainfall as a function of ***feature*** height (open bars) and 30 dBZ contour height (gray bars) during Cruise 1. Features with 30 dBZ contours (maximum reflectivity $\geq$ 30 dBZ) account for 30% of total features observed, 65% of convective area, and 93% of convective rainfall.

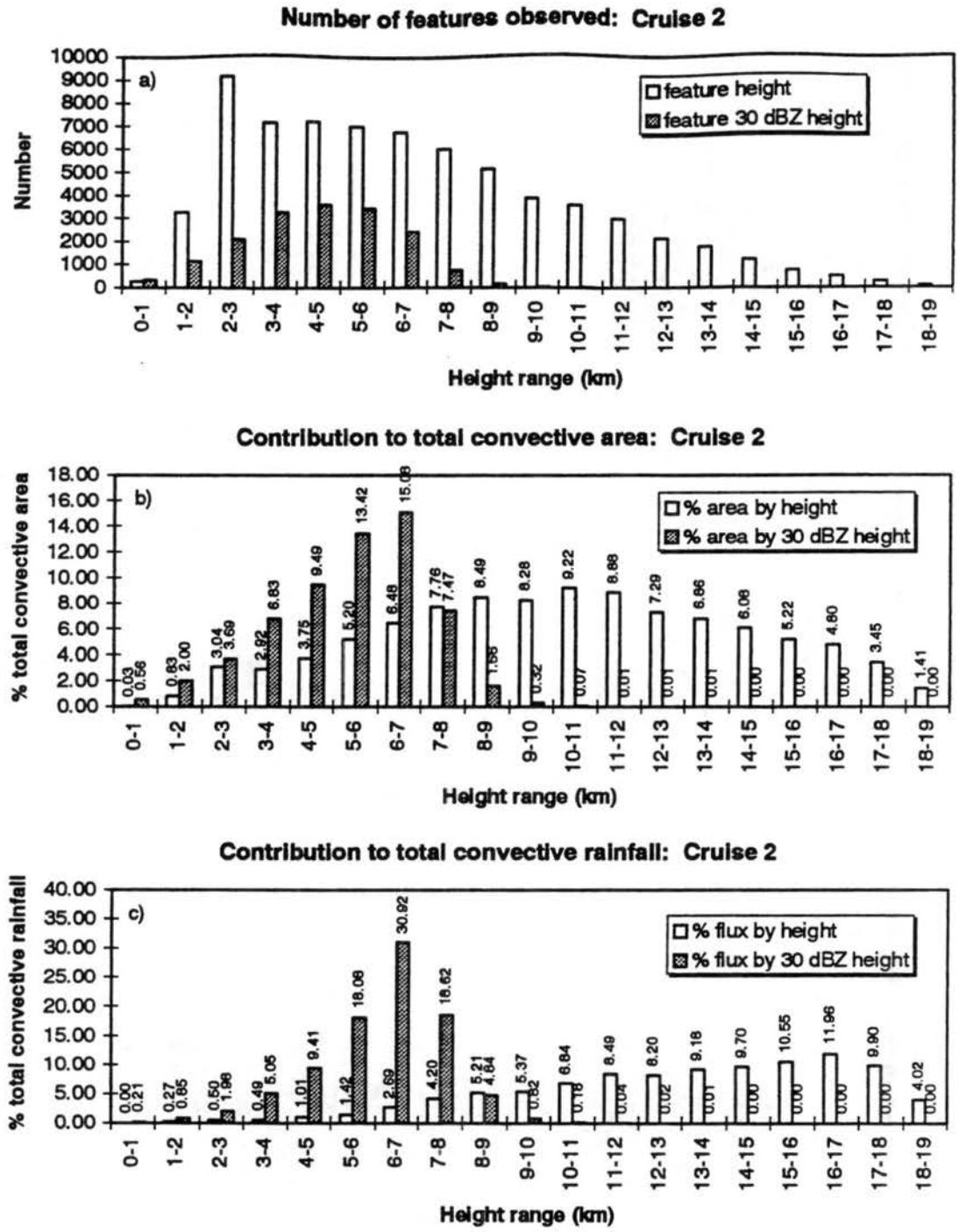

Fig. 3.6. As in Fig. 3.4, but for Cruise 2. Features with 30 dBZ contours (maximum reflectivity $\geq$ 30 dBZ) account for 25.1% of total observed features, 60.6% of convective area, and 91.0% of convective rainfall.

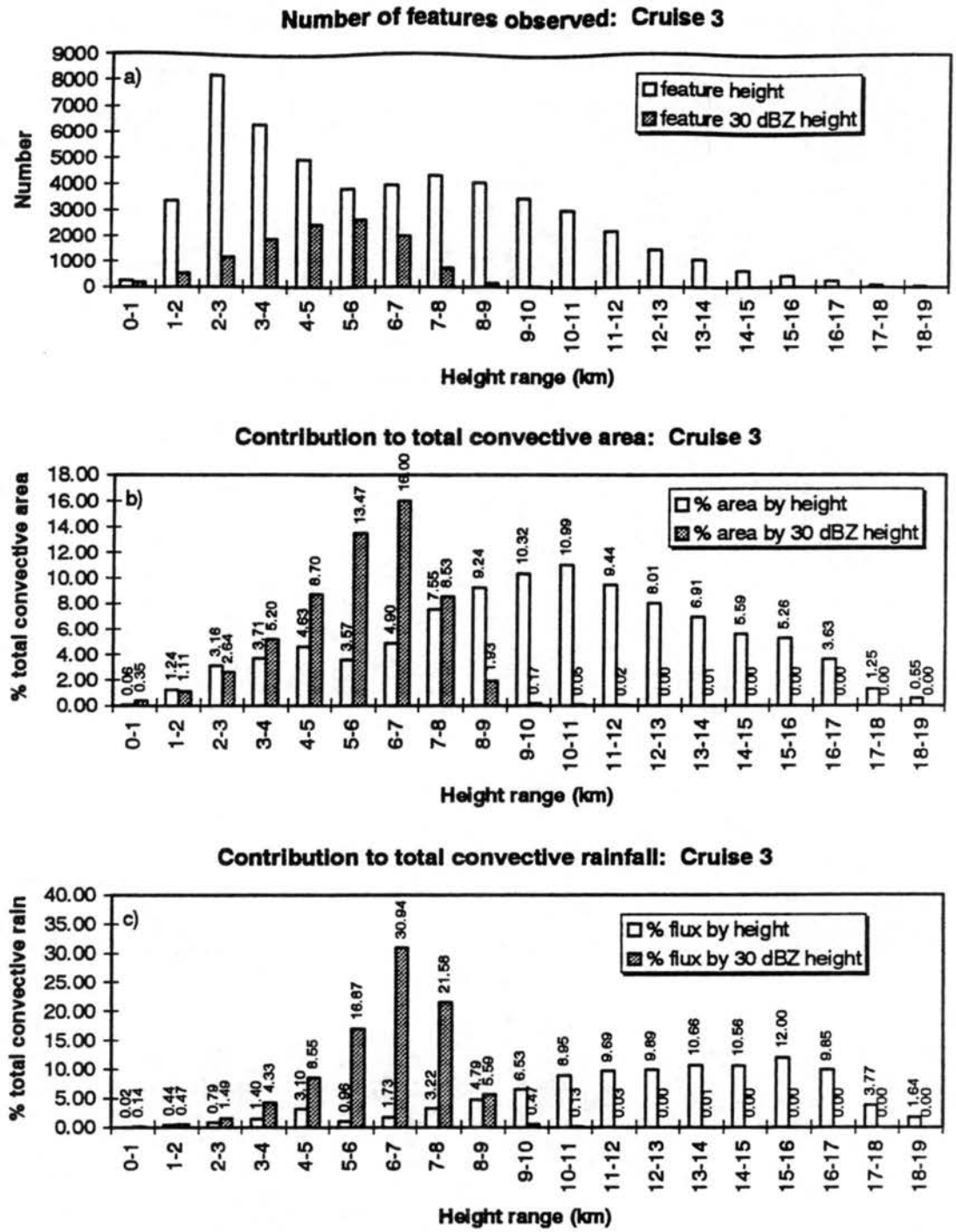

Fig. 3.7. As in Figure 3.4, but for Cruise 3. Features with 30 dBZ contours (maximum reflectivity $\geq$ 30 dBZ) account for 22.8% of total observed convective features, 58.2% of convective area, and 90.6% of convective rainfall.

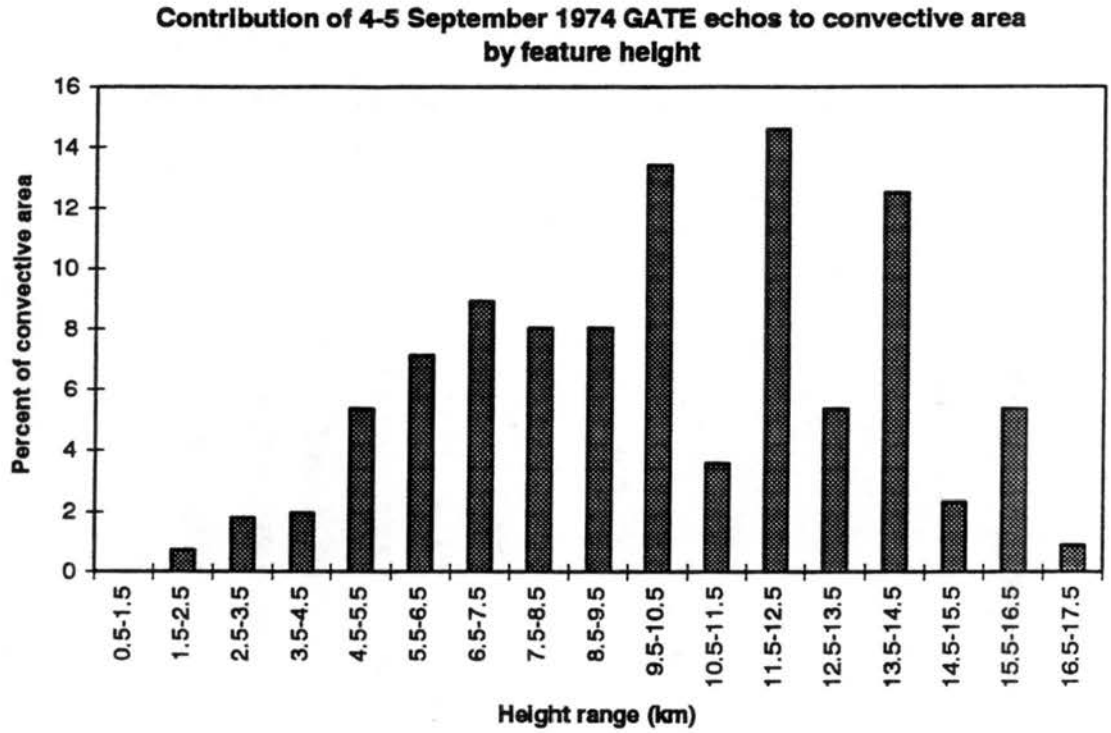

Fig. 3.8 Contribution to convective area by feature height for the 4-5 September 1974 GATE case (adapted from Leary, 1984).

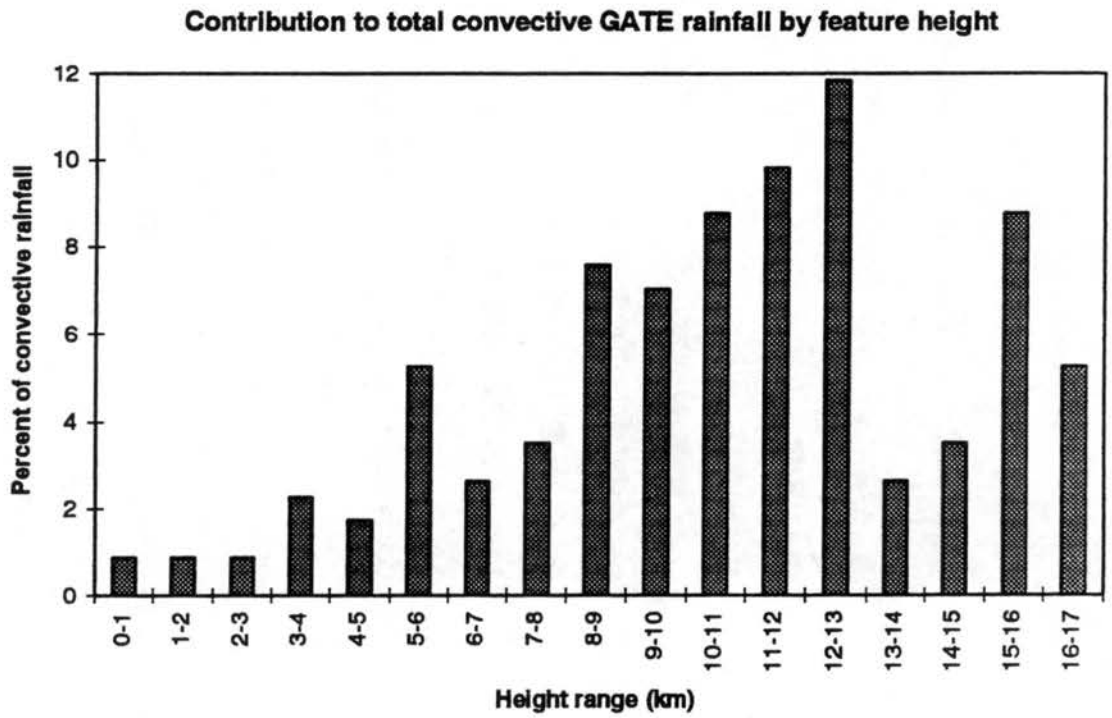

Fig. 3.9 Contribution to total convective rainfall for GATE features present at 00Z during each day of GATE. Height bins correspond to *maximum* height attained during echo lifetime (adapted from Cheng and Houze, 1979).

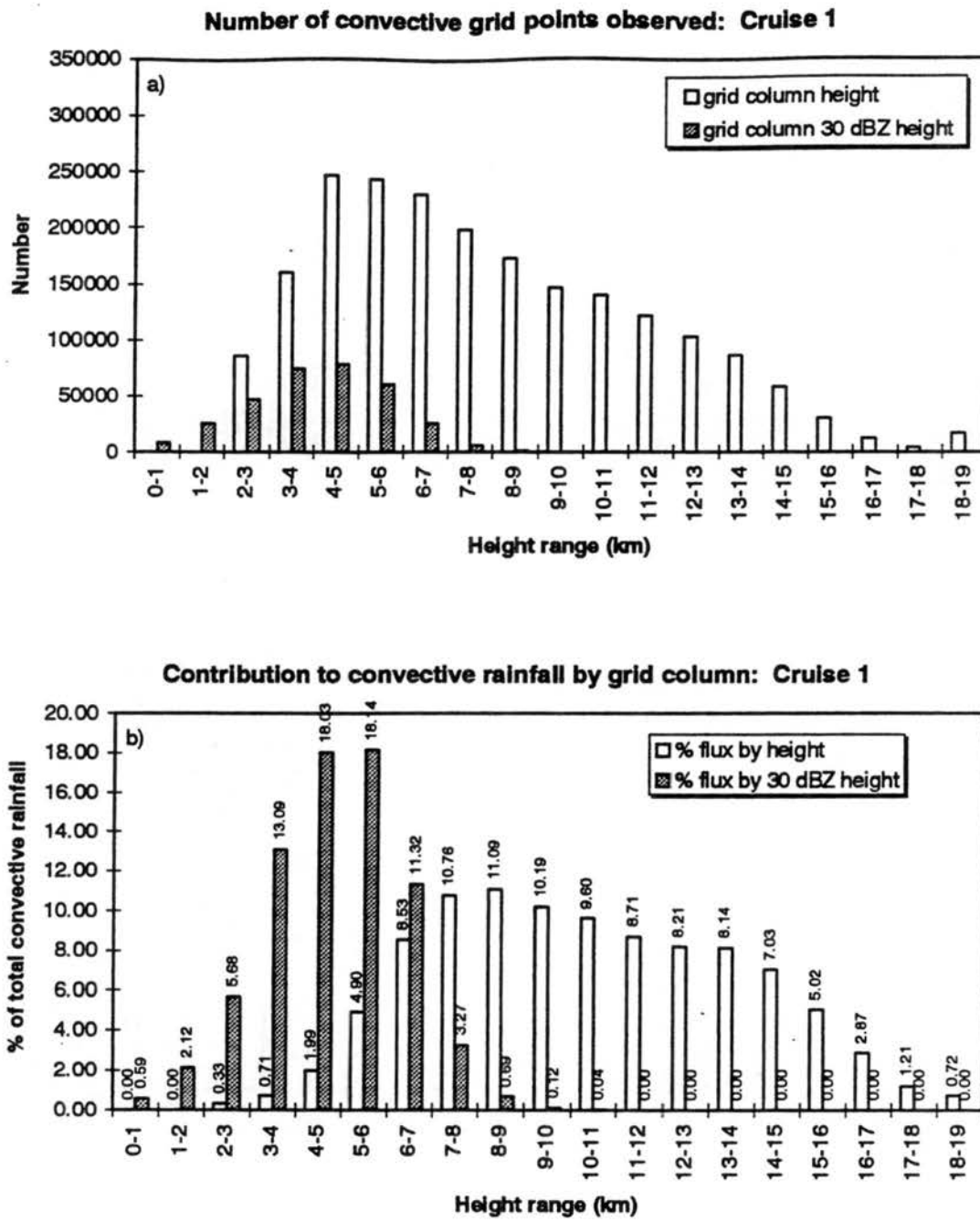

Fig. 3.10. Distribution of a) number count and b) percent of total convective rainfall as a function of *grid column* height (open bars) and 30 dBZ contour height (gray bars) during Cruise 1. Grid columns with 2 km reflectivity $\geq$ 30 dBZ account for 15.9% of total observed convective pixels and 73.1% of convective rainfall.

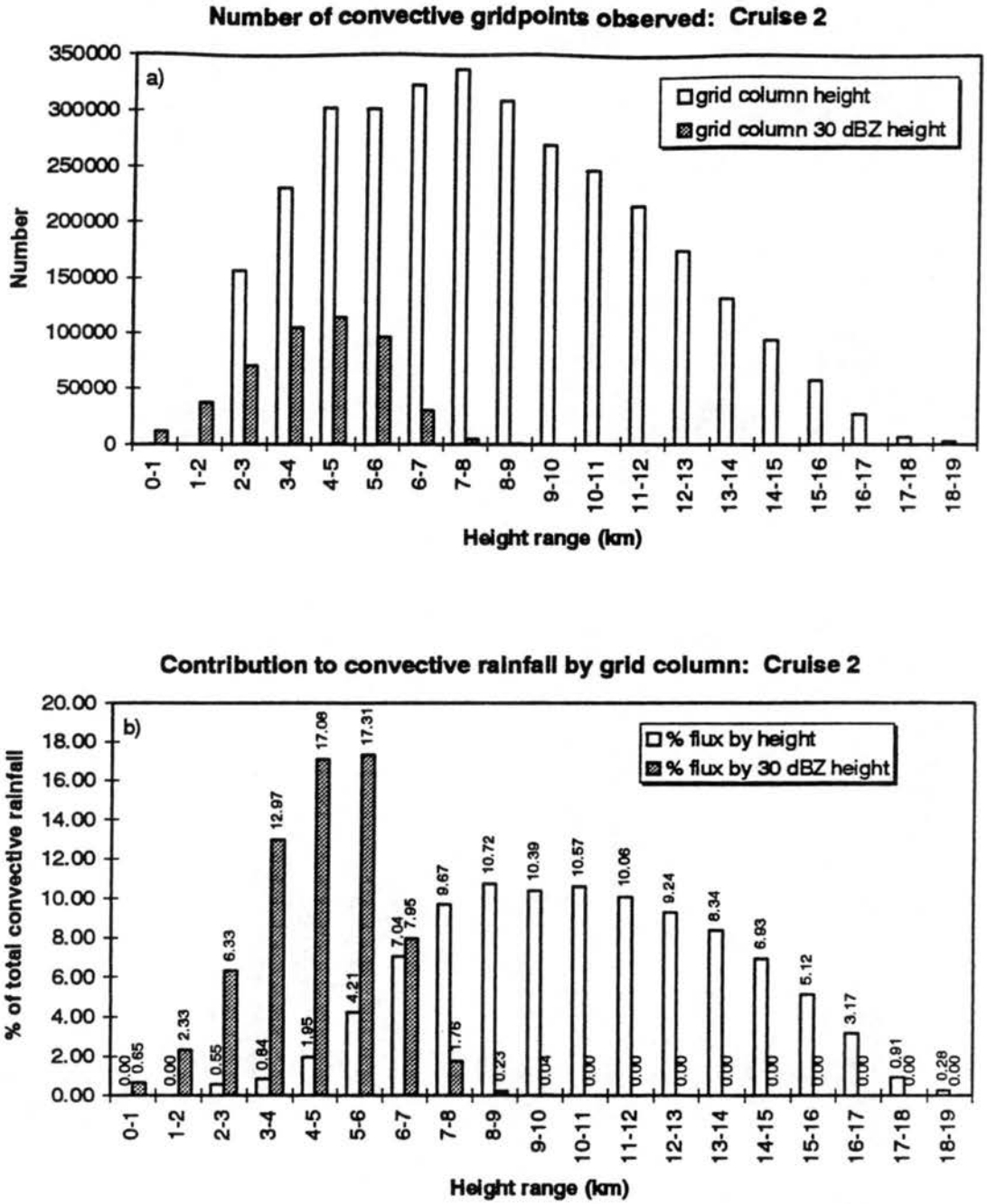

Fig. 3.11. As in Fig. 3.7, but for Cruise 2. Grid columns with 2 km reflectivity $\geq$ 30 dBZ account for 14.8% of total observed convective pixels and 66.7% of convective rainfall.

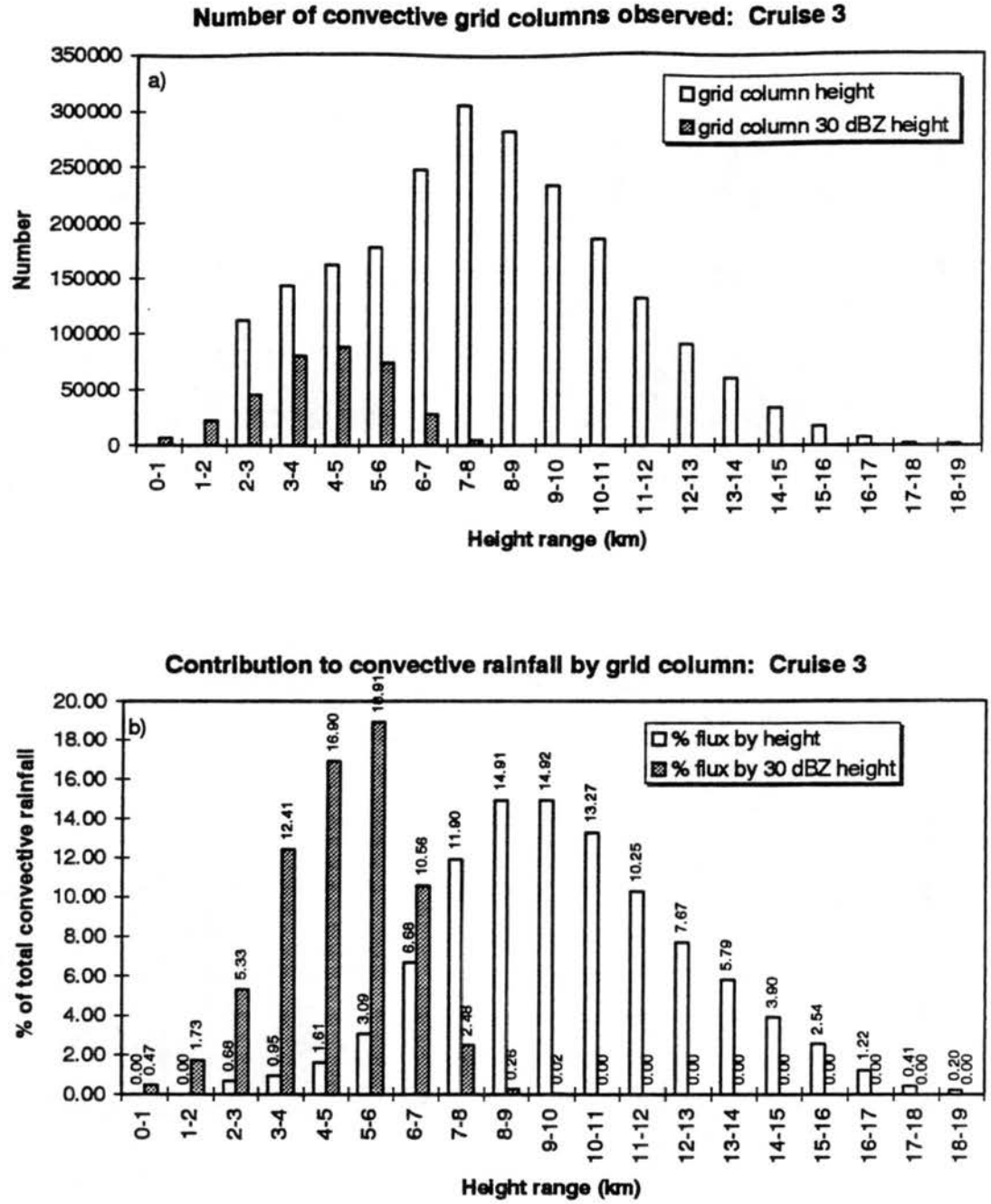

Fig. 3.12. As in Fig. 3.7, but for Cruise 3. Grid columns with 2 km reflectivity $\geq$ 30 dBZ account for 16.0% of total observed convective pixels and 69.1% of convective rainfall.

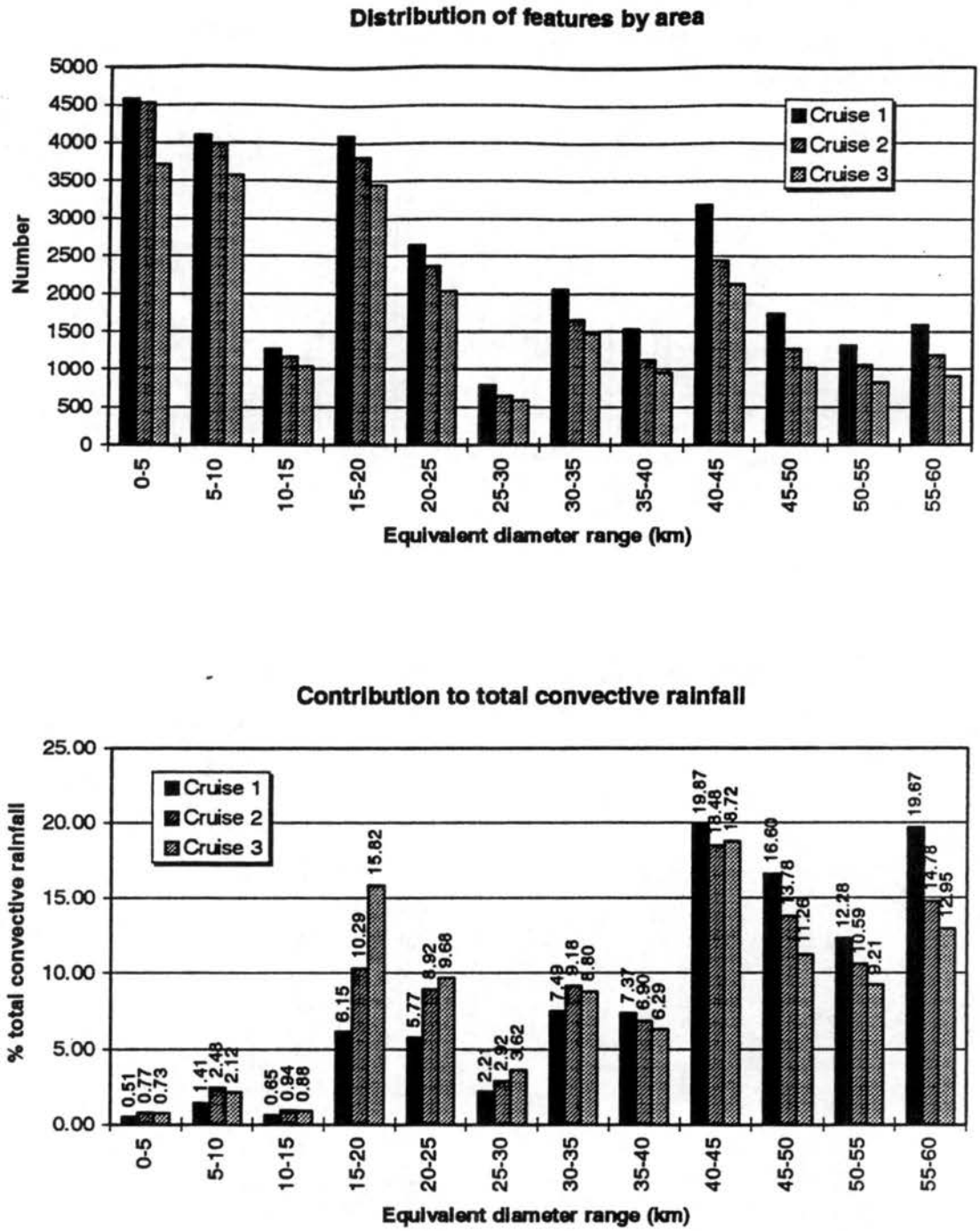

Fig. 3.13 Distribution of features as a function of area horizontal dimension (a) and distribution of convective rainfall as a function of horizontal dimension (b).

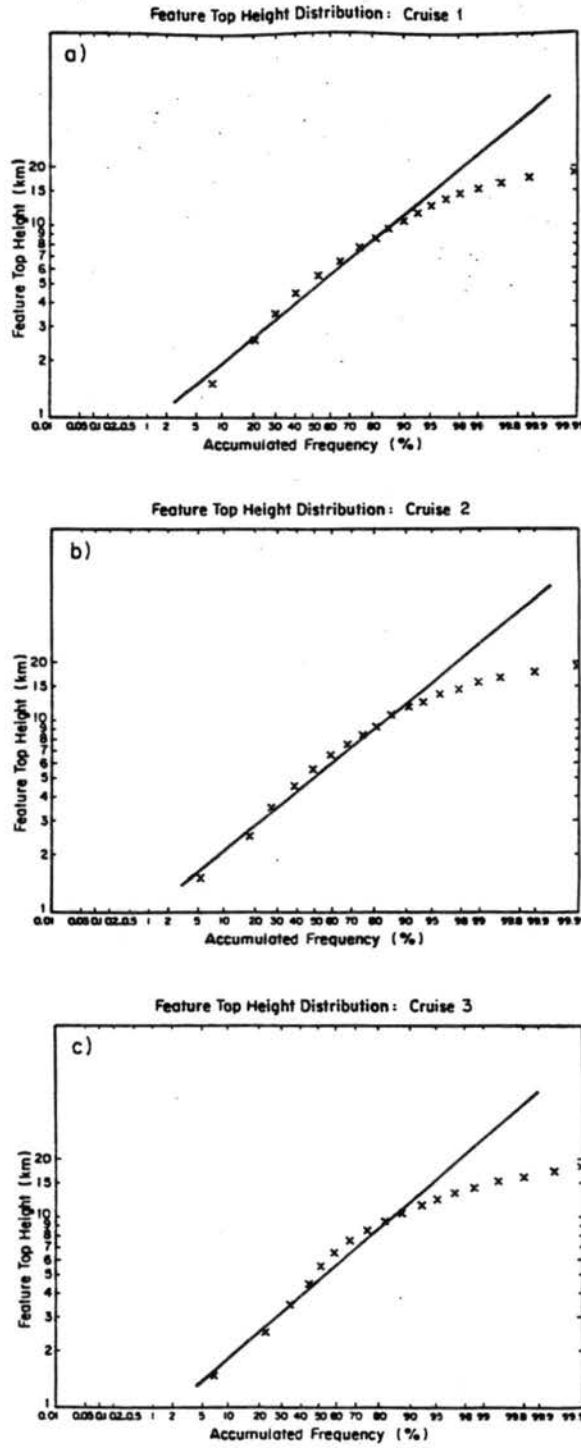

Fig. 3.14 Cumulative distribution of feature heights plotted on a probability scale for Cruises 1 through 3 (panels a-c, respectively). The feature height scale is logarithmic. Straight line are the cumulative probability curves for perfectly normal distributions having the same mean and standard deviation as the data.

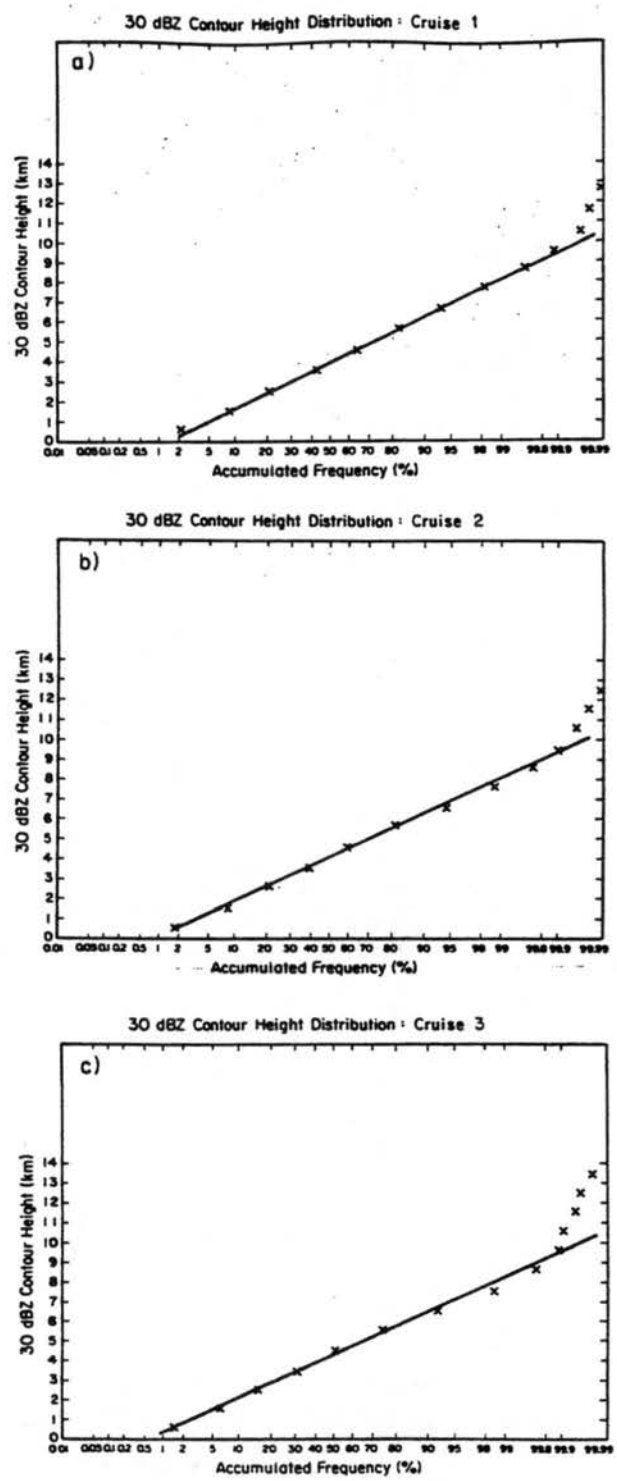

Fig. 3.15 As in Fig. 3.14, but for feature 30 dBZ contour heights.

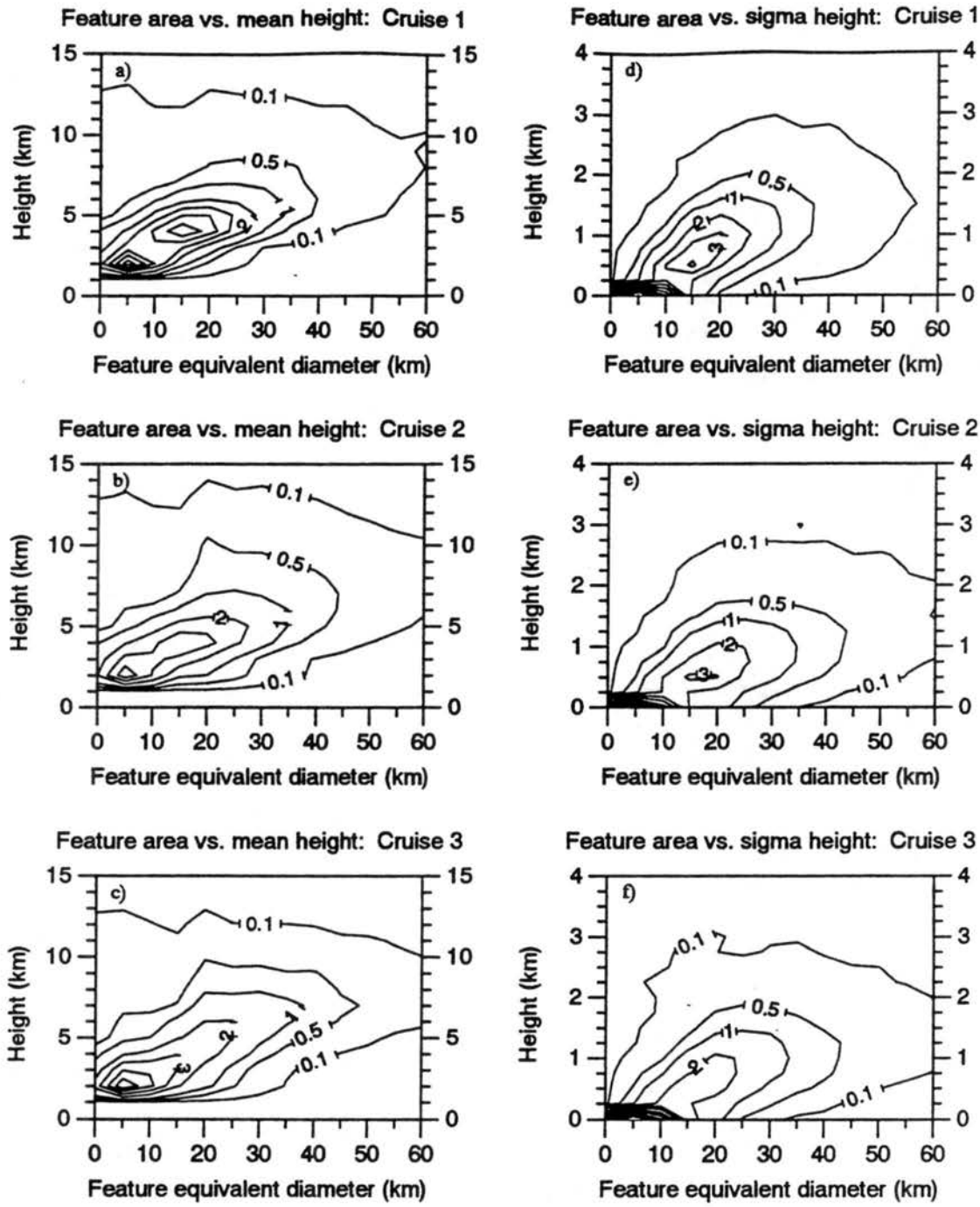

Fig. 3.16 Distribution of mean feature height (panels a-c) and the standard deviation of feature top height (within a single feature; panels d-f) as a function of feature horizontal dimension for each cruise.

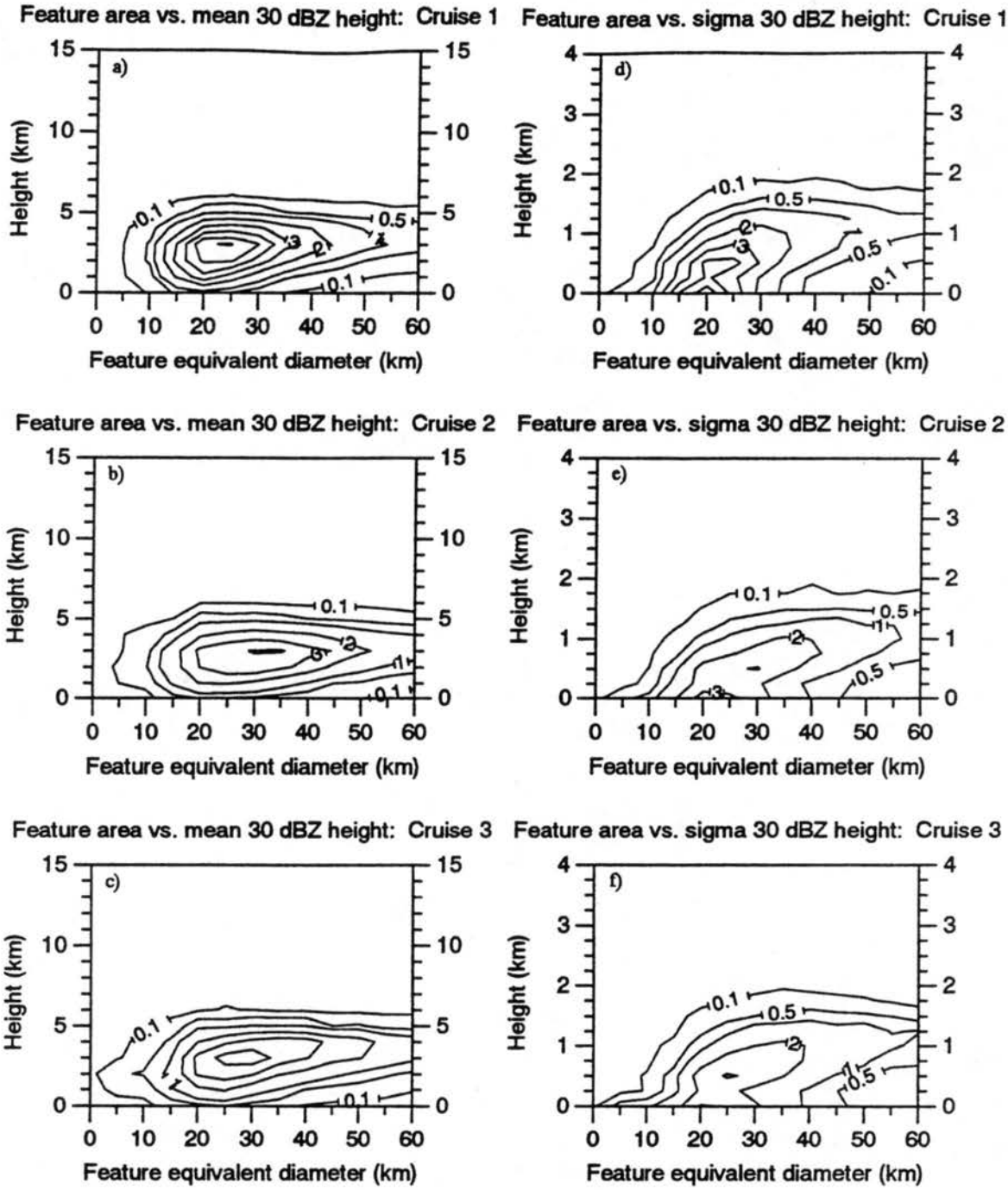

Fig. 3.17 As in Fig 3.16, but for 30 dBZ contour height.

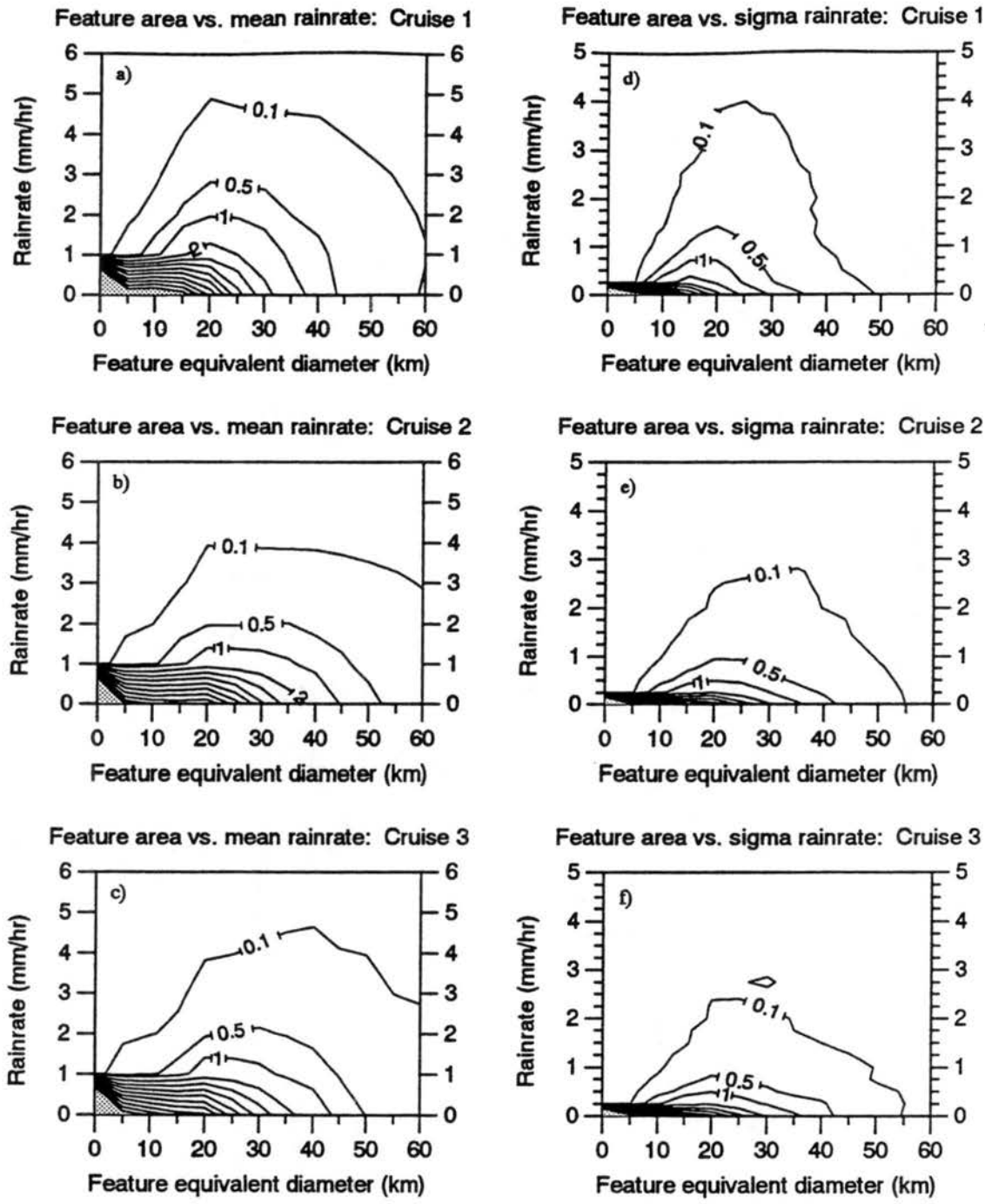

Fig. 3.18 As in Fig 3.16, but for rainfall rate.

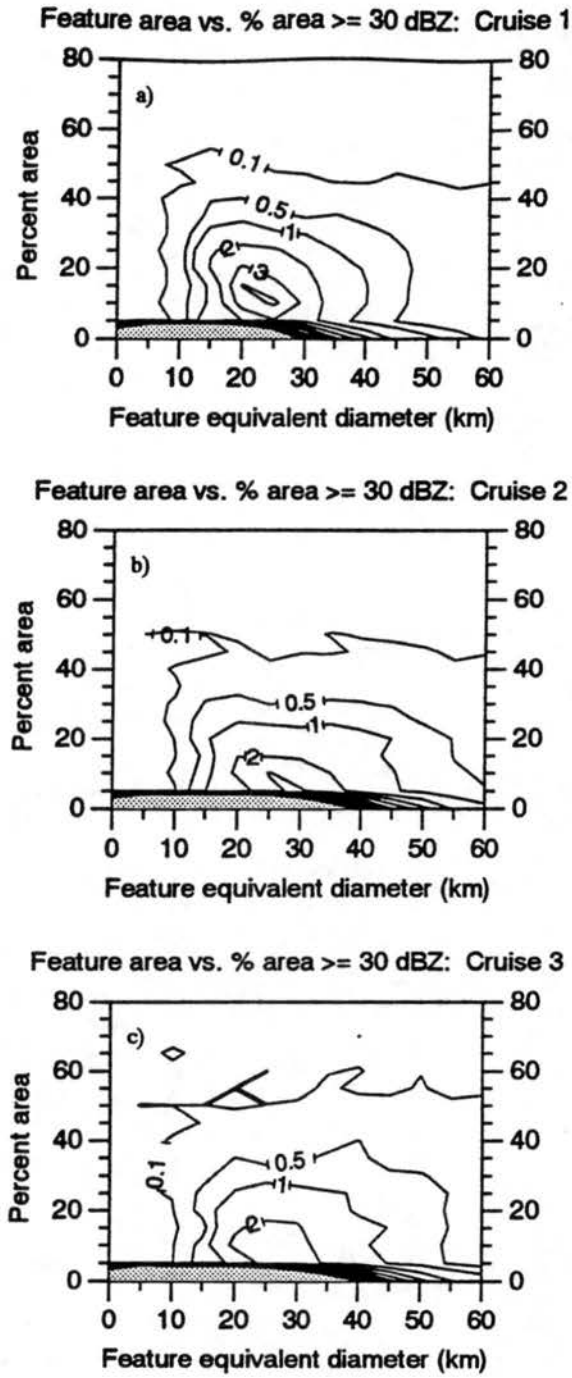

Fig. 3.19 Distribution of the fraction of feature area at z=2km with reflectivity $\geq$ 30 dBZ for cruises 1, 2, and 3 of the R/V Vickers (panels a-c, respectively).

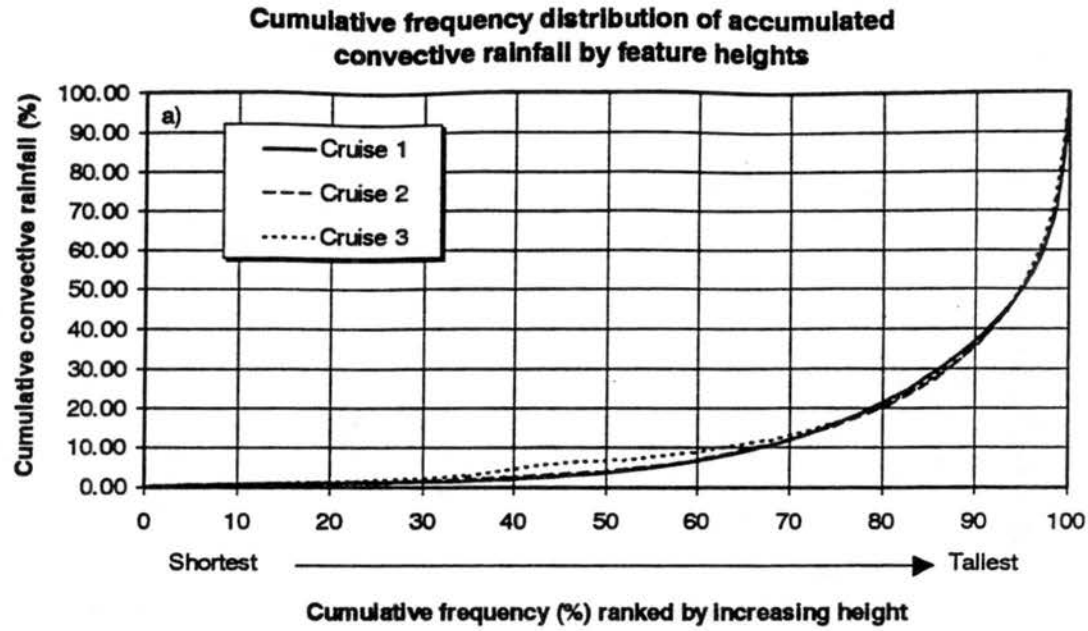

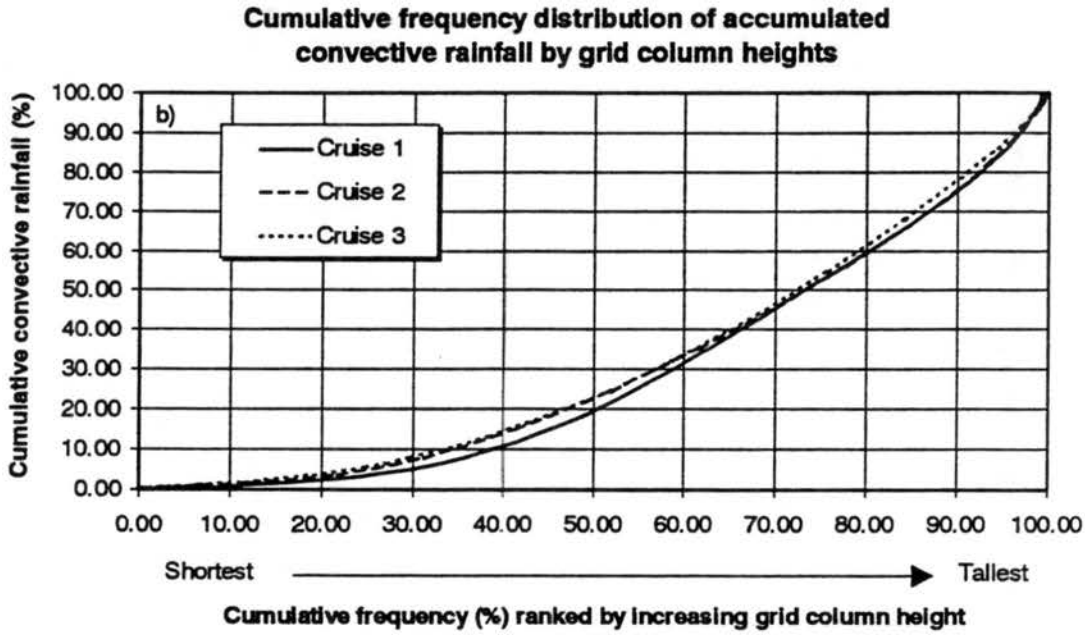

Fig. 3.20 Cumulative distribution of accumulated convective rainfall by a) feature height and b) grid column height.

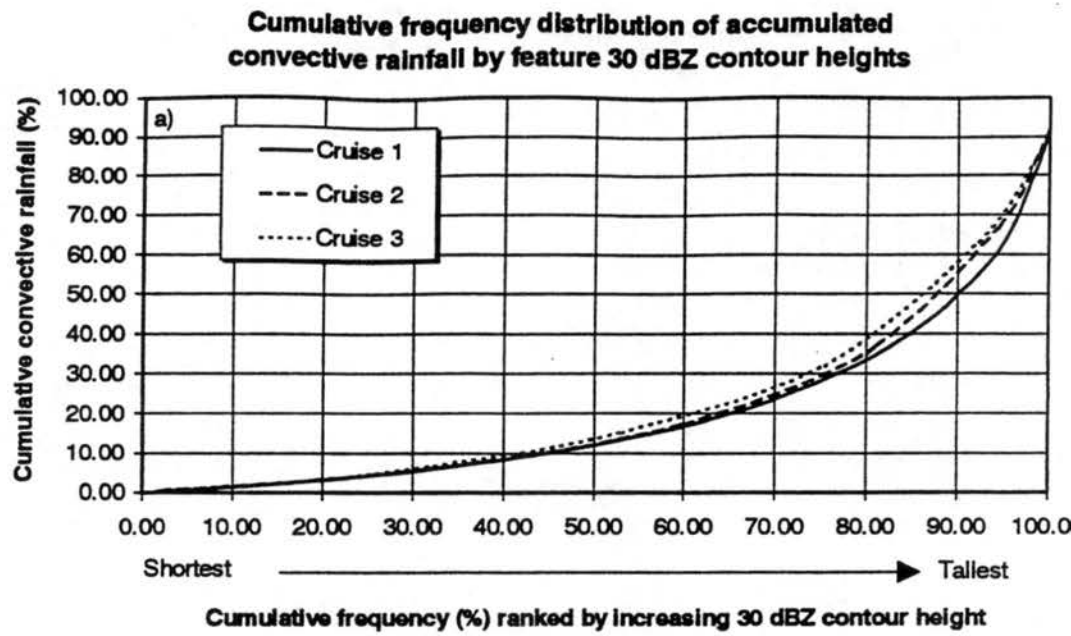

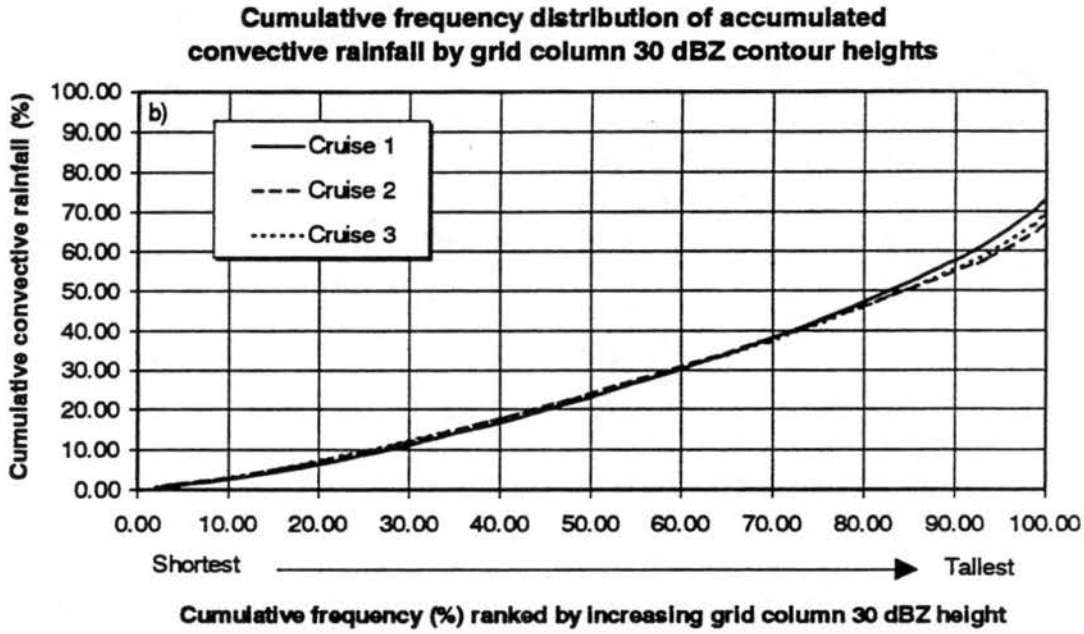

Fig. 3.21 Cumulative frequency distribution of accumulated convective rainfall by a) feature 30 dBZ contour height and b) grid column 30 dBZ contour height.

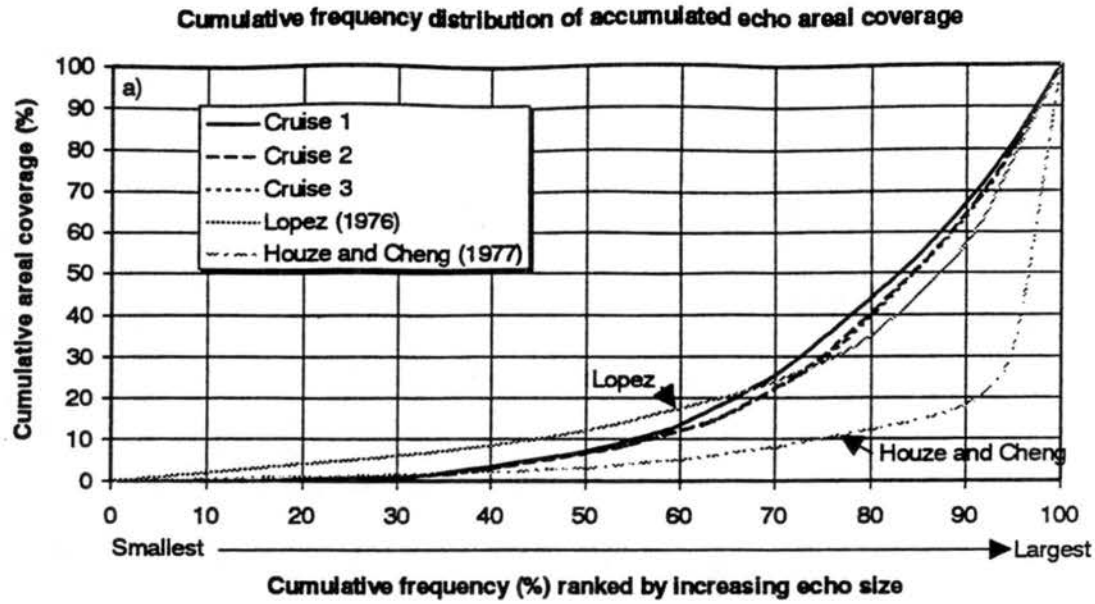

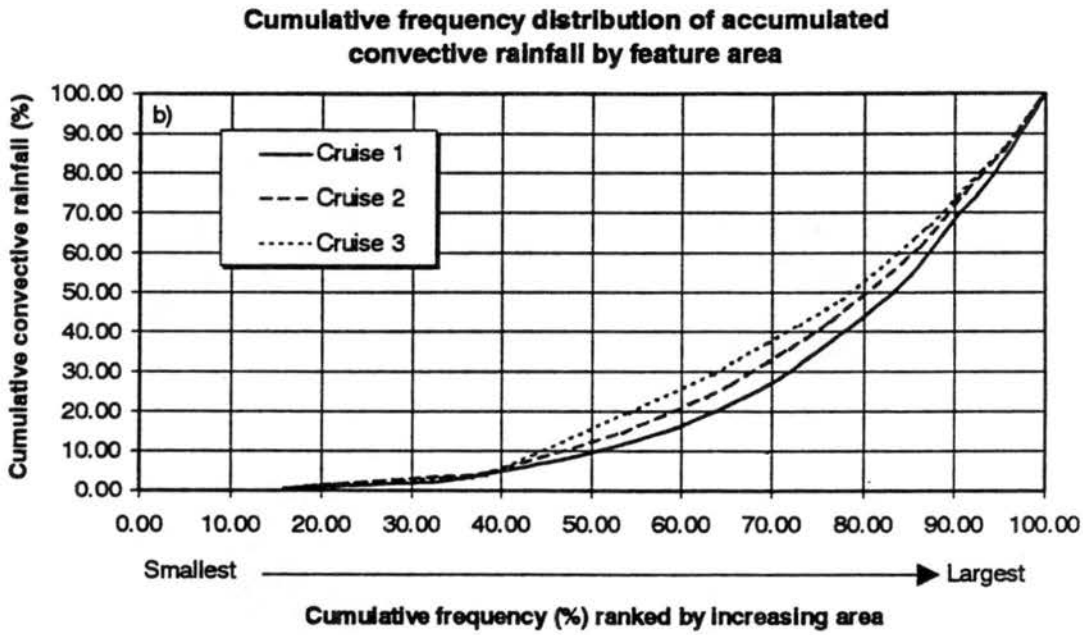

Fig. 3.22 Cumulative frequency distribution of accumulated echo areal coverage. Western tropical Atlantic distributions compiled by Lopez (1976) and Eastern Atlantic distributions compiled by Houze and Cheng (1977) are shown for comparison.

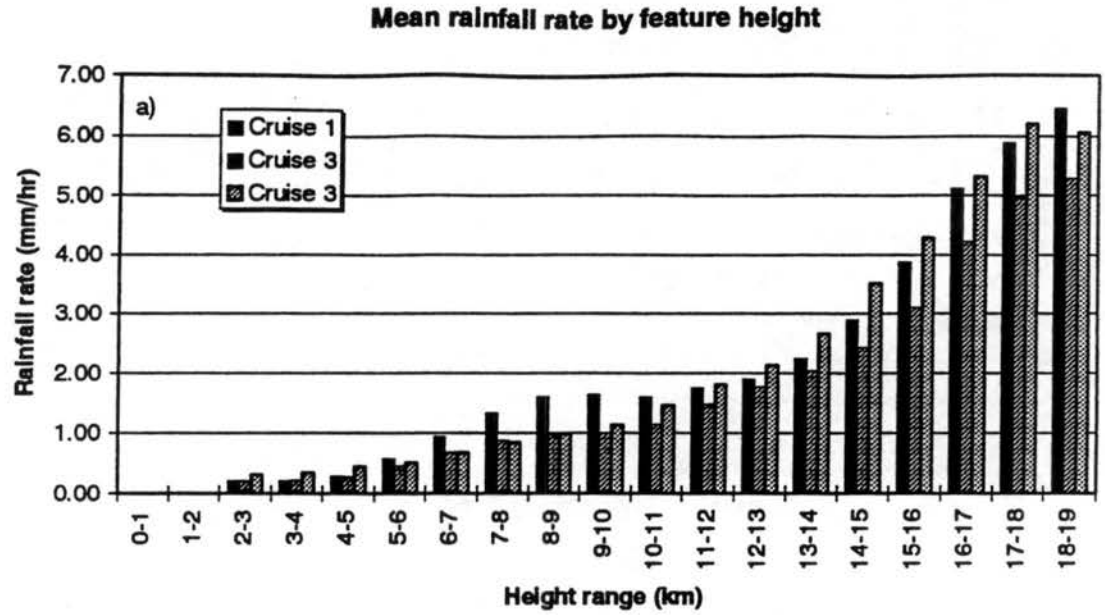

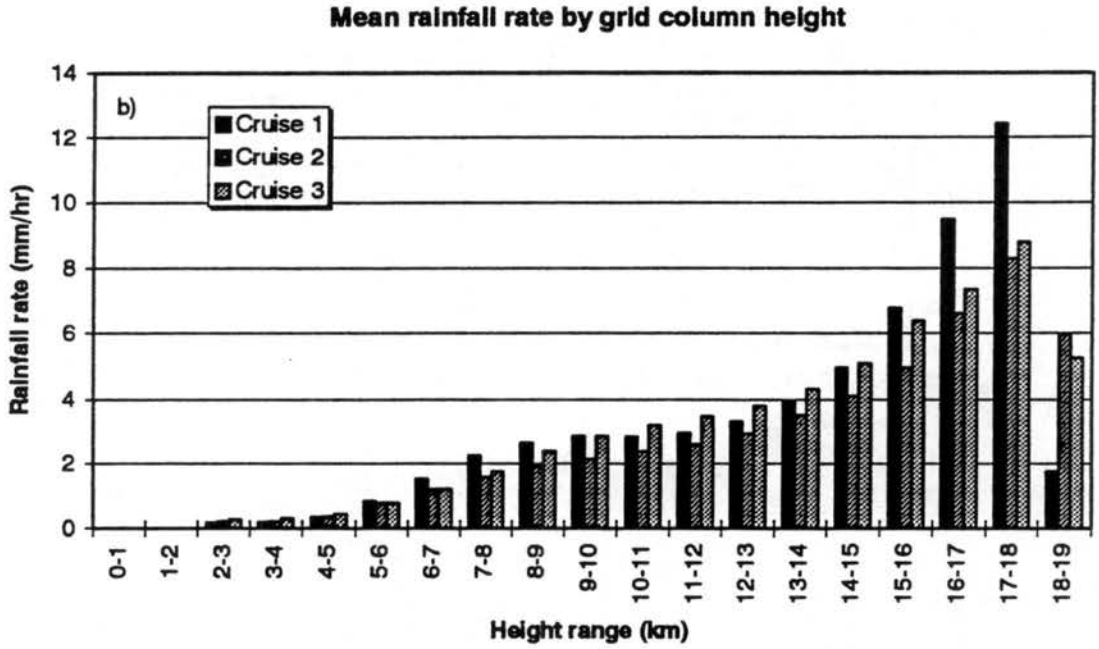

Fig. 3.23 Mean rainfall rates for a) convective feature height categories and b) convective grid column height categories for each cruise of the R/V Vickers. Note the difference in scale for rainfall rate in each panel.

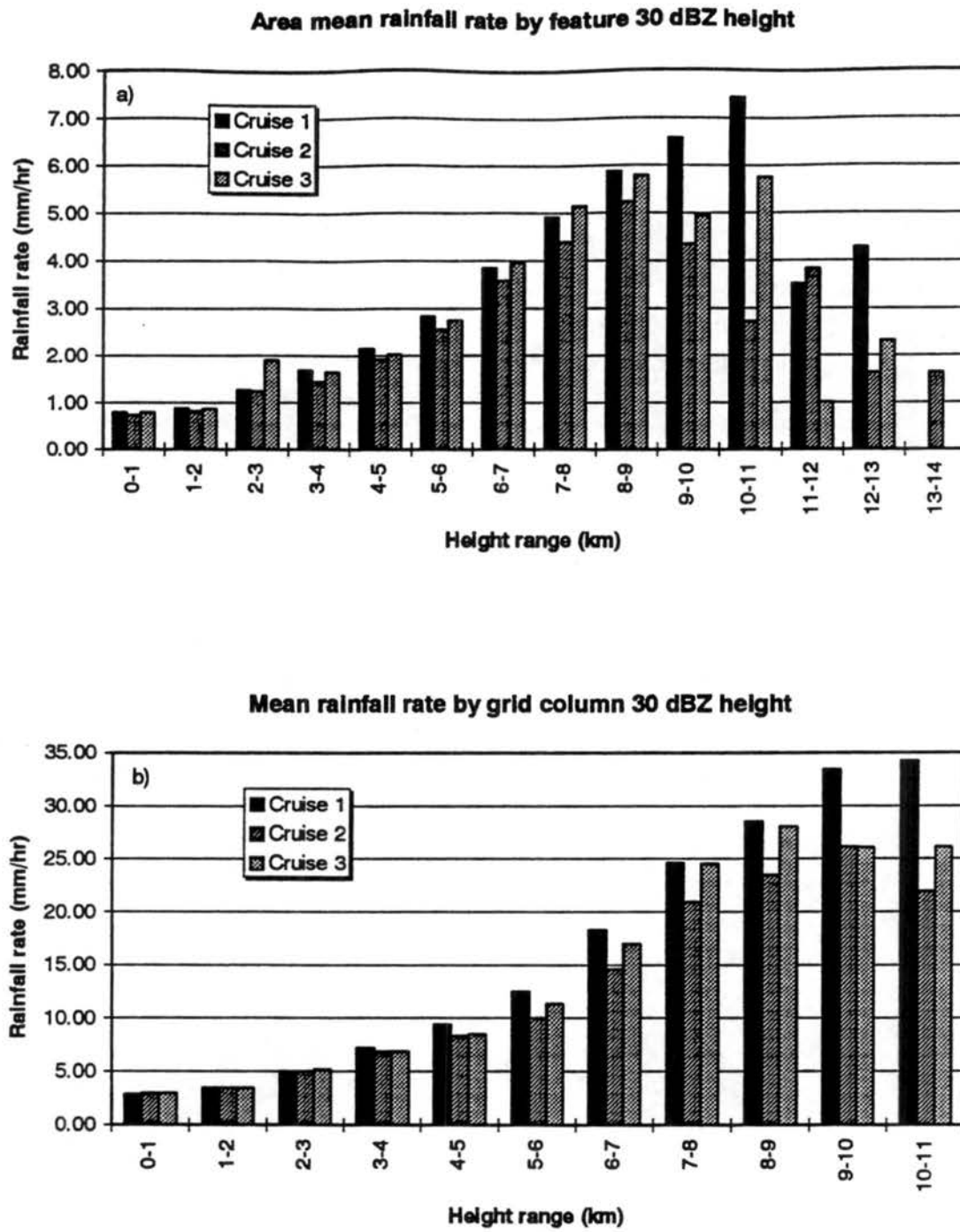

Fig. 3.24 Mean rainfall rates for a) convective feature 30 dBZ contour heights and b) convective grid column 30 dBZ contour heights. Note the difference in scale for rainfall rate in each panel.

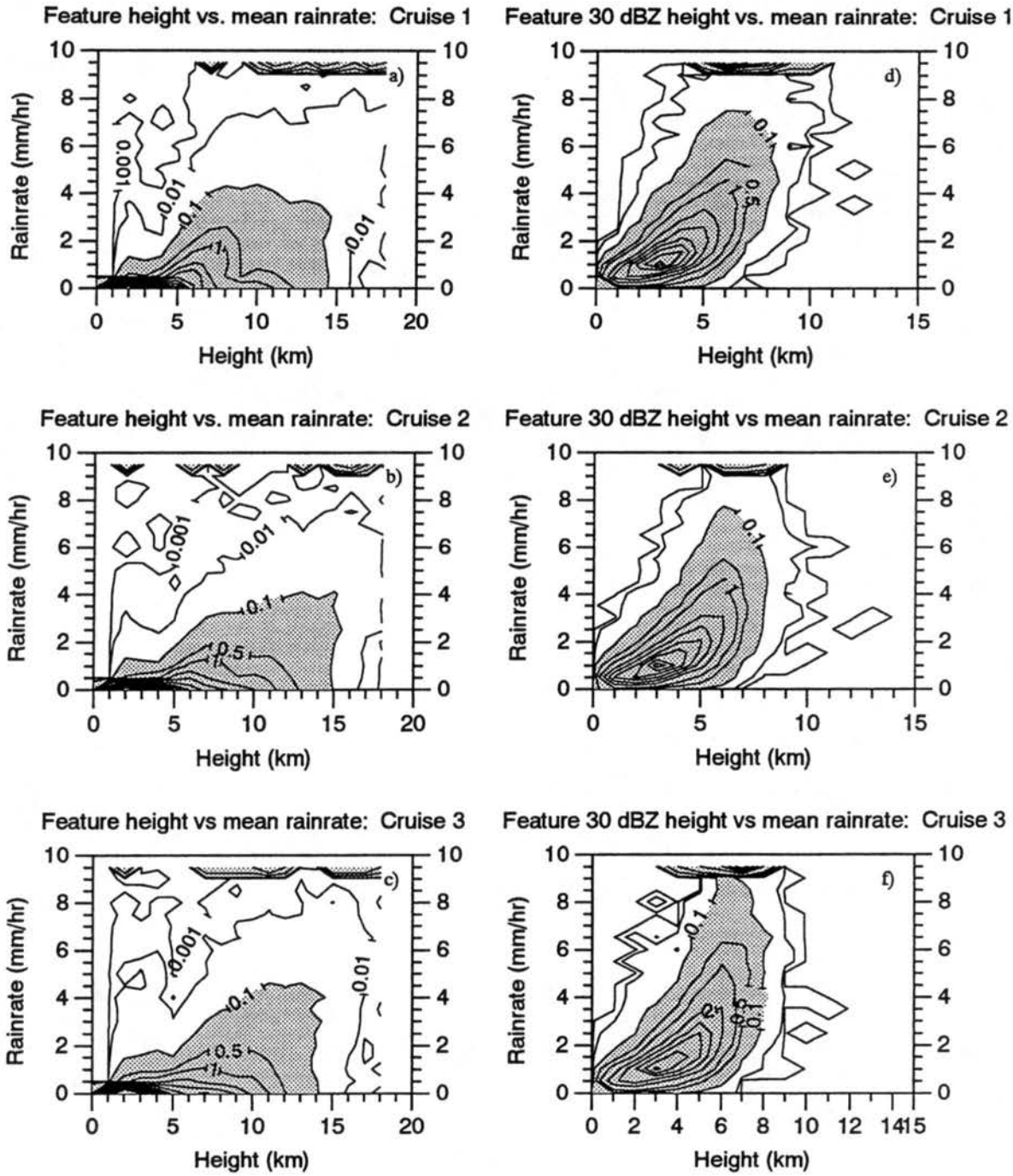

Fig. 3.25 Distribution of feature mean rainfall rate as a function of feature height (panels a-c) and 30 dBZ contour height (panels d-f). Percentages greater than 0.1% are shaded.

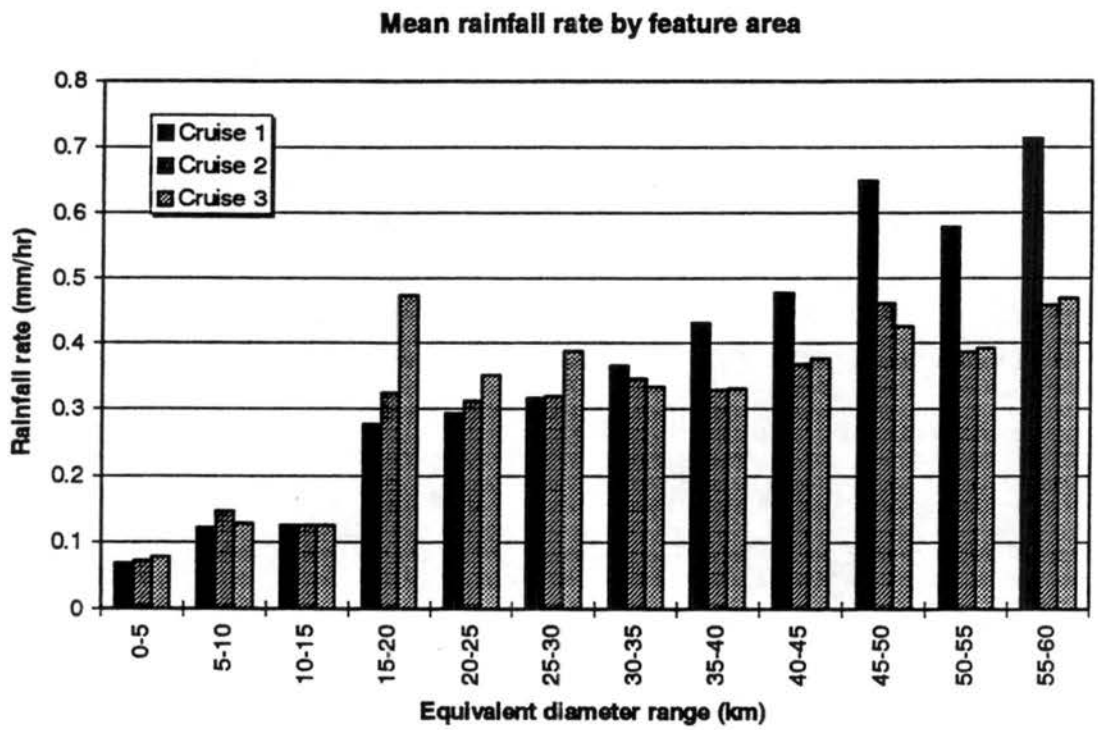

Fig. 3.26 Mean rainfall rate as a function of feature area.

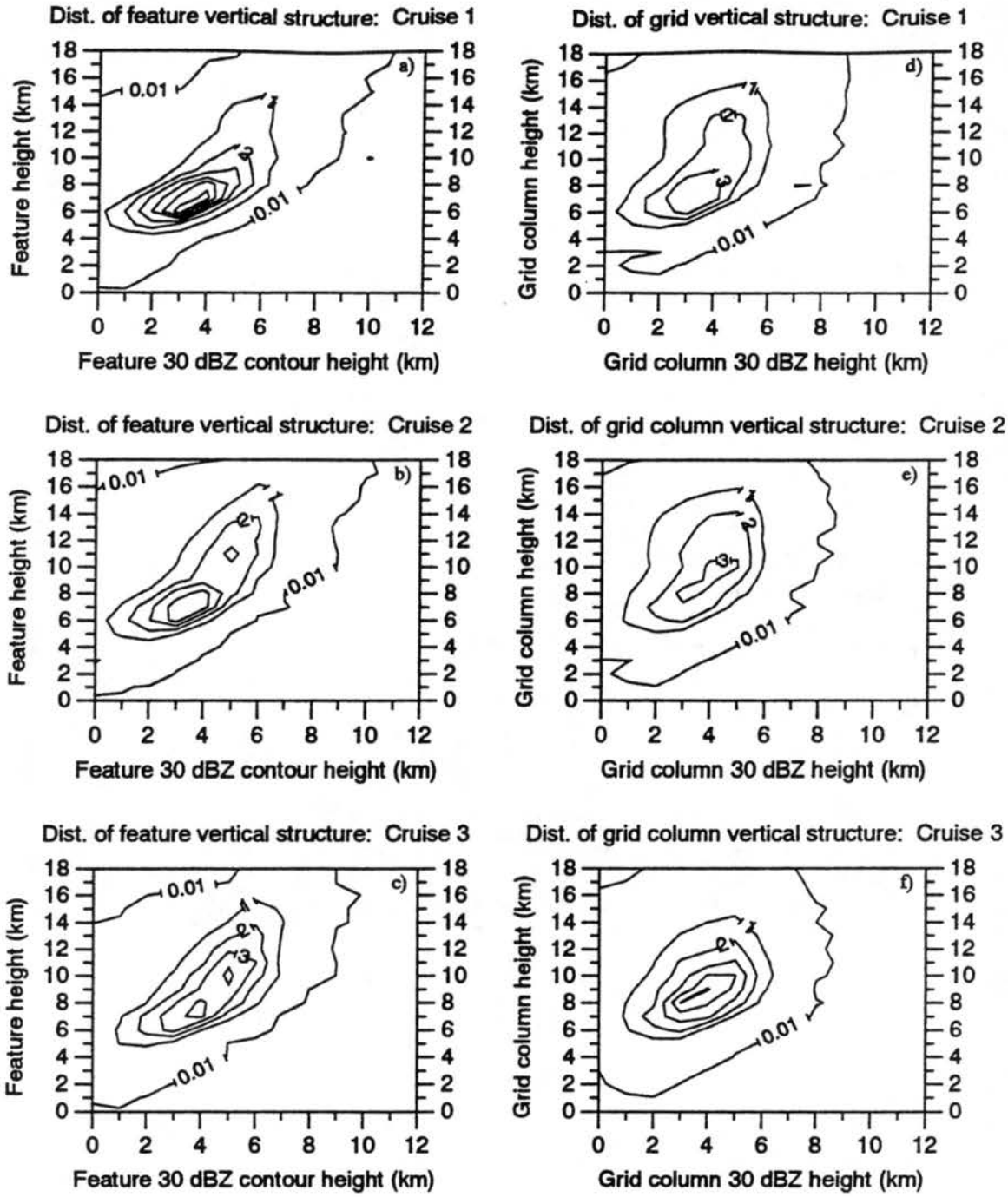

Fig. 3.27 Distribution of convective features (panels a-c) and grid columns (panels d-f) as a function of height and 30 dBZ contour height for each cruise.

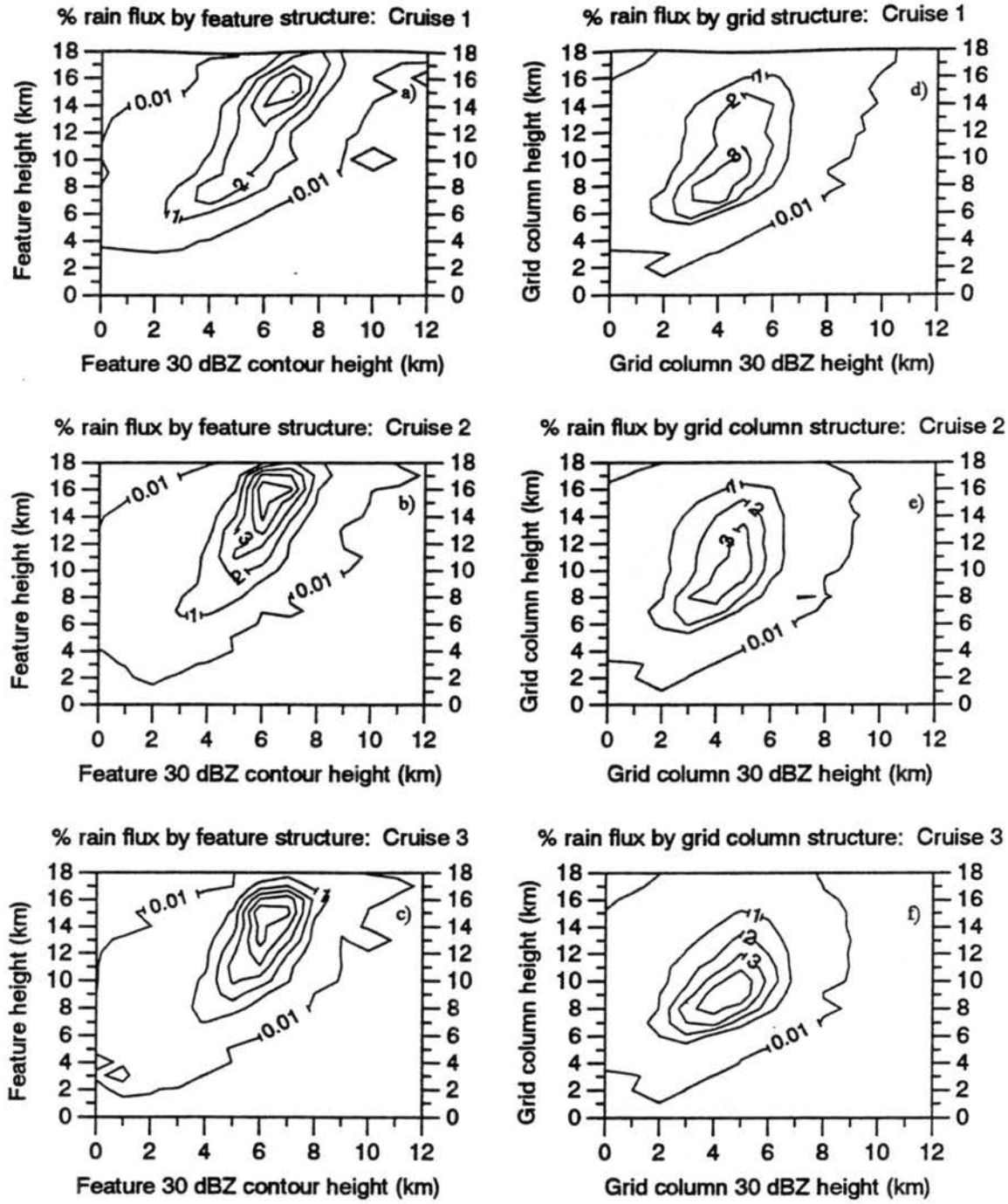

Fig. 3.28 As in Fig. 3.27, but for contribution to total convective rainfall.

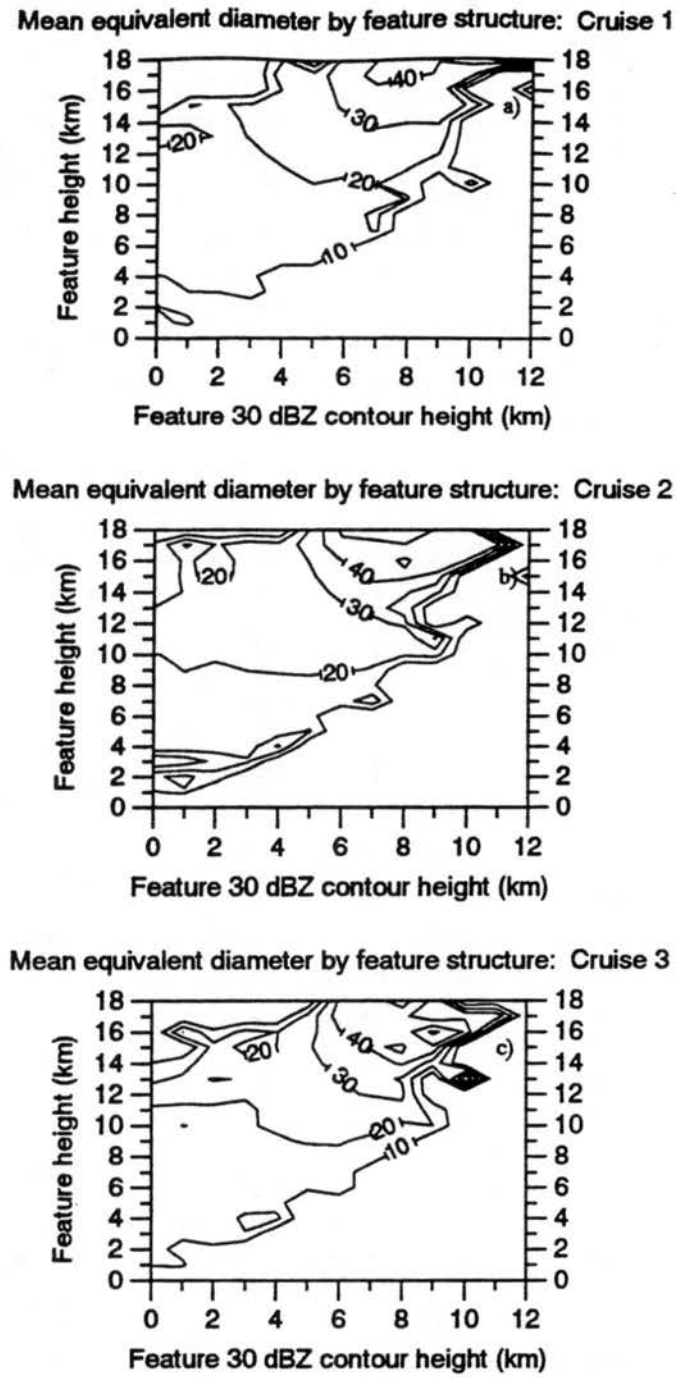

Fig. 3.29 Mean equivalent diameter (km) of features associated with various vertical structures.

Chapter 4

VARIABILITY AND MODULATION OF CONVECTION DURING COARE

Chapter 3 focused on mean distributions of convection over month long periods, which is useful for climatological studies and has particular relevance for TRMM, which will map tropical rainfall amounts over monthly time scales. In this chapter, variations in convective activity and particularly the vertical structure of convection are studied over shorter time periods in an effort to determine how variations in the large-scale environment affect—and are affected by—the vertical structure of convection. Such studies are useful to applications such as global climate models, which predict atmospheric conditions on spatial scales comparable to the IFA, but cannot resolve individual precipitating systems. The first section of this chapter examines the relationship of radar-derived rainfall to variables calculated using the interpolated sounding data. Section 2 examines how the daily distribution of convective features (and grid columns) varies with time and investigates what factors modulate these variations. Section 3 presents a method for computing time series of convective heating profiles and examines the relationship between heating profile shape and convective vertical structure.

4.1 Relationship between rainfall and environmental variables

Before discussing the relationship of radar-derived rainfall and environmental variables, it is first necessary to clarify what is meant by "environmental variables" and the "large-scale environment." In theory, one would like to separate the effects of precipitating systems and pre-existing environmental conditions in any study attempting to ascribe behaviors of these systems to the state of the atmosphere. When attempting to model specific convective events, this desired separation is usually possible if a sounding can be identified that is representative of the unmodified system environment (usually one that is

launched just ahead of a main convective line) and if that sounding produces a reasonably behaved simulation.

The difference between "system" and "environment", however, becomes less distinct when utilizing the interpolated sounding dataset. The interpolated sounding at each 1×1 degree latitude-longitude grid point is a distance-weighted mean of the nearest six soundings. As such, some or all of the six soundings may have been launched "ahead" of convective systems; or they may have been launched within systems, or perhaps in air that was recently modified by the passage of a system. Therefore, the interpolated sounding at any given grid point should be thought of as being representative of mean atmospheric conditions in the vicinity of that gridpoint (soundings launched within the IFA had horizontal separations of approximately 300 km). In this study, then, "environmental conditions" and "large-scale conditions" refer to the mean state of the tropical environment as a whole—unmodified air representative of the undisturbed environment as well as air modified by precipitating systems.

4.1.1 Rainfall and convective available potential energy (CAPE)

Convective available potential energy, or CAPE, is a measure of the maximum possible vertical velocity that could be attained by an undilute parcel rising from the level of free convection (LFC) to its level of neutral buoyancy (LNB). Mathematically, CAPE is defined as

$$CAPE = \frac{w_{max}^2}{2} = \int_{LFC}^{LNB} \left(\frac{T_{v,parcel} - T_{env}}{T_{env}} \right) dz . \qquad (4.1)$$

It is common practice to compute the lifted parcel properties by averaging the temperature and specific humidity of the mixed layer—typically lowest 50 mb during COARE. However, the interpolated sounding data set only extends down to the 1000 mb level, whereas surface pressures in the warm pool region are typically near 1010 mb. Parcel properties were therefore computed as the mean temperature and specific humidity in the 1000 to 960 mb level. The virtual temperature of the parcel[1] is computed in order to estimate the true buoyancy of the lifted parcel.

[1] The virtual temperature is the temperature of a parcel containing no water vapor, but having the same density as the moist parcel at the same pressure.

Since a more unstable atmosphere should lead to greater potential updraft velocities, and therefore enhanced rainfall production, it is expected that rainfall production and CAPE should be somehow related. Fig. 4.1 presents time series of MIT radar-derived rainfall and sounding-derived CAPE values during the four month IOP. A 3-day running mean filter has been applied to emphasize the trends in each curve. CAPE tends to increase during periods of light rainfall, since decreased cloud cover allows the ocean surface to heat up, which results in higher boundary layer temperatures and water vapor mixing ratios. CAPE tends to decrease during rain events, as the instability is consumed by rainfall production. In general, however, the two curves do not appear to be particularly well-correlated. One explanation for this apparent lack of correlation may be that rainfall production lags CAPE generation. In other words, CAPE increases over a certain period before the boundary layer energy is tapped by convection.

To investigate this possibility, lag correlations of rainfall and CAPE are computed up to 10 days prior to and 10 days after rainfall events. The lag correlation results are presented in Fig. 4.2 In this figure, negative lag corresponds to CAPE leading rainfall, while positive lag corresponds to rainfall leading CAPE. For all lag periods, the correlations are rather low, although at times they are statistically significant at the 95% confidence level (indicated by dashed lines). From this analysis, it is seen that maximum (minimum) CAPE values precede maximum (minimum) rainfall amounts by approximately 3 days, although the low correlation (0.2) indicates that factors other than CAPE also control the timing of rainfall occurrence. On average, CAPE decreases for four days following rainy periods, although CAPE may respond faster on specific occasions, as can be seen in Fig. 4.1.

Ushiyama *et al.* (1995) performed a similar analysis for rainfall observed in an oceanic sector by the X-band radar operating at Manus Island from November 1992 to Jan 1993. CAPE values were computed from the omegasonde that was launched from the same site as the radar. Lag correlations between rainfall observed in an "ocean sector" and CAPE reveal a similar pattern to those observed in Fig. 4.2, with peak positive correlation at lag -1 to -2 and a rapid decrease in correlation a few days following a rainfall event. Magnitudes of the correlations are essentially the same. The 1-to-2 day lag observed during COARE appears to be similar to that for the GATE region, as suggested by the analysis

of Thompson *et al.* (1979) who found that, for 3–5-day easterly wave disturbances, CAPE lead rainfall by approximately a quarter wavelength, which corresponds to slightly more than 1 day.

The primary difference between the correlations in Fig. 4.2 and those presented in Ushiyama *et al.* is the 4-5 day periodicity of correlation for the Manus data (i.e., peak positive correlations were found at lag -1 to -2, -5 to -6, and -8 to -10). The lack of any 4-5 day periodicity in Fig. 4.2 may be a consequence of using the interpolated sounding data to compute CAPE. Disturbances of this period have wavelengths of approximately 3500 km (Reed and Recker, 1971). Because of the spatial averaging that is performed in the objective sounding analysis, atmospheric conditions within the IFA are computed from soundings that span approximately 800 km when all stations recorded useable data. This distance will increase during periods when various stations did not report data or when various stations did not obtain useable data. Therefore, CAPE values obtained from the interpolated sounding data are compiled over nearly a quarter of a wavelength under ideal conditions, and over a greater fractional wavelength when some IFA soundings were unusable or missing. As indicated by Figs. 5 and 6 of Reed and Recker (1971), averaging over these distances could significantly smooth the variations of surface temperature and humidity observed over the disturbance wavelength.

The fact that rainfall-CAPE correlations from this study and that of Ushiyama *et al.*, (1995) are so low merits further discussion. Although a correlation of 0.2 is significant, this means that only a fraction of the variability in the rainfall time series can be explained by variations in CAPE. As will be discussed later in this chapter, the correlation between rainfall and CAPE will be highest for those systems that are able to fully realize the CAPE; whereas there are numerous occasions where convection may be inhibited by factors independent of CAPE, such as convective inhibition (CIN; the "negative area" between the temperature curve of a parcel lifted from the surface and the environment), mid-level dry layers and unfavorable shear conditions. Another factor that may be even more important, however, is the limited observational area of the radar. Radar-derived rainfall time series are very sensitive to the spatial distribution of rainfall over areal scales larger than their range of observation. Therefore, it is quite possible that a period characterized by high CAPE results in large rainfall amounts several days later, but not within the radar's field of view. Alternatively, if following a period of low or moderate CAPE a

highly localized, but otherwise anomalously intense rainfall event occurs within the radar's field of view, the correlation between rainfall and CAPE will also decrease.

4.1.2 Relationship between rainfall and mean vertical motion, surface wind speed

As the low correlations between CAPE and rainfall presented in the previous subsection suggest, large-scale estimates of CAPE are not sufficient to determine when and how much it rains in the IFA. Other quantities may be better indicators of convective activity. During GATE, it was noted that variations in radar-derived rainfall were generally in phase with variations of vertical motion at 700 mb (Reeves *et al.*, 1979). Furthermore, Song and Frank (1983) found that GATE rainfall was well-correlated with vertical motion at all levels up to about 200 mb, with a slight maxima in correlation occurring near 300 mb. Convective activity in GATE was strongly modulated by diurnal fluctuations of solar radiation and 3-5 day period easterly waves (Reed and Recker, 1971; Payne and McGarry, 1977; Thompson *et al.*, 1979), which were well-resolved by the GATE sounding network. In contrast, disturbances leading to convective activity during COARE were observed over a broad range of spatial and temporal scales (Chen *et al.*, 1995; Numaguti *et al.*, 1995; Ushiyama *et al.*, 1995; Haertel and Johnson, 1996; and others).

To investigate how vertical motion associated with the multitude of disturbance scales that were present during COARE relate to radar-derived rainfall, correlations of daily mean rainfall rates and daily mean vertical motion calculated from the gridded sounding data were computed for each 25-mb level between 900 and 200 mb. Correlations for the entire IOP and each individual cruise are presented in Fig. 4.3. Maximum correlation for the entire IOP is -0.67, which is in close agreement to the GATE correlations (-0.7 to -0.75) presented in Song and Frank (1983). The shape of the correlation curve is quite different, however. In GATE the correlation between vertical motion and rainfall increased steadily from -0.4 to -0.7 in the 975 to 250 mb layer, with maximum correlation occurring near 300 mb. In COARE, the IOP-mean correlation is sharply peaked at 500 mb.

Reasons for these differences are not clear, but may be related to how well vertical motions associated with various disturbance scales are resolved by the COARE sounding network, or to actual differences in vertical motion profiles for disturbances of different scales. The correlation curves for each

of the three cruises tend to support the second argument—that the vertical distribution of vertical motion varied from cruise to cruise. In Cruise 1, the correlation peaked near 300 mb, but a second peak of nearly equal magnitude is found at about 750 mb, and a weaker peak at 600 mb. The two most pronounced peaks may be a consequence of the two populations of convective features identified in Chapter 3, with the shallower population being correlated to low-level vertical motions, and the deeper population being correlated with upper-level vertical motions. The correlation during Cruise 2 was quite high (-0.83) and peaked at 575 mb. The unusually high correlations during this cruise may be related to the spatial size of rainfall-producing circulations during this cruise, as discussed in the next several paragraphs. Cruise 3 correlation peaked at about 450 mb, but was not as high as that observed during Cruise 2.

The cruise to cruise variations in maximum correlation are larger than the variations that Song and Frank (1983) presented for different GATE phases. To investigate why this may be so, it is useful to examine how the correlation between rainfall rate and diagnosed vertical motion varies with time. Fig. 4.4 presents 7-day running correlations between radar-derived rainfall and 500 mb vertical motion, as well as running correlations between rainfall and 1000 mb wind speed. For each 7-day period where daily mean rainfall rates were available, the correlation between rainfall and vertical motion, and rainfall and surface wind speed were computed. The correlation was plotted on day 4 (the central day) of each 7-day period.

When presented in this manner, deviations from cruise-mean correlations between rainfall and vertical motion are quite apparent. For example, the rain-vertical motion correlation of Cruise 1 is initially high, but quickly decreases, and does not recover until the end of the cruise. During the middle of Cruise 1, one may be tempted to conclude that rainfall is not well-correlated with vertical motion. Such a conclusion, however, is contrary to our knowledge that vertical motion is necessary for the production of rainfall. A brief convective period associated with the ISO was observed during the first two days of Cruise 1, followed by a short and weakly defined westerly wind burst. The remainder of the cruise was dominated by the "inactive" phase of the ISO (see Lin and Johnson, 1996a). Because both rainfall amounts and mean vertical motion during this inactive phase are quite low, the correlations may be unreliable. This also appears to be the case during light rainfall periods in GATE, as depicted in Reeves,

et al. (1979). Towards the end of Cruise 1 the rain-vertical motion correlation increased as the next convective phase of the ISO approached from the west, and the rainfall-vertical motion correlations once again increased.

Cruise 2 was characterized by an intense and well-defined passage of the ISO. The first few days of Cruise 2 experienced the convective portion of the ISO, which produced the highest daily rainfall rates observed during the entire IOP (see Fig. 2.10). This burst of convective activity was followed by a westerly wind burst, mean downward motion, and low rainfall rates, which also contributed to the high rain-vertical motion correlation observed during the first third of Cruise 2. As the "inactive" portion of the ISO settled into the IFA, the rain-vertical motion correlations decreased, as did the tendency for the formation of isolated convection.

Cruise 3 experienced an ISO passage that was atypical of those observed during Cruises 1 and 2. The convective portion of the ISO approached from the west, but seemed to "skip" over the IFA (see Fig. 2.8), so the most pronounced signal of the ISO during this cruise was the WWB that was most intense from Julian days 400 to about 403. Surface winds remained westerly during this cruise, so the weak easterly winds associated with the inactive phase of the ISO were never observed during this cruise.

Correlations between rainfall and surface wind speed are also quite variable during the IOP, and generally do not exceed the 95% confidence threshold. However, Fig. 2.10 indicates that there is a general tendency for rainfall and surface wind speed to increase and decrease together. Whether the surface winds respond to the dynamics of passing convective disturbances, or whether the rainfall is fed by enhanced surface fluxes driven by increased wind speeds is difficult to determine. Fig. 4.4 indicates, however, that the correlation between rainfall and surface winds is not always positive. There are four several-day periods (and one 1-day period) where the correlation between rainfall and surface wind speed is negative. Three of these periods (Julian days 321-325, 360-371, and 400-403) correspond to WWBs. Lin and Johnson (1996a) have shown that deep tropospheric shear during WWB events can reach up to 50 m s^{-1} over the depth of the troposphere, apparently prohibiting the formation of deep, well-organized convective systems and widespread rainfall during these events. Such an effect has been modeled by Weisman and Klemp (1982), who illustrated that the storm strength parameter, S—which is a function of

maximum updraft velocity—decreases to zero for Richardson numbers less than about 5, reflecting the detrimental effect that wind shear has on the growth of initial buoyant plumes. The strong shear associated with the high surface winds during WWBs is the likely cause for the negative correlation between rainfall and surface wind speed. Although the negative correlations associated with the WWBs in Cruises 1 and 3 are not significant at the 95% confidence level, the strongest surface winds of these WWBs during these cruises lasted only a few days, and may not dominate the 7-day correlations. On the other hand, the negative rain-wind speed correlation seen during the last week of Cruise 1 occurred during a very low wind, low rainfall period, so there is less reason to believe that there is a physical explanation for the negative correlations than there is for the negative correlations of Cruise 1 and Cruise 3 that occur at the time of the WWBs.

4.2 Temporal variations of convective vertical structure and relation to the large-scale environment

Chapter 3 presented approximately monthly distributions of convective feature (and grid column) heights and 30 dBZ contour heights and the rainfall associated with these features. Such distributions provide insight to the magnitude of variations that can expected over monthly time scales, which is useful for projects such as TRMM. As discussed in Chapter 2, however, atmospheric disturbances with temporal scales other than a month are frequently observed in the western Pacific warm pool region. It is of interest, then, to examine how distributions of convective properties vary from day to day and to relate the observed variations to large-scale conditions.

4.2.1 Daily variations of convective distributions

Reasons for observed variations in convective distributions may be more easily understood when placed in the context of previously identified atmospheric phenomena. In this subsection, convective variability is discussed primarily in terms of the ISO, whose progression is particularly well identified by the time series of near-surface zonal wind speeds, presented in Fig. 4.5. As Lin and Johnson (1996a) have illustrated, westerly surface winds intensify as the main convective envelope of the ISO approaches from the west, and can increase dramatically once the envelope has passed. Surface westerlies steadily decrease

in the days following a WWB, and often become weak to moderate easterlies for a brief period before returning to westerly in advance of another passage of ISO convection. The time series of Fig. 4.5 reveals that westerly surface winds are about twice as common as easterlies, so they represent a larger portion of a single ISO wavelength. However, by considering the time series of radar-identified convective echo, and wind *speed*, as well as direction, it is possible to identify the pre-convective, convective and WWB periods contained in westerly flow.

Fig. 4.6 presents time-height relative frequency distributions of convective feature and grid column heights for each cruise. Relative frequencies greater than 20% are shaded. For example, on Julian day 335, the 4-5 and 5-6 km feature height bins (Fig. 4.6a) each contain more than 20% of all observed features. A cross section along any Julian day in Fig. 4.6 when viewed along the Julian day axis would resemble a frequency distribution bar chart—such as those shown in Figs. 3.5 through 3.7 and 3.10 through 3.12—with feature height on the ordinate and relative frequency on the abscissa. Shaded areas would correspond to the taller bars (higher frequencies). The distributions of both feature and grid column height can vary substantially over periods shorter than one week. Note that, although the modal height varies with time, *at least some very deep convective features were always present.*

The first few days of Cruise 1 (Julian days 315-317) sampled convection associated with a weak convective envelope and WWB. Convective feature and grid column heights are grouped between 5 and 15 km, with very few feature (column) heights found below 5 km. On Julian day 318, the convective "envelope" of the ISO moved east of the MIT radar and surface winds increased. This transition was accompanied by a sudden shift in the distributions to lower heights. The feature distribution shows a modal height during this period of about 5 km, while the modal grid column height is 4 km, with relatively more heights at even lower altitudes. The extended period of shallow convection that is present during most of Cruise 1 was interrupted around Julian days 326 through 332, during which time daily rainfall rates (see Fig. 4.1) and convective heights increased dramatically. This brief active period was accompanied by an increase in surface westerlies (Lin and Johnson, 1996a), but it is not clear whether the westerlies were associated with the WWB or some other disturbance. The modulation of convective vertical structure will be addressed more thoroughly in the next subsection. The second period of

suppressed convection during Cruise 1 (Julian days 333-342) was accompanied by weak easterly surface flow. As the surface winds began to shift from easterly to westerly with the approaching ISO, convection again became more intense.

Cruise 2 captured both the convective and WWB portions of the ISO, as well as about a week's worth of the inactive phase. The most intense convective activity and highest daily rain rates of the entire IOP occurred on Julian day 360. Both convective feature and grid column modal heights are found at 9 and 8 km, respectively. Following the passage of the convective envelope was a particularly strong WWB which, because of the unusually strong tropospheric wind shear observed at this time, confined convection to heights well below the freezing level[2]. The lower sea surface temperatures that resulted from the strong mixing associated with the WWB may have also acted to suppress convective development. As the surface westerlies and tropospheric shear decreased, and sea surface temperatures began to recover, conditions once again became favorable for deeper convection up until approximately Julian day 372. By this time, the inactive phase of the ISO had entered the IFA and convective heights decreased.

The first several days of Cruise 3 were convectively active with the approach of the convective phase of another ISO. Judging from Fig 2.8, however, the bulk of the convective activity "leap frogged" the IFA, resulting in a quick transition from convective phase to WWB on Julian day 400. As with the WWB in Cruise 2, convective feature heights were drastically suppressed compared to their distribution during the remainder of the cruise. Once again, however, as the tropospheric shear associated with strong low-level winds decreased during early February (around Julian day 406), conditions became more favorable for convective activity. The remainder of Cruise 3 was characterized by relatively strong westerly winds, suggesting a prolonged WWB phase with this ISO passage. An inactive phase such as those observed during Cruises 1 and 2 was never observed and, consequently, convective cloud tops remained high.

---

[2] Some of the features and grid columns identified during this period (Julian days 365-368) are actually sea clutter, which could be observed up to heights of 2 km in the gridded data. The partitioning algorithm generally eliminated most of the sea clutter from the convective partition, the exception being the small ring of high reflectivities within a few kilometers from the radar.

How did the internal structure of convection vary during each cruise? Time-height relative frequency distributions of convective feature and grid column 30 dBZ contour heights are presented in Fig. 4.7. In general, the temporal trends of 30 dBZ contour height distribution are similar to those for cloud top height in Fig. 4.6, with more features and grid columns being vertically intense (as indicated by their 30 dBZ contour height) during periods of enhanced rainfall, and less intense during WWBs and inactive phases of the ISO. The tendency for the majority of convective features (and grid columns) having 30 dBZ contour heights below the freezing level (situated at approximately z=5 km), even during relatively active periods, is apparent. It is interesting to note that the modal 30 dBZ column height of convective grid columns (Fig. 4.7e) is nearly constant at 4 km throughout Cruise 2, whereas the modal 30 dBZ contour height during Cruises 1 and 3 surpasses the 5 km mark on several days. This behavior suggests that the internal vertical structure of convection during Cruise 2 is well represented by the mean reflectivity profiles presented in Fig. 3.1, whereas daily convective reflectivity profiles from Cruises 1 and 3 may be more variable.

The temporal evolution of the distribution of rainfall as a function of echo top height for each cruise is presented in Fig. 4.8 and reveals some interesting insights into the cruise-mean distributions presented in Chapter 3. For example, it is now seen that bimodal convective rainfall production during Cruise 1 was indeed accomplished by two populations of convective echo, *but these populations did not exist simultaneously*. Instead, convective rainfall fell primarily from features with tops between about 12 and 15 km (8-15 km for the grid column distributions) for most of Cruise 1, but production shifted to more shallow convection on Julian days 318 and 333 through 339. Convective rainfall production during the strong ISO passage of Cruise 2 was broadly distributed over the height bins above the freezing level. Interestingly, the grid column distribution (Fig. 4.8e) reveals that rainfall production by the very tallest grid columns peaked after the ensuing surface westerlies had subsided, and not during the main convective burst of the ISO. The presence of the more shallow cloud population seen in Cruise 1 is suggested during the inactive period of Cruise 2 (Julian days 374-380), but is masked in the cruise mean distributions by the enormous amounts of rain that fell in the first 10 days of the cruise. Rainfall

production as a function of echo top height varied little during Cruise 3, except during the WWB when almost no rain fell.

Finally, rainfall production as a function of 30 dBZ contour height is presented in Fig. 4.9. The reduced variability of 30 dBZ contour height distributions seen in Fig. 4.7 is reflected in the rainfall distributions, particularly those for the grid column 30 dBZ heights. Even during the extremely suppressed conditions of Cruise 1 (Julian days 333-339), the modal rainfall height only decreases to about 4 km compared to about 5 km for the rest of the cruise. The rainfall by height distributions are broadest towards the end of Cruise 1, and following the WWBs of Cruises 2 and 3, indicating the presence of more vertically intense features at these times. Interestingly, the distributions of rainfall as a function of 30 dBZ contour height during the main convective phase of each ISO (Julian days 315-317, 359-361, and 396-397) are *narrower* than the post-WWB distributions, suggesting that the most vertically intense convection during COARE occurred behind WWBs, rather than ahead of them.

4.2.2 Convective vertical structure as a function of ISO phase

The previous discussion suggests that convection is vertically more intense during periods of westerly surface flow than in easterly, and increases in intensity with increasing wind speed. An exception to this, of course, occurs when strong WWBs increase tropospheric shear to the extent that convection cannot develop substantially. To further investigate the relationship between convective vertical structure and ISO phase, the distribution of rainflux-weighted convective echo heights and 30 dBZ contour heights during easterly and westerly surface flow regimes were calculated and are presented in Fig. 4.10. Daily mean flux-weighted heights were computed as follows:

$$\textit{Flux-weighted height} = \overline{\left(\frac{\sum_{columns} flux \bullet height}{\sum_{columns} flux} \right)}, \qquad (4.2)$$

where the overbar represents averaging over all radar volumes analyzed in a given day[3]. Flux-weighted heights, rather than mean heights, were used in order to emphasize those grid columns that rain the most and, therefore, heat the atmosphere the most. This also reduces the influence of "false" rain arising from sea clutter, since 2 km reflectivities associated with this phenomena tend to be quite low.

The distributions of *daily mean* flux-weighted heights in Fig. 4.10 confirm that on average, convection is both deeper (i.e., taller echo heights) and vertically more intense (i.e., taller 30 dBZ contours) during westerly flow than in easterly. In both regimes, however, deep and shallow convection can be found. Although convection is generally deeper and more intense during periods of westerly surface flow, the shallowest and least vertically developed convection is found in this flow regime, apparently associated with the WWBs. Interestingly, however, the fraction of days with flux-weighted heights greater than 11 km is nearly identical for each surface flow regime: 29.3% for easterly flow versus 28.5% for westerly.

The relationship of convective vertical structure to ISO phase is further investigated by computing flux-weighted heights as a function of surface wind speed and direction. Flux-weighted heights were binned into 2 m s^{-1} 1000-850 mb zonal wind speed bins and averaged. The results are presented in Fig. 4.11. Strict comparisons between easterly and westerly regimes are only possible for zonal winds speeds up to 5 m s^{-1}, since strong easterly surface winds comparable to those seen in the westerly regime never developed. For zonal wind speeds up to 4 m s^{-1} (the upper limit of the 3 m s^{-1} bin), there is no difference in convective vertical structure between easterly and westerly regimes. At 5 m s^{-1}, however, flux-weighted heights are approximately 1 km higher in the westerly regime than in the easterly regime—a difference that is significant at the 95% confidence level. Average flux-weighted heights and 30 dBZ contour heights maximize in the 9 m s^{-1} westerly wind bin, and decrease for higher speed bins. Fig. 4.5 reveals that the two highest westerly wind speed bins are both associated with the intense WWB observed in early January.

[3] For days when all volumes were successfully collected, this represents 72 volumes at the analyzed 20-minute resolution. Fewer than 72 volumes were analyzed on days where scheduled or unscheduled radar maintenance was performed, but these occasions were infrequent.

A curious feature seen in Fig. 4.11 is the apparently anomalous decrease in flux-weighted heights for westerly surface winds in the 7 m s^{-1} speed bin. Such a decrease could result from convective heights that are uniformly lower than those of the two neighboring wind speed bins, or from a combination of deep and shallow convective heights. Fig. 4.12 presents time series of daily mean upper and lower tropospheric relative humidity, flux-weighted echo top height, and 1000 mb mean wind speed. Each of the days that fell into the 7 m s^{-1} wind speed bin of Fig. 4.11 are represented as a small diamond in Fig. 4.12b, revealing that two main groups of echo compose the flux-weighted heights in the 7 m s^{-1} bin—one from the late December convective period associated with the ISO passage, and one from the early February WWB, which accounts for the anomalous decrease in flux-weighted height for this speed bin. It is not entirely clear why deep convection was able to organize for the late December group of data points but not for those of early February. Deep tropospheric shear was actually stronger during the late December convective passage than it was during the early February WWB. A more plausible explanation may lie with the near-surface meridional winds. Fig. 4.5 reveals that both the early January and early February WWBs had strong northerly surface wind components, with the strongest northerly winds corresponding to the early February burst. Lower tropospheric relative humidity was also quite low during this period (Fig. 4.12a). Based on this evidence, it seems likely that the enhanced northerly winds the early February burst advected dry subtropical air into the IFA and thermodynamically suppressed convective development, in a manner similar to that described by Numaguti *et al.* (1995) for 4–5 day wave disturbances.

4.2.3 Convective vertical structure and tropospheric moistening

This section focuses on the modulation of convective activity by intrusions of dry subtropical air advected into the IFA at low levels by rotating disturbances, and how this behavior interacts with modulation at the ISO disturbance scale. While convection is clearly modulated by the ISO, several authors (Reed and Recker, 1971; Numaguti *et al.*, 1995; Takayabu *et al.*, 1996; Haertel and Johnson, 1996) have demonstrated that convection is also modulated on shorter time scales by rotational disturbances such as 2–day and 4–5 day waves. The time series plots of meridional wind (Fig. 4.5) and

layer-mean relative humidity (Fig. 4.12) illustrate the presence of rotational disturbances with time scales shorter than those associated with the 30–60 day ISO cycle.

To determine which of these scales are present in the variability of convective vertical structure, a spectral analysis of daily mean flux-weighted echo heights and 30 dBZ contour heights was performed. The results of this analysis are presented in Fig. 4.13. Spectral peaks are found for 2–3 day, 4–5 day, and 6–8 day periods for each cruise, which are consistent with previously documented spectral peaks found in western Pacific tropospheric wind time series (i.e., Ushiyama *et al.*, 1995; Numaguti, *et al.*, 1995, Haertel and Johnson, 1996). There is also evidence of a 13–15 day spectral peak for the flux-weighted heights (Fig. 4.13a) during Cruises 1 and 2. Although the time series data for these two cruises are only 29 and 28 days, respectively, similar frequency variations can be seen in the relative humidity time series of Fig. 4.12.

Analysis of convective vertical structure modulation by rotational disturbances and their associated dry "tongues" is somewhat more complicated than that for the ISO for several reasons. First, not all rotating disturbances advect air into the IFA. Second, widths of the dry air filaments can be quite narrow (i.e., a few hundred kilometers), and therefore not well-resolved by the sounding network (Mapes and Zuidema, 1996). Furthermore, because these dry air filaments are "entrained" into the rotating disturbances, they are not preferentially associated with any particular low-level wind direction (see the time series of two such dry air intrusions in Numaguti *et al.*, 1995), so an analysis of convective vertical structure as a function of meridional wind speed or direction produces ambiguous results. Instead, modulation of convective vertical structure by dry air intrusions is described for those cases presented in the literature.

The first dry air intrusion to the IFA while the R/V Vickers was on station occurred on 13 November 1992 (Julian day 319). Mean relative humidities in the 1000-500 mb layer (hereafter referred to as "low-level relative humidity") dropped from over 70% on 12 November to less than 55% on 13 November (Fig. 4.12a), while 500-350 mb mean relative humidity (hereafter referred to as "upper level relative humidity") also dropped almost simultaneously. Rainflux-weighted grid column heights decreased from a high of 13 km just a few days prior, to just over 8 km upon arrival of the dry air. By 15

November 1992 (Julian day 321), low-level relative humidity had recovered to about 65%, whereas upper-level humidity recovered at a somewhat slower rate. The time height cross section of tropospheric relative humidity (Fig. 4.14) reveals that the low-level relative humidity increase was primarily driven by a gradual erosion (moistening) of the inversion base with time. At the same time, the flux-weighted height of convective grid columns was increasing.

The scenario of tropospheric drying at lower and upper levels, convective suppression, and then gradual tropospheric moistening and an increase in convective intensity raises questions as to how each of these processes is regulated. Since dry tongues have been tracked backwards in time to subtropical origins (i.e., Numaguti *et al.*, 1995; Ushiyama *et al.*, 1995), it is clear that the low-level dry tongues suppress the convection, rather than suppressed convection leading to drying of the lower levels of the atmosphere. The same is not true, however, for upper tropospheric drying and moistening. Udelhofen and Hartmann (1995) used IR (11 μm) and water vapor (6.7 μm) data to study the relationship of upper tropospheric (i.e. 550-200 mb) moistening to convective activity. They found that upper tropospheric humidity (UTH) decreases from values of 44-74% near the edges of upper tropspheric clouds to 11-15% at distances of about 500 km or more. Furthermore, they found that the "dispersal" of UTH from cloud edges was least for suppressed convection, and that UTH dispersal increased with increasing cloud top height. Finally, they found that the diurnal variation of UTH lags that of upper tropspheric cloudiness by about 8 hours. Therefore, the drying of the lower and upper troposphere during the 13–16 November 1992 dry intrusion appear to be linked by convection as follows: low level dry air suppresses convective cloud tops via enhanced stability and entrainment of dry air into convective towers, which in turn reduces the moisture source for the upper troposphere, leading to drying.

The remoistening of the troposphere again is linked to convective activity. Surface wind speeds during this period are about 2 m s^{-1} and apparently provide enough moisture flux from the ocean surface to maintain convection, as evidenced by the rainfall time series in Fig. 2.10. Moisture that is detrained from convection erodes the base of the dry layer and gradually creates a more favorable environment for deeper, subsequent convection. As convection reaches higher altitudes, moistening of the upper

troposphere becomes more efficient, as described in Udelhofen and Hartmann (1995). Based on the cross sectional zonal wind time series of Lin and Johnson (1996a), the 13–16 November 1992 dry intrusion occurred as winds associated with the early November WWB were decreasing, but before the inactive phase of the ISO was situated over the IFA. The scenario just described is quite similar to the dry intrusion of early February (Julian days 400 to about 406) described by Yoneyama and Fujitani (1995), except surface winds were stronger during this period and recovery times for tropospheric humidity are faster.

A third dry intrusion described by Numaguti *et al.* (1995) occurred on 25–26 November 1992 (Julian days 331–332). However, as was pointed out by Mapes and Zuidema (1996), this intrusion was only sampled by the northernmost stations composing the IFA, so its presence is not apparent in Fig. 4.12. Immediately following this dry intrusion, however, are decreases in upper and lower level relative humidities and flux-weighted cloud top height (beginning around Julian day 336). Although the behavior of these three variables is quite similar to that discussed for the 13–16 November dry intrusion, the suppressed conditions appear to be a consequence of the inactive phase of the ISO being situated over the IFA, rather than due to suppression by a dry layer. The dramatic drying of the upper troposphere during this period is accompanied by only moderate drying of the lower troposphere (see Fig. 4.14). Furthermore, surface winds reach their lowest speeds observed during the entire IOP in this period (similarly low surface winds are observed in the second week of January), resulting in the lowest surface fluxes observed during the IOP (Lin and Johnson, 1996b). Apparently, although surface winds are non-zero during calm surface wind conditions, they were too low during the inactive phase of the MJO to support widespread convection.

Recovery times for both upper and lower relative humidity in early December is about 10 days. Interestingly, flux-weighted echo top heights appear to recover somewhat faster than upper tropospheric relative humidity, which seemingly conflicts with the conclusions of Udelhofen and Hartmann (1995). However, in his analysis of the horizontal organization of convection, Rickenbach (1995) showed that this entire 10–day period was characterized by widely spaced isolated convective cells. Therefore, even though the convection that produced the most rainfall was relatively deep, the fact convective features were few

and far between limited the rate of IFA-mean moistening in the upper troposphere. The sequence of events just described are consistent with the observations during the second inactive phase of the ISO that occurred in the second week of January.

The next occurrence of tropospheric drying for which convective structure data are available is the late December-early January WWB. As has been seen previously, the strong tropospheric shear that occurs with WWBs can suppress convective activity by inhibiting its ability to organize beyond isolated convection. Using the same reasoning for the inactive phase of the ISO, the scant and unorganized convection typical of WWBs may lead to drying of the upper troposphere. However, low-level relative humidity during this period is lower than those for the inactive ISO phase "drying" periods (centered on Julian days 337 and 377). Sheu and Liu (1995) studied the behavior of dry intrusions during COARE using SSM/I data and have attributed this low-level drying to the advection of dry subtropical air into IFA by a mid-latitude cold surge which preceded the early January WWB. Note that the late January WWB (Julian days 395 to about 399) was characterized by a decrease in flux-weighted cloud top heights towards the end of the burst, but no decrease in tropospheric humidity. Apparently, tropospheric drying does not always accompany WWBs.

The proposed chains of events for each of the described upper tropospheric drying mechanisms are summarized as flowcharts in Figs. 4.15 through 4.17. Two of the mechanisms are directly tied to the phase of the ISO, while the "dry intrusion" mechanism (Fig. 4.15) is related to higher frequency rotational disturbances. It is possible that the drying mechanisms associated with these higher frequency disturbances can enhance the drying associated with either the inactive or WWB phases of the ISO. For example, a dry intrusion just prior to the onset of the inactive phase of the ISO may prolong the moisture recovery period by providing a few additional days of upper tropospheric drying time. In another example, dry air may be advected near, but not into, the IFA by a high frequency disturbance and then may be incorporated into the drying associated with the WWB.

4.3 Convective heating profiles

The previous section discussed how convective vertical structure is modified on various spatial and temporal scales and how these modifications both impact and respond to tropospheric moistening. Of course, convection is also a source of diabatic heating in the atmosphere. This section presents a new method of computing convective heating (Q_{1c}) profiles by combining the interpolated sounding and radar data sets. How the shape of the Q_{1c} profiles varied from cruise to cruise and as a function of surface flow regime is also examined.

4.3.1 Computation of convective heating profiles

Mr. Xin Lin of Colorado State University computed Q_1 profiles every six hours using the interpolated sounding data and kindly provided the results for this study. The method of computation is presented in Lin and Johnson (1996b), and is similar to that of Yanai *et al.* (1973). These profiles represent the combined heating from both convective and mesoscale (i.e. stratiform) precipitation. Johnson (1984) presented a method of partitioning heating profiles into convective and mesoscale components using an assumed mesoscale heating profile shape. Mathematically, Q_1 is the sum of the heating profiles resulting from convective, mesoscale, and radiational heating:

$$\hat{Q}_1 = f\hat{Q}_{1m} + (1-f)\hat{Q}_{1c} + \hat{Q}_R \tag{4.3}$$

where Q_1 is the total heating, Q_{1c} is the convective heating, Q_{1m} is mesoscale heating, Q_R is radiational heating (longwave plus shortwave), f is fraction of total precipitation falling from mesoscale anvils (stratiform cloud), and the caret refers to normalization by rainfall rate. It should be noted that Q_1 and Q_R are normalized by the *total* (convective plus stratiform) rainfall rate, Q_{1c} is normalized by the convective rainfall rate, and Q_{1m} is normalized by the stratiform rainfall rate. Johnson (1984) computed Q_{1c} profiles based on composite Q_1 profile presented in Yanai *et al.* (1973). He assumed a fixed value of $f = 0.2$ and used composite rainfall rates based on observations to normalize the heating profiles. Daily mean Q_R estimates presented in Cox and Griffith (1979) were also used. Johnson's results indicate that the composite Q_{1c} profile peaks at about 650 mb for $f = 0.2$, but varies between 600 and 700 mb if f is allowed to vary from 0.1 to 0.3.

Equation 4.3 is also used to compute Q_{1c} in this study, except the calculation is performed for every 6 hour Q_1 profile closest to the R/V Vickers (2°S 156°E), rather than for a time-mean composite Q_1 profile. Such a high temporal resolution introduces a few complications to the Q_{1c} estimate. The first issue that must be addressed is how to compute f. Computation of the stratiform contribution to total rainfall over any time period greater than 20 minutes is a simple task with the partitioned rainfall results. The real issue, however, is to determine an appropriate averaging period for the computation of f, since the heating "sensed" by the sounding network arises from precipitation that was formed prior to the sounding launch. In his analysis of buoyancy bores associated with vertical heating profiles, Mapes (1993) estimates that buoyancy bores emanating from a localized heat source travel at about 50 m s^{-1}. The spacing of soundings in the eastern IFA (corresponding to the area observed by the MIT radar) is about 400 km, whereas the distance between opposite corners of the IFA is approximately 800-900 km. Assuming that the precipitation observed by the MIT radar has stratiform rain fractions representative of those over the IFA, these figures would suggest that an averaging time of 2-4 hours prior to sounding launch should be used to compute f. However, because rainfall is so variable over small spatial scales, an averaging time of 6 hours prior to sounding launch was used to compute f in an effort to obtain a value more representative of the IFA.

A second issue that must be addressed is how to handle variations in the radiative heating profile. Cox and Griffith (1979) present hourly total radiative heating profiles for the GATE region for both disturbed and undisturbed conditions. Their Table 1 presents the distribution of cloud top pressure during each set of conditions. For disturbed conditions, the modal cloud top pressure is 250 mb and drops to 600 mb for undisturbed conditions. More than 60% of the cloud cover during disturbed conditions in GATE had cloud top pressures lower than 500 mb, while more than 60% of cloud cover during undisturbed conditions had cloud top pressures higher than 500 mb. Using the height data provided with the COARE gridded sounding data, the mean height of the 500 mb pressure level was computed to be about 5.5 km.

This height was compared the modal height of convective grid columns in the hour prior to sounding launch[4] to determine if the disturbed or undisturbed radiative heating profile should be used.

It should be noted that even the undisturbed conditions summarized in Cox and Griffith (1979) correspond to widespread cloud cover. Clear sky represents only 4.8% and 23.2% for the sky cover for disturbed and undisturbed conditions, respectively, as reported in Table 1 of Cox and Griffith. During COARE, however, there were several periods (most notably associated with the inactive phase of the ISO) where nearly completely clear sky conditions existed, making use of the Cox and Griffith profiles inappropriate. Xin Lin of Colorado State University provided total radiative heating profiles calculated from the 6-hourly temperature and moisture variables from the gridded sounding data using the NCAR CCM2 radiative transfer code. A subjective definition of clear sky conditions was used to identify "clear sky" periods based on a combination of IFA-mean IR brightness temperature and fractional areal coverage of precipitation as determined by the MIT. The clear sky radiative heating profiles were used when the IFA-mean brightness temperature was $\geq$ 275K *or* when the fractional area of precipitation was $\leq$ 10%.

Finally, two different Q_{1m} profiles were used in separate Q_{1c} calculations: a vertically smoothed version of the mesoscale heating profile of Houze (1982) and the Q_{1m} profile diagnosed by Johnson and Young (1983) during the Winter MONEX field project, north of Borneo. While each mesoscale profile produced similar Q_{1c} profiles when averaged over each cruise, the Q_{1m} profile of Johnson and Young (1983) tended to produce Q_{1c} profiles that resembled a negative Q_{1m} profile on days that were characterized by heavy precipitation and larger-than-average values of f (i.e., strong heating at low levels and strong cooling at upper levels). A comparison of the Johnson and Young Q_{1m} profile to that of Houze is presented in Fig. 9 of Johnson and Young (1983). While the shapes of the two curves are similar, peak heating and cooling rates in the Johnson and Young Q_{1m} profile are about 5°C greater than those obtained by Houze (1982). R. Johnson (personal communication; 1995) felt that the enhanced cooling of the Johnson and Young Q_{1m} profile may be a consequence of enhanced evaporative cooling resulting from

[4] The averaging time for convective cloud top height distributions is only one hour (as opposed to six hours for the computation of f) because the radiative heating "sensed" by the sounding emanates from the sounding trajectory, rather than from remote precipitating systems.

strong and dry low level northerly winds over the South China Sea during the winter months. Daily Q_{1c} profiles computed using the Houze (1982) Q_{1m} profile eliminated the occurrence of "negative Q_{1m} profiles", so this is the profile used in the Q_{1c} calculations.

4.3.2 Q_{1c} profiles during COARE

Time series of daily mean Q_{1c} profiles, as well as the cruise-mean average, are presented in Fig. 4.18. The profiles are not normalized by rainfall rate so that the variability of heating from day to day and cruise to cruise may be seen. Convective heating naturally increases during periods of heavier rainfall and tends to maximize near 750 to 500 mb. Two exceptions concerning the vertical location of maximum heating are seen on Julian days 361 and 400. On these days, the diagnosed convective heating bears a close resemblance to Q_{1m}, suggesting that the value of f on these days underestimated the relative amount of stratiform precipitation falling beyond the area of analyzed radar data. Aside from these two days, there are also several occurrences of negative values of Q_{1c}, which is a physically unrealistic condition. Although negative Q_{1c} values are scattered throughout the time-height cross sections, they are most prevalent during periods of very light winds (i.e., Julian days 317, 324-328, 336-338, 342, and 373-377). During these light wind profiles, relatively large errors in divergence (and therefore vertical velocity) calculations may result from small differences in wind speed and direction. Fortunately, very little rainfall fell during these periods, so their effect on the cruise-mean Q_{1c} profiles is not very great. Because so many assumptions and estimates of variables go into the calculation of Q_{1c}, the shape of the Q_{1c} profile on any given day may not be very accurate. However, assuming these errors are distributed randomly from day to day, average profiles obtained over several days should be physically meaningful.

The cruise-mean profiles presented in Fig 4.18 reveal that the vertical placement of maximum convective heating varies from cruise to cruise. The mean profiles are averages of all data points, both positive and negative. When only positive convective heating values are averaged, the magnitude of heating increases, but the shapes of the curves and the levels of maximum heating do not change. Similarly, eliminating Julian days 361 and 400 from the averaging results in only minor changes in the profile shapes, and has no impact on maximum heating levels. Heating (and rainfall) was greatest during

Cruise 2, despite the fact that cruise-mean CAPE values were the smallest during this cruise. A discussion of this phenomena is given in section 5.2. Referring back Fig. 3.2, it is seen that the *shapes* of the cruise-mean Q_{1c} profiles vary in a manner consistent with shapes of the cruise-mean buoyancy profiles. For example, there is about 1°C less thermal buoyancy at all levels during Cruise 2 than in Cruises 1 and 3. Invoking arguments similar to those used in Zipser and LeMone (1980), this should, on average, result in weaker updraft velocities for Cruise 2 convection which would limit the depth of condensational growth of water and raindrops, therefore concentrating convective heating in the lower levels of the troposphere. In contrast, there is more buoyancy on average during Cruises 1 and 3, and the heating profiles maximize at higher levels. Maximum heating during Cruise 1 is located between 500 and 350 mb, whereas maximum heating in Cruise 3 peaks at 500 mb. The slightly higher level of maximum heating in Cruise 1 is consistent with the slightly greater buoyancy in the 500-350 mb layer compared to that of Cruise 3. Also, Fig. 3.1 reveals that cruise-mean reflectivity profiles in this layer (near 8 km) increase by about 0.6 dBZ with increasing buoyancy—a small but statistically significant difference (Cruise 2: 13.1 dBZ, Cruise 3: 13.7 dBZ, Cruise 1: 14.2 dBZ).

The Q_{1c} time series also provides a method to study the shape of convective heating profiles for easterly and westerly surface flow regimes. Mean Q_{1c} profiles are computed for the 16 days of easterly surface flow and the 63 days of westerly surface flow for which radar-derived rainfall estimates are available. These results are presented in Fig. 4.19a. Although there is greater heating with westerly flow than with easterly flow, the peak heating is shifted upward in easterly flow (Q_{1c} peaks at 450 mb in easterly flow compared to 600 mb for westerly flow). Furthermore, convective heating peaks just below the level of maximum thermal buoyancy for each regime (Fig. 4.19b).

Although the heating profiles results for each flow regime are consistent with the buoyancy profiles, there is an apparent inconsistency with the results presented in Fig. 4.10—namely that convection is, on average, shallower and less vertically intense during periods of easterly surface flow than in westerly. Why is it then, that a regime dominated by shallow, less vigorous convection has its peak heating rate higher than the deeper and more intense westerly flow regime? This apparent paradox is resolved when the contribution to total rainfall by the daily mean flux-weighted heights of Fig. 4.10a are

considered. Five of the 16 days of easterly flow fall into the three tallest flux-weighted height bins of Fig. 4.10a (i.e., 11-14 km). These five days represent five of the six highest daily mean rainfall rates observed in the easterly flow regime and account for 66.7% of the total precipitation that fell during periods of easterly surface flow. In contrast, only 57.9% of the total precipitation that fell during westerly surface flow is accounted for in the three tallest height bins. Therefore, shallow convection during westerly flow made a larger contribution to convective heating in the westerly flow regime than it did in the easterly regime.

Given the differences in heating profile shapes and their apparent relation to the vertical distribution of buoyancy, the next logical question to ask is what controls the buoyancy distribution in easterly and westerly surface flow regimes. Thermal buoyancy is primarily a function of the moisture content of the lifted parcel and of the stability of the troposphere, so both of these factors must be considered when discussing buoyancy controls. As Lin and Johnson (1996a) have demonstrated, sea surface temperatures during the inactive (usually easterly surface flow) phase of the ISO are 1-1.5°C higher than during westerly surface flow associated with the convectively active and WWB phases of the ISO. Two factors account for this difference: first, more insolation reaches the ocean surface during the less cloudy inactive phase and, second, the generally weaker easterly surface winds result in less mixing of the ocean surface waters, thereby preventing cooling of the ocean surface by mixing with cooler water below. The warmer ocean temperatures translate to a warmer boundary layer, thus increasing the potential buoyancy of near-surface parcels.

Thermal buoyancy is also affected by the atmospheric temperature profile. A temperature profile that lies closer to the dry adiabatic lapse rate will result in greater buoyancy for a lifted parcel than one that is more stable. Furthermore, the presence of stable layers (temperature inversions) will also reduce the buoyancy experienced by a rising parcel. Buoyancy differences between easterly and westerly surface flow regimes are greatest above 500 mb. Johnson *et al.* (1996) have discussed the prevalence of two types of stable layers near the 0°C level (typically around 550 mb). The first type of stable layer is associated with precipitating systems is characterized by anomalously cool and moist conditions and is located just

below the freezing level. The second type, which tended to occur outside of precipitating areas, is found just above the freezing level and is associated with anomalously warm and dry conditions. Johnson *et al.* (1996) argue the first type of stable layer is associated with melting within stratiform cloud, while the second type may be a consequence of advective, radiative, gravity wave and/or melting effects. Fig. 16 of Johnson *et al.* (1996) suggests that these mid-level stable layers are no more frequent during periods of widespread precipitation (generally westerly surface flow) than during relatively rain-free (easterly flow) periods, although most of the layers are of the first type during precipitating periods, whereas the second type dominates the more undisturbed conditions. Since the *frequency* of stable layers does not differ significantly during periods of easterly and westerly surface flow, yet the *type* does, it is possible that the moist/cool (westerly) stable layers are more stable and/or areally more extensive than those of the warm/dry (easterly) regime. Neither Johnson *et al.* (1996) nor Mapes and Zuidema (1996) examine degree of stability as a function of surface flow regime, so this impact on buoyancy cannot be investigated with the published literature.

4.4 Summary of findings

Variations of convective activity—as indicated by time series of rainfall and of convective echo distributions—were examined with respect to their response to and impact on environmental variables. Lag correlations between rainfall and CAPE were low, but statistically significant, and indicate that rainfall maximized approximately three days after CAPE, and that CAPE decreased 3-4 days following a rainfall event. A similar lag in rainfall was observed by Ushiyama *et al.* (1995). The low correlations between CAPE and rainfall suggest that other factors, as well as CAPE, control the timing and intensity of rainfall.

For seven day periods, correlations between radar-derived rainfall and sounding-derived vertical motion ranged from -0.2 to almost 1.0. Correlation decreased during periods of light winds and weakly organized convection, suggesting that the scales of motion that produced were frequently too small to be adequately resolved by the sounding network and/or that divergence estimate errors increased during periods of light wind, therefore reducing the correlation. Rainfall tended to be positively correlated with

surface wind speed, except during WWBs, when tropospheric shear increased to the point where convection could not easily develop into organized systems.

Daily mean distributions of convective heights and 30 dBZ heights reveal that at least some deep convection was always present—even during periods when convective activity is quite low. Modal convective heights varied from less than 5 km to 13 km over the course of just one day. Variability of 30 dBZ contour height distributions were not as dramatic, but varied in a manner temporally similar to those of echo top heights. Convective rainfall was often produced by two different populations of convective cloud—one deep and vertically intense, and another that was shallow and less vertically intense—although it appears that these two populations did not exist simultaneously. Convective heights and 30 dBZ contour heights were substantially suppressed during WWBs and—at least in the two convective-WWB cycles sampled—reached their maximum vertical development as winds associated with the WWB decreased and not during the passage of the main convective envelope of the ISO.

Daily mean rainflux-weighted echo heights tended to be greater during easterly surface flow regimes than during easterly, however the shallowest flux-weighted heights were found in the westerly regime and were associated with the WWBs. For surface wind speeds greater than about 4 m s^{-1}, flux-weighted echo heights were shallower during easterly surface flow than during westerly.

Suppression of convective heights was associated with three distinct phenomena: low-level intrusions of subtropical dry air into the IFA, low surface wind speeds characteristic of the inactive phase of the ISO, and WWBs. In each case, suppression of convective vertical development led to upper tropospheric drying. Convective heights increased and upper tropospheric moistening resumed as the "suppressing" condition weakened (i.e., as the low-level dry tongue was eroded by detraining water vapor from its base upward, or as surface winds increased or decreased for inactive and WWB phases of the ISO, respectively).

Profiles of convective diabatic heating were computed using a combination of sounding-derived total diabatic heating, radar-derived rainfall amounts, and idealized and calculated radiative heating profiles. Instantaneous convective heating estimates are subject to potentially large, but probably random, errors, so the results are most meaningful when averaged over several days. Cruise-mean convective

heating profiles reveal variations in the placement of maximum heating for each cruise, which are qualitatively consistent with the cruise-mean buoyancy profiles presented in Chapter 3. Convective heating profiles observed during easterly and westerly surface flow regimes are also qualitatively consistent with buoyancy profiles from each of these flow regimes, with heating peaking near 500 mb during westerly surface flow and near 300 mb during easterly flow. The locations of maximum convective heating are somewhat surprising considering the distribution of rainflux-weighted heights for each flow regime. However, a larger fraction of the rainfall during the easterly regime was associated with the tallest flux-weighted height days than during the westerly regime, so the results are not as paradoxical as they may first seem. Factors that may control the vertical distribution of buoyancy (and apparently heating profiles, too) are warmer sea surface temperatures characteristic of the inactive (easterly) phase of the ISO and possibly stronger mid-level stable layers during the active (westerly) phase.

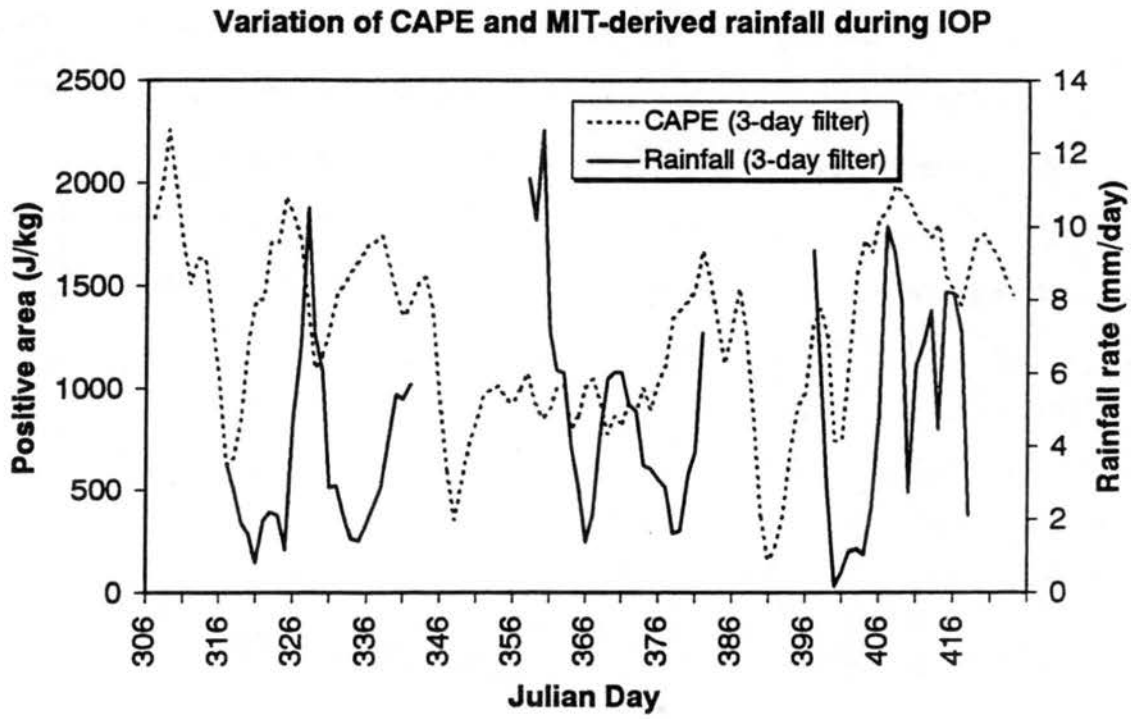

Fig. 4.1 Time series of IFA-mean convective available potential energy (CAPE) and MIT-derived rainfall during the COARE IOP. CAPE is computed for a parcel with temperature and moisture properties of the mean 1000-960 mb level lifted irreversibly.

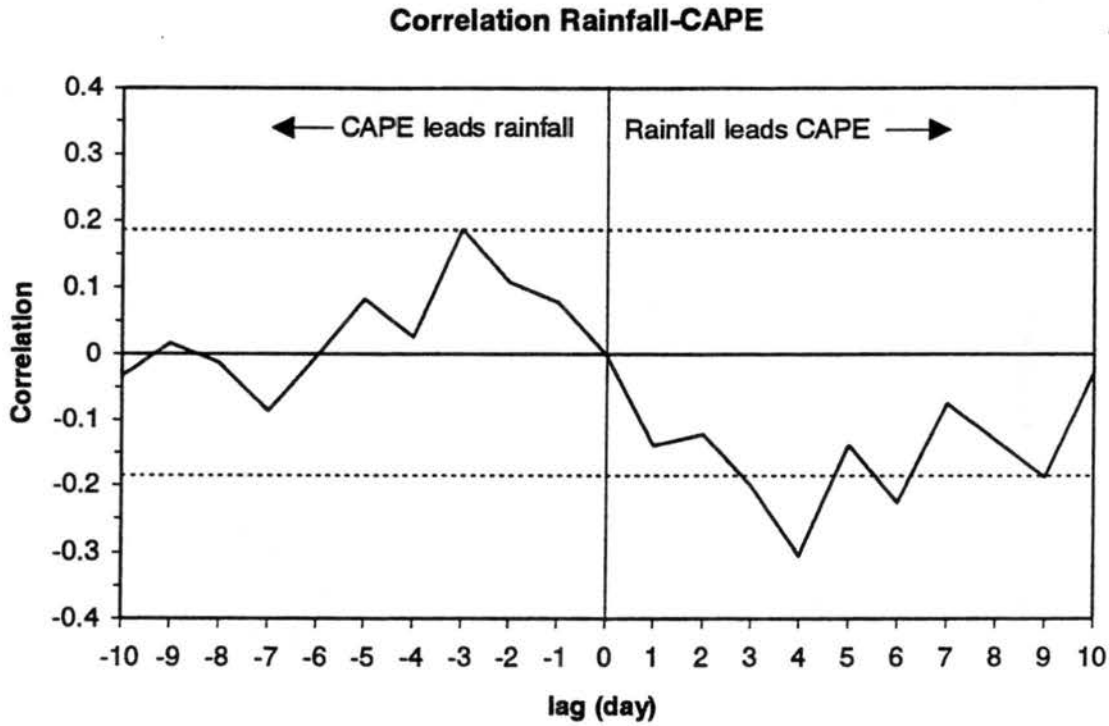

Fig. 4.2 Lag correlations for CAPE and rainfall. Dashed lines represent 95% confidence levels.

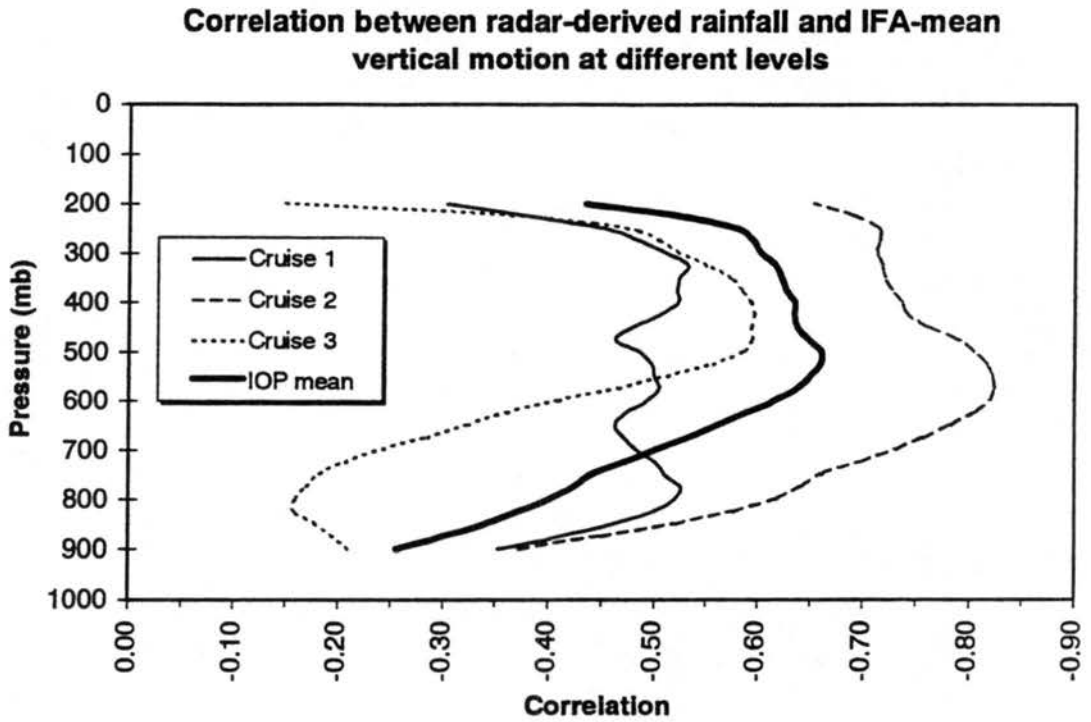

Fig. 4.3 Correlations between MIT radar-derived rainfall rate and IFA mean vertical motion at different levels for each cruise and for the COARE IOP.

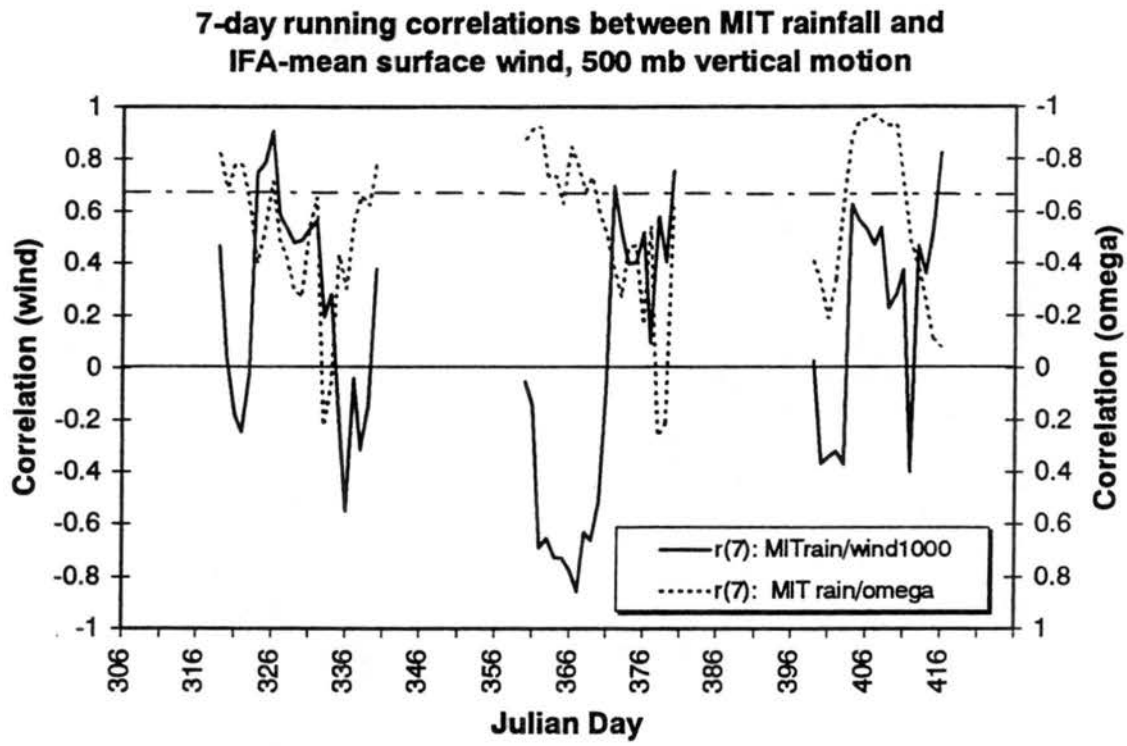

Fig. 4.4 Time series of 7-day correlations between rainfall and 1000 mb wind speed (solid line) and rainfall and 500 mb vertical velocity (dotted line). 7-day period correlations are plotted on day 4 of each period. Thin dashed-dotted line indicates 95% confidence level.

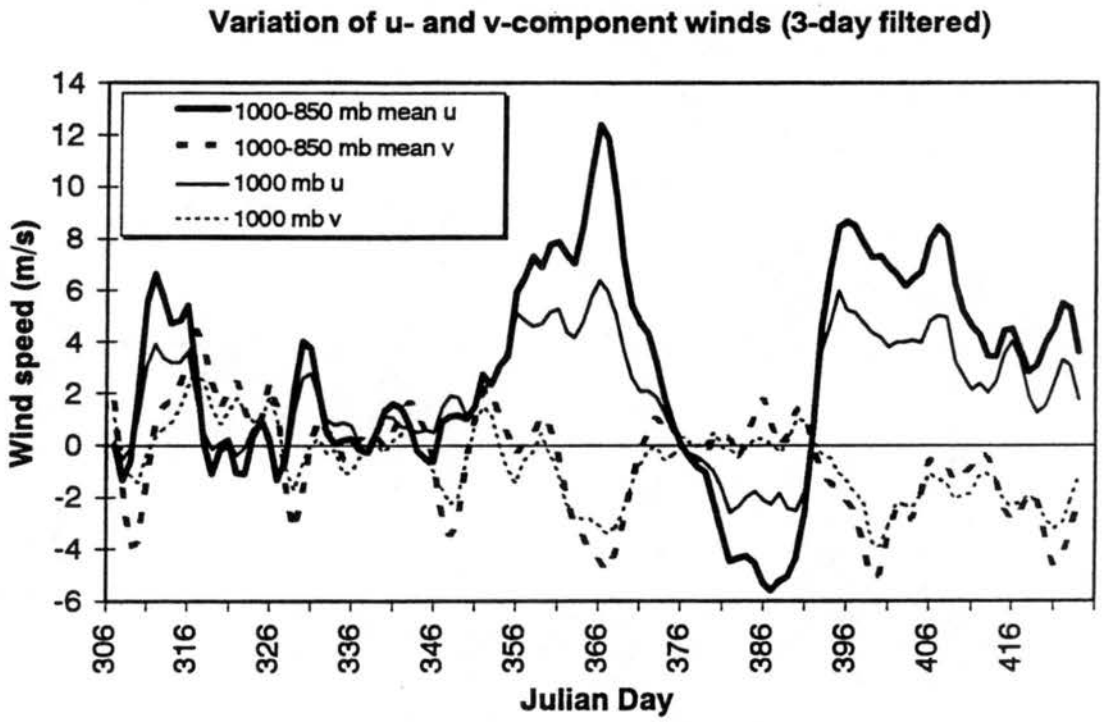

Fig. 4.5 Time series of IFA mean zonal u- (solid) and v- (dashed) component winds at 1000 mb (light lines) and averaged over 1000 to 850 mb (heavy lines). A three-day running mean has been applied to the data.

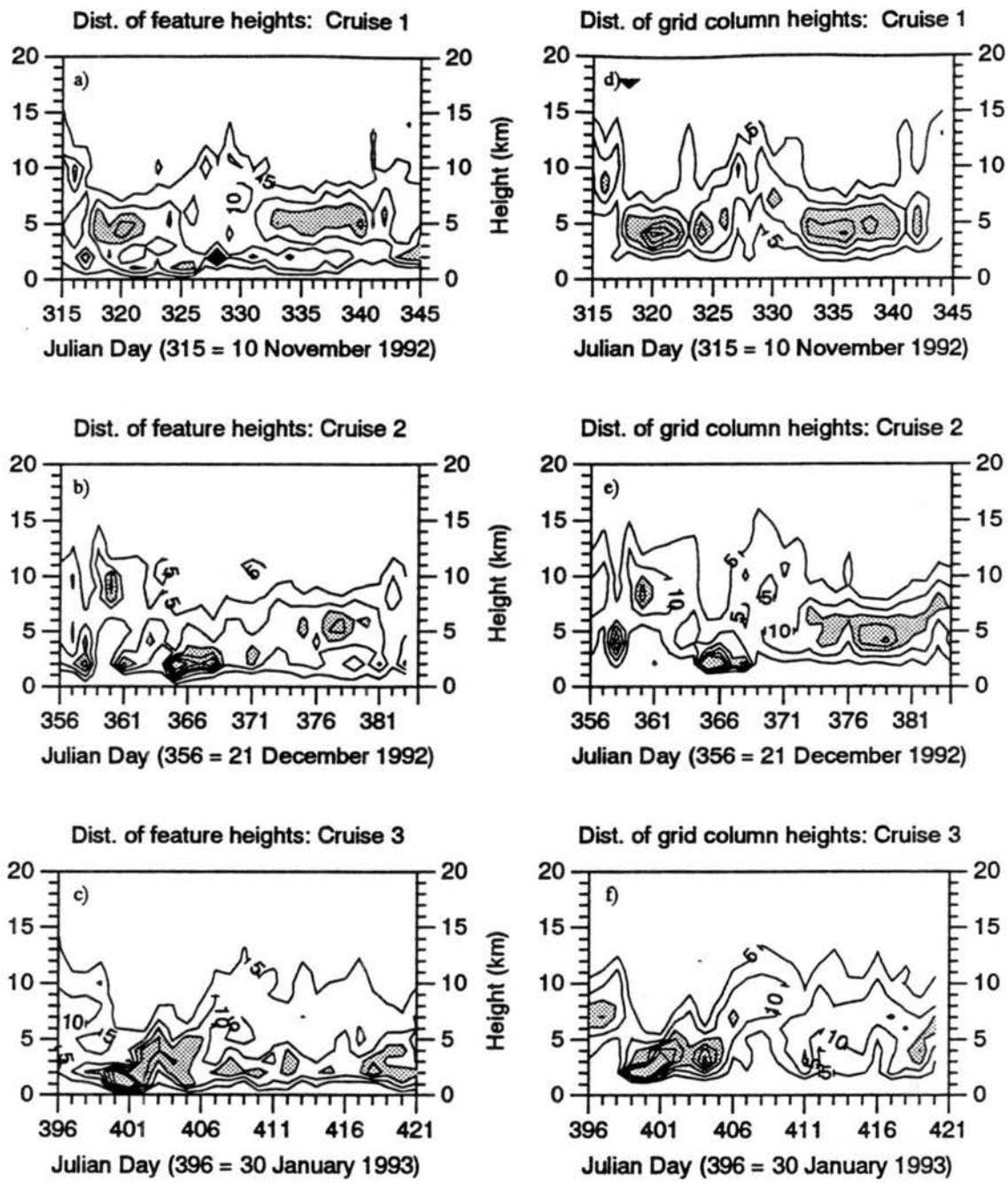

Fig. 4.6 Relative frequency distribution of convective feature heights (panels a-c) and convective grid column heights (panels d-f) for each cruise of the R/V Vickers. Relative frequencies are contoured at 1, 5, 10, 20, 30, and 40 percent. Frequencies greater than 20% are shaded.

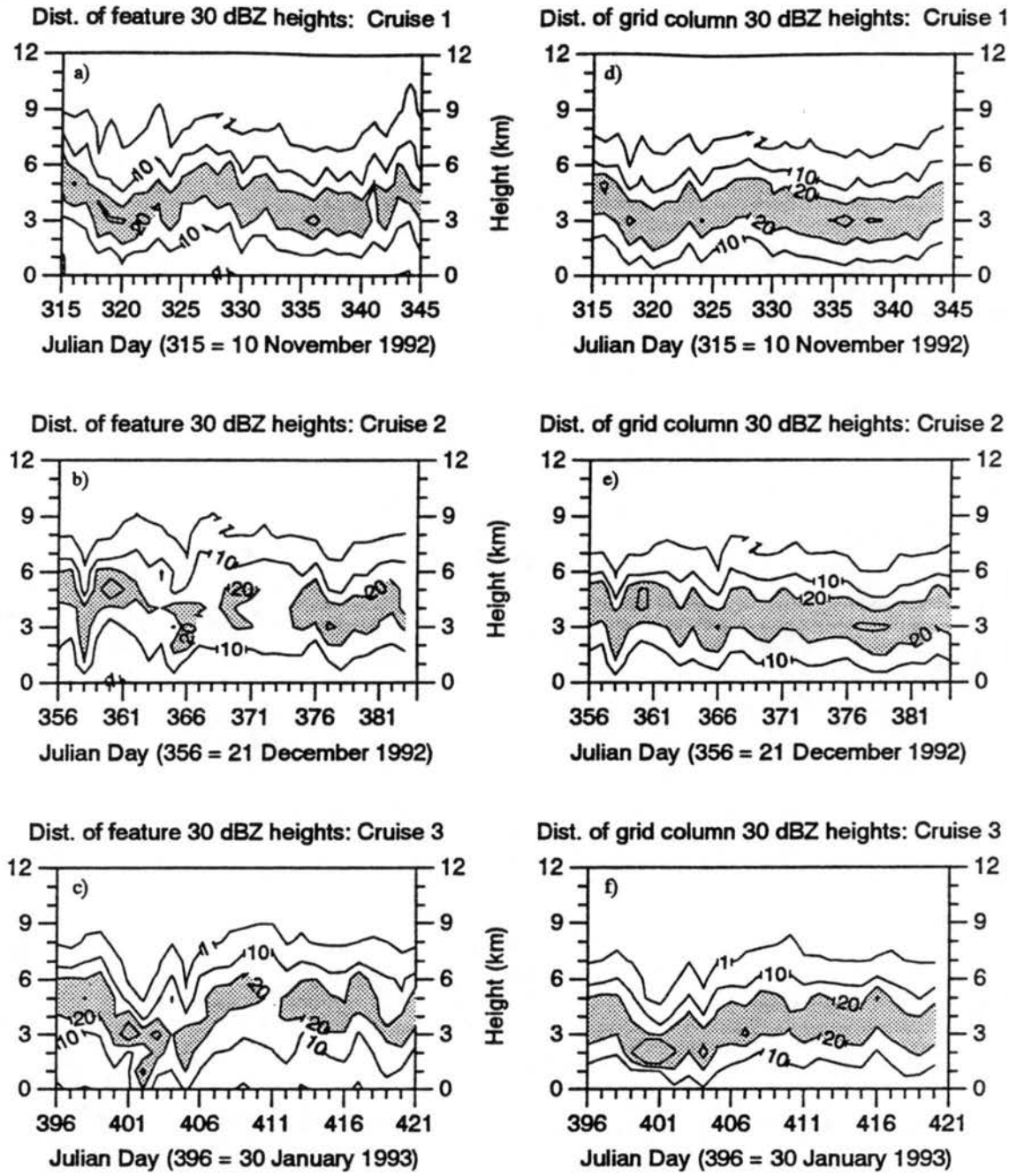

Fig. 4.7 As in Fig. 4.6, but for 30 dBZ contour heights. Relative frequencies are contoured at 1, 10, 20, and 30 percent.

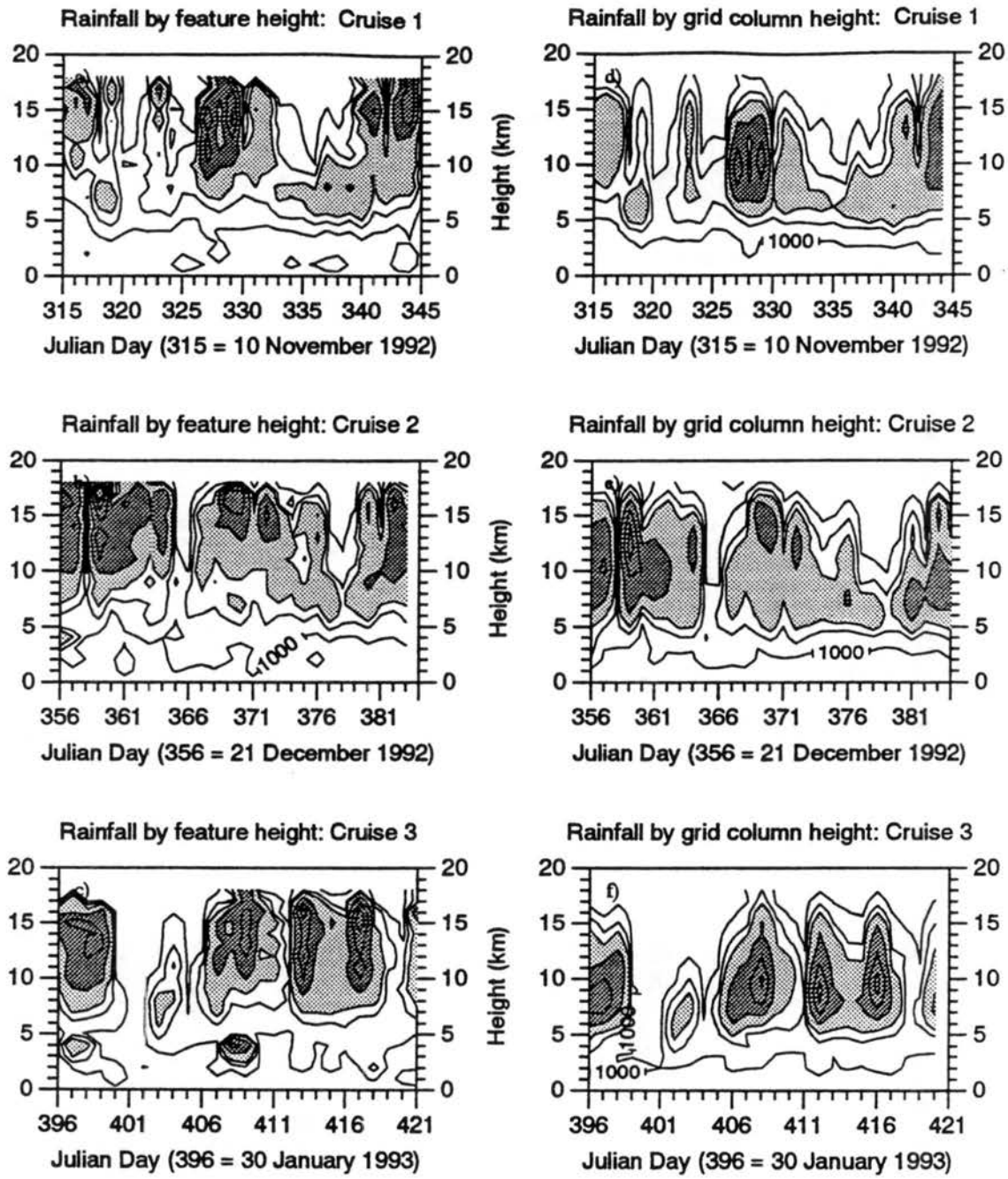

Fig. 4.8 Distribution of rainfall contribution as a function of convective feature height (panels a-c) and of convective grid column height (panels d-f). Rainfall units are $m^3 s^{-1}$ and are contoured at intervals of 1000, 5000, 1E+04, 2.5E+04, 5E+05, and 7.5E+04. Fluxes greater than 1E+04 are lightly shaded, while those greater than 2.5E+04 are darker shaded.

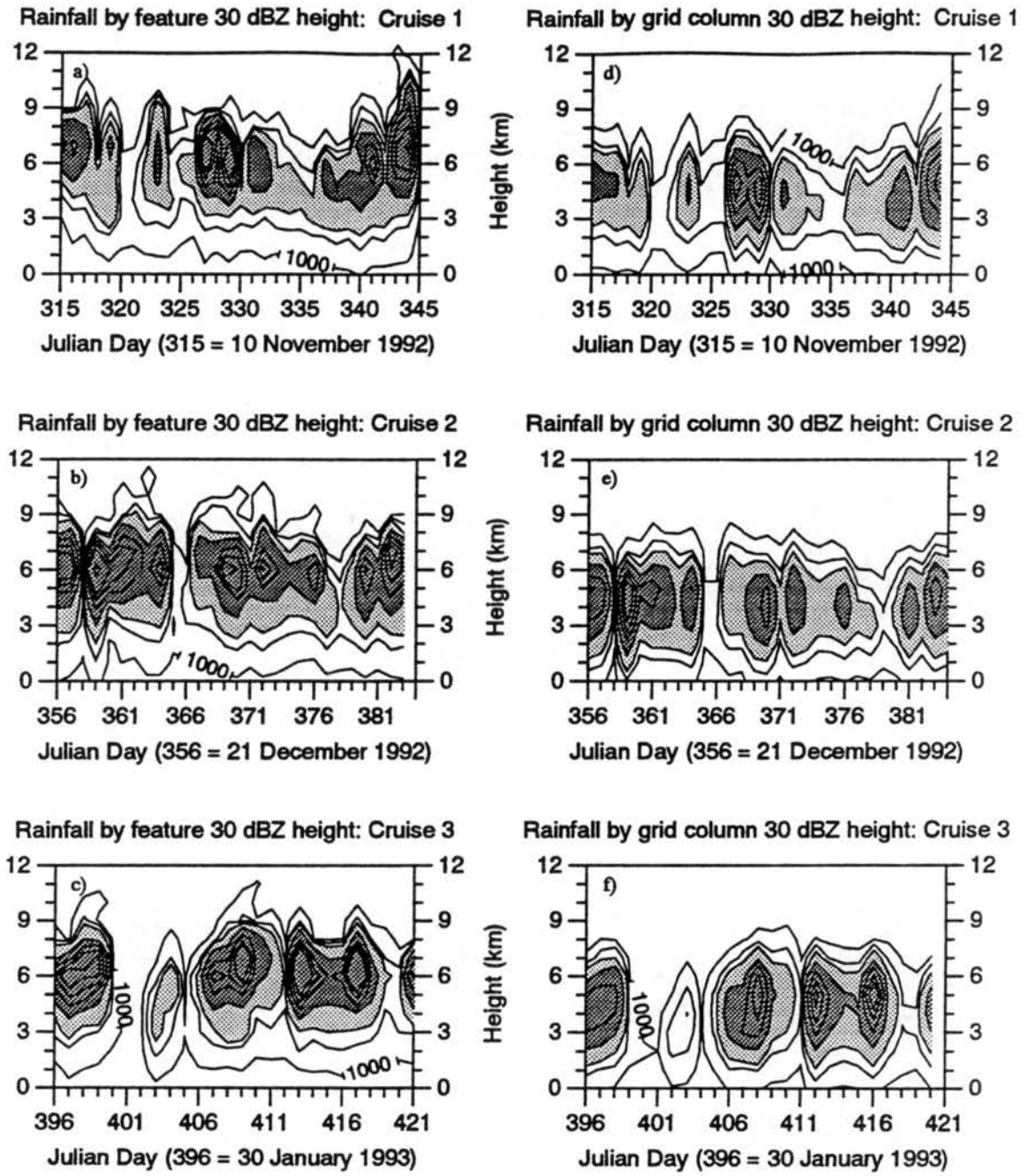

Fig. 4.9 As in Fig. 4.8, but for 30 dBZ contour heights.

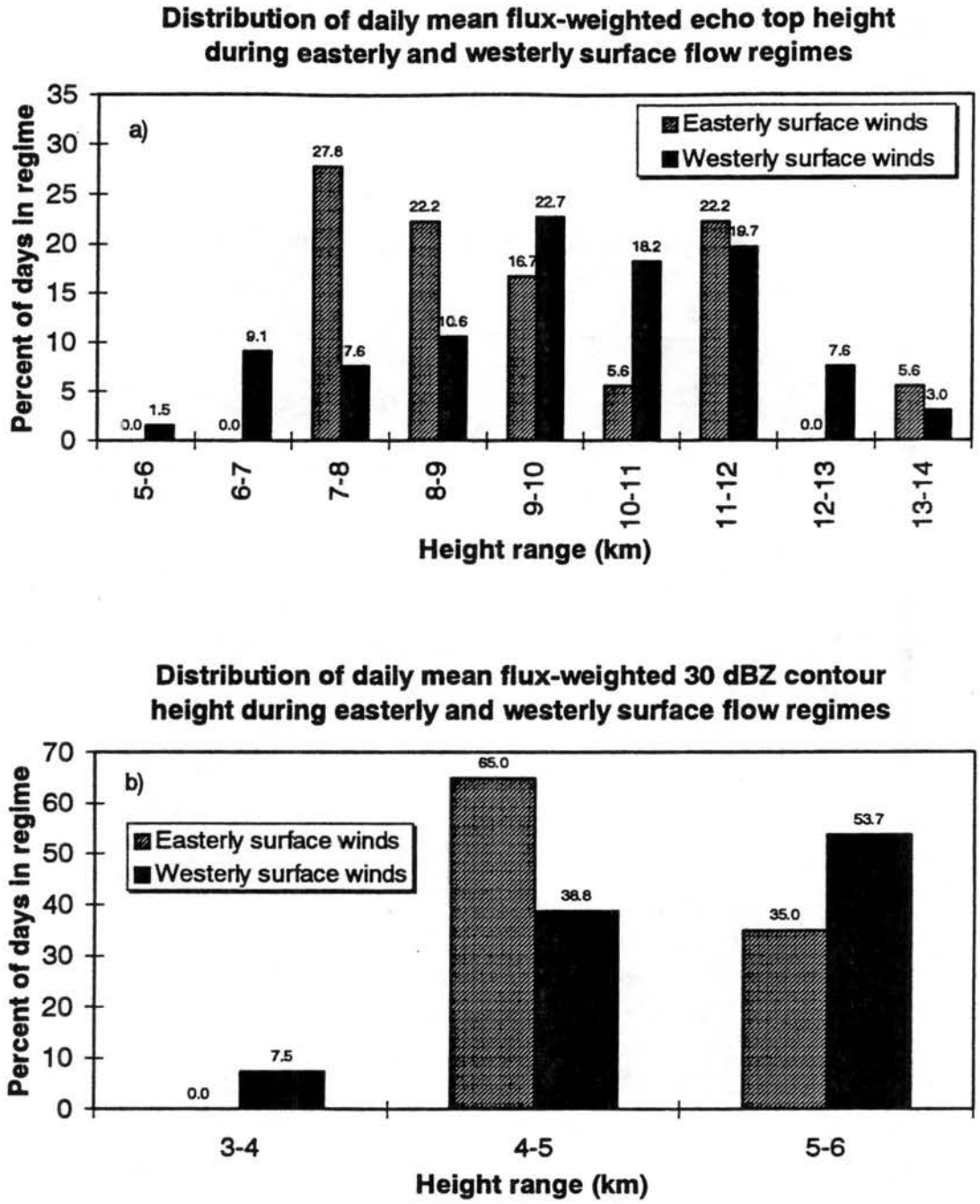

Fig. 4.10 Distribution of daily mean rainflux-weighted convective grid column heights (a) and 30 dBZ contour heights (b) for easterly and westerly surface flow regimes.

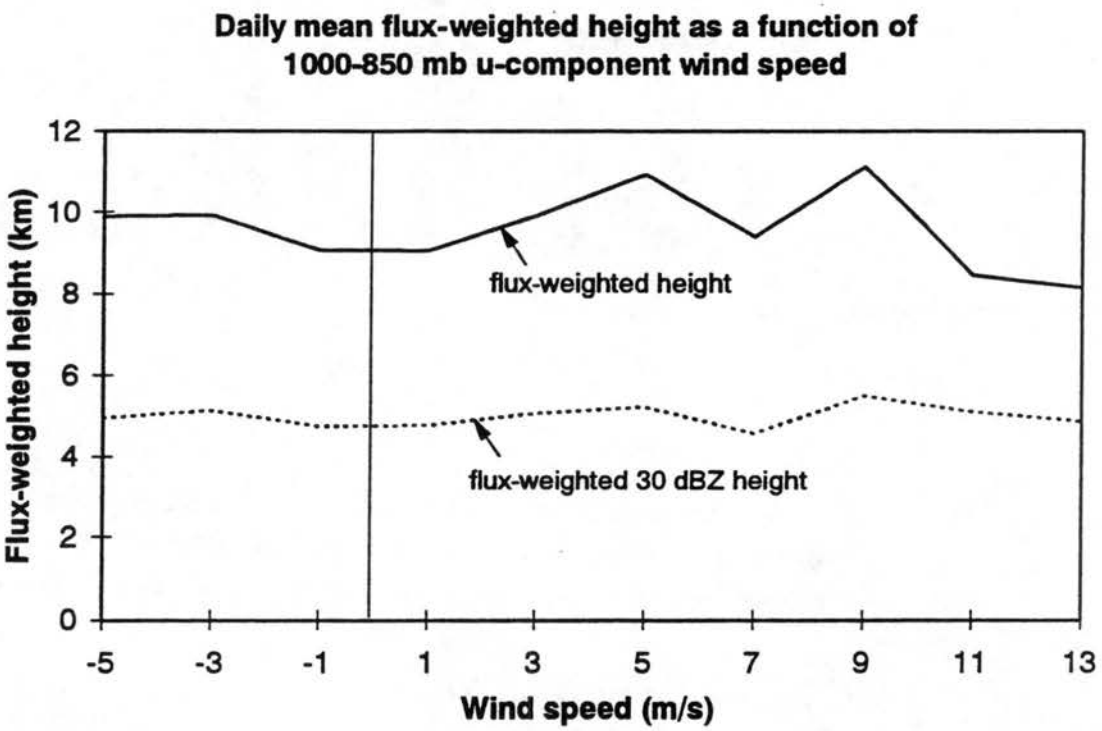

Fig. 4.11 Variation of daily mean rainflux-weighted grid column height and 30 dBZ contour height as a function of mean 1000-850 mb zonal wind speed.

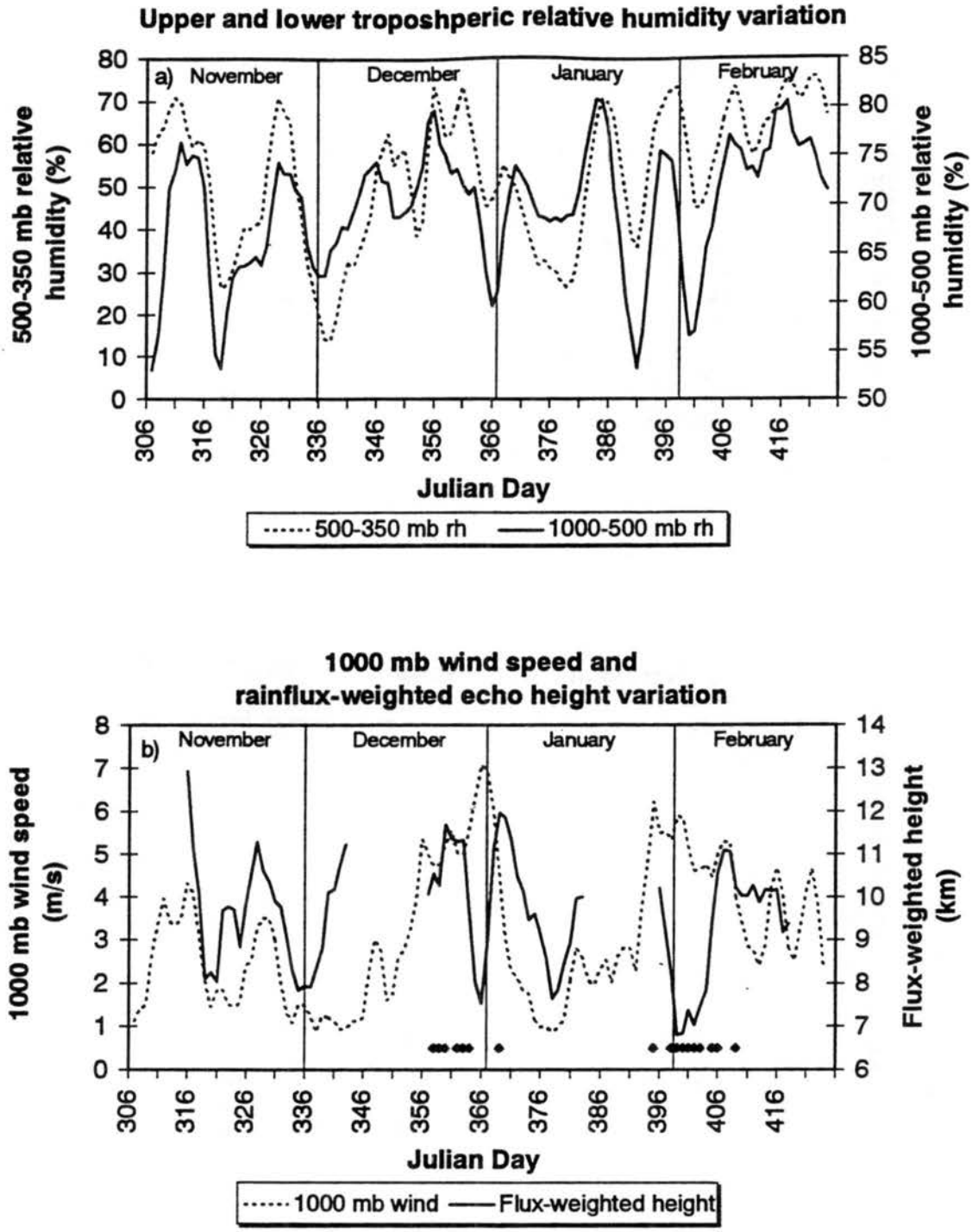

Fig. 4.12 Time series of a) upper (500-350 mb) and lower (1000-500 mb) tropospheric relative humidity and b) 1000 mb wind speed and rainflux-weighted convective grid column height during the COARE IOP.

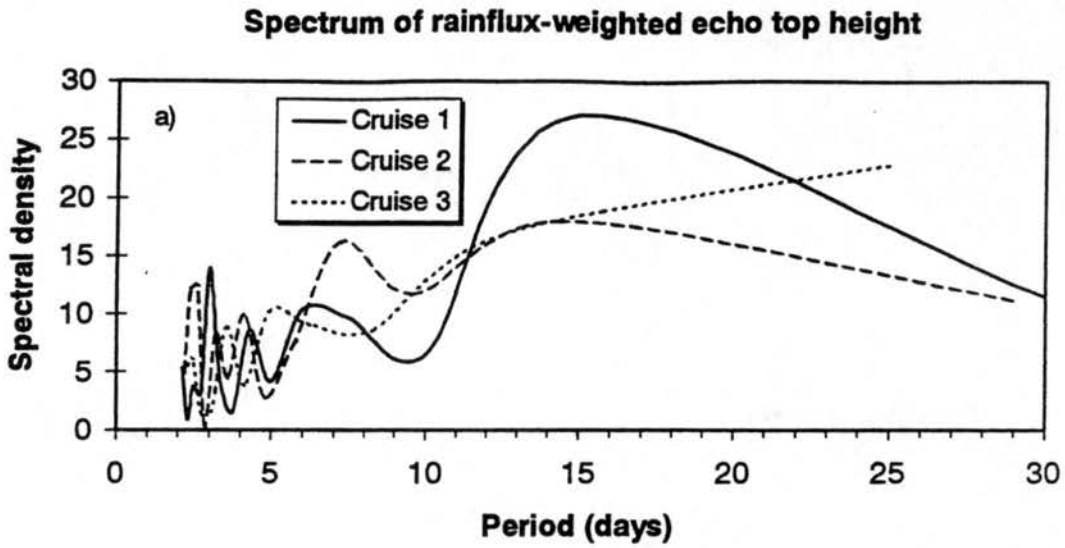

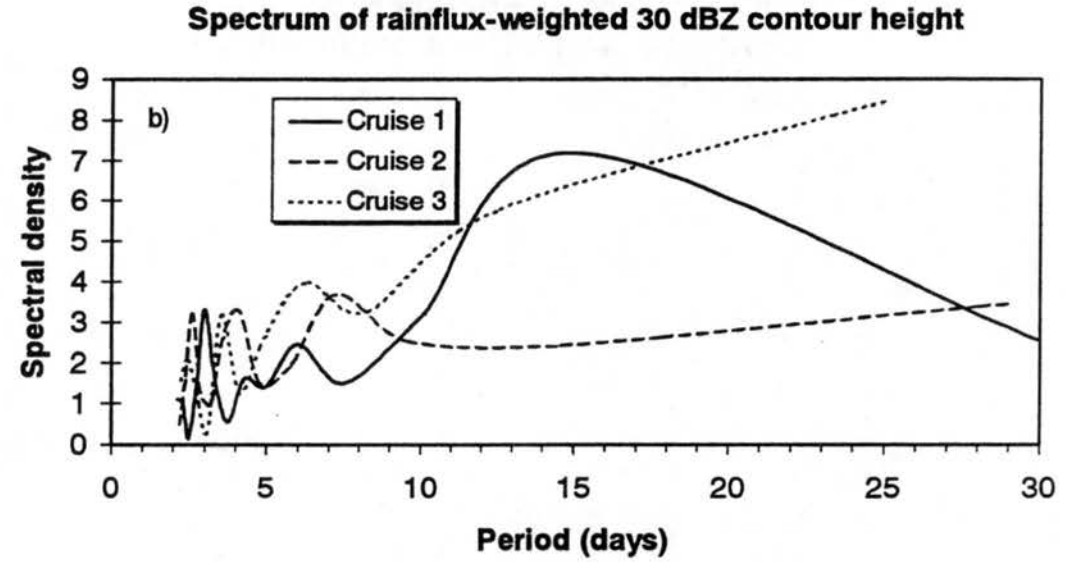

Fig. 4.13 Spectrum of a) daily mean rainflux-weighted convective grid column heights and b) 30 dBZ contour heights for each cruise.

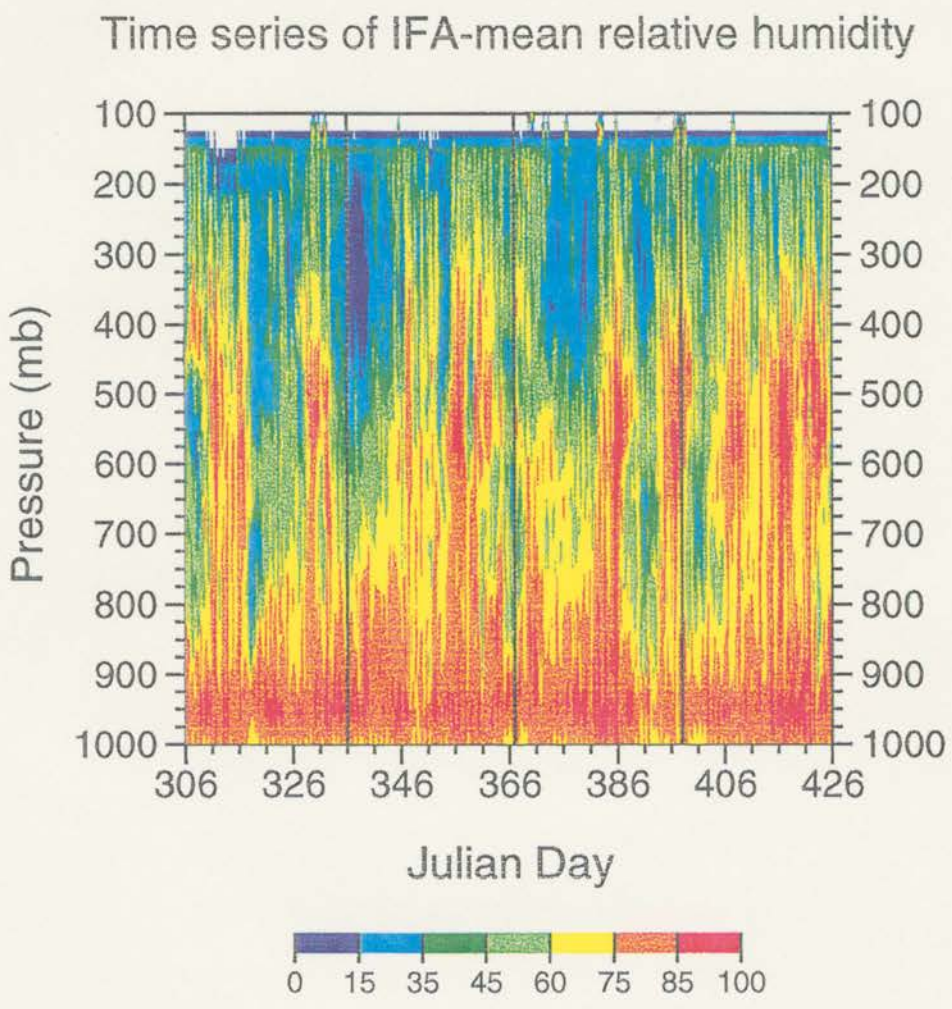

Fig. 4.14 Time height cross section of tropospheric relative humidity during COARE IOP. Temporal resolution is every 6 hours.

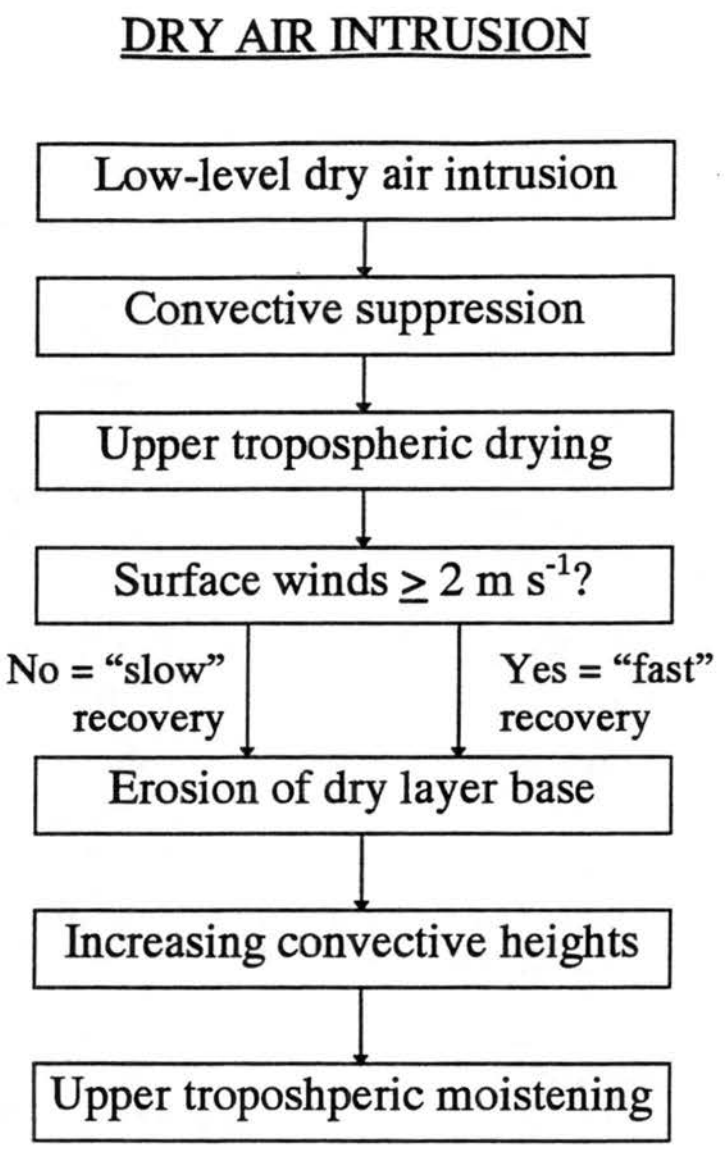

Fig. 4.15 Sequence of event during tropospheric drying and moistening associated with a low-level dry air intrusion.

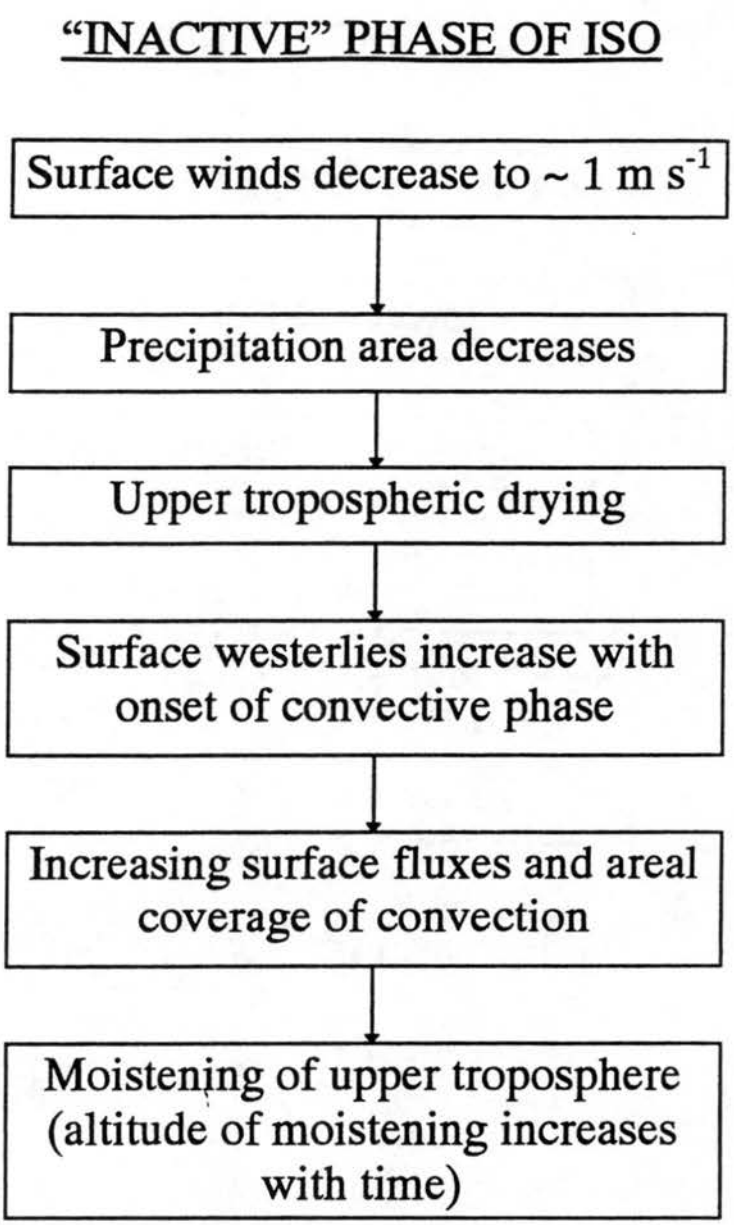

Fig. 4.16 As in Fig. 4.15, but for the ISO "inactive" phase.

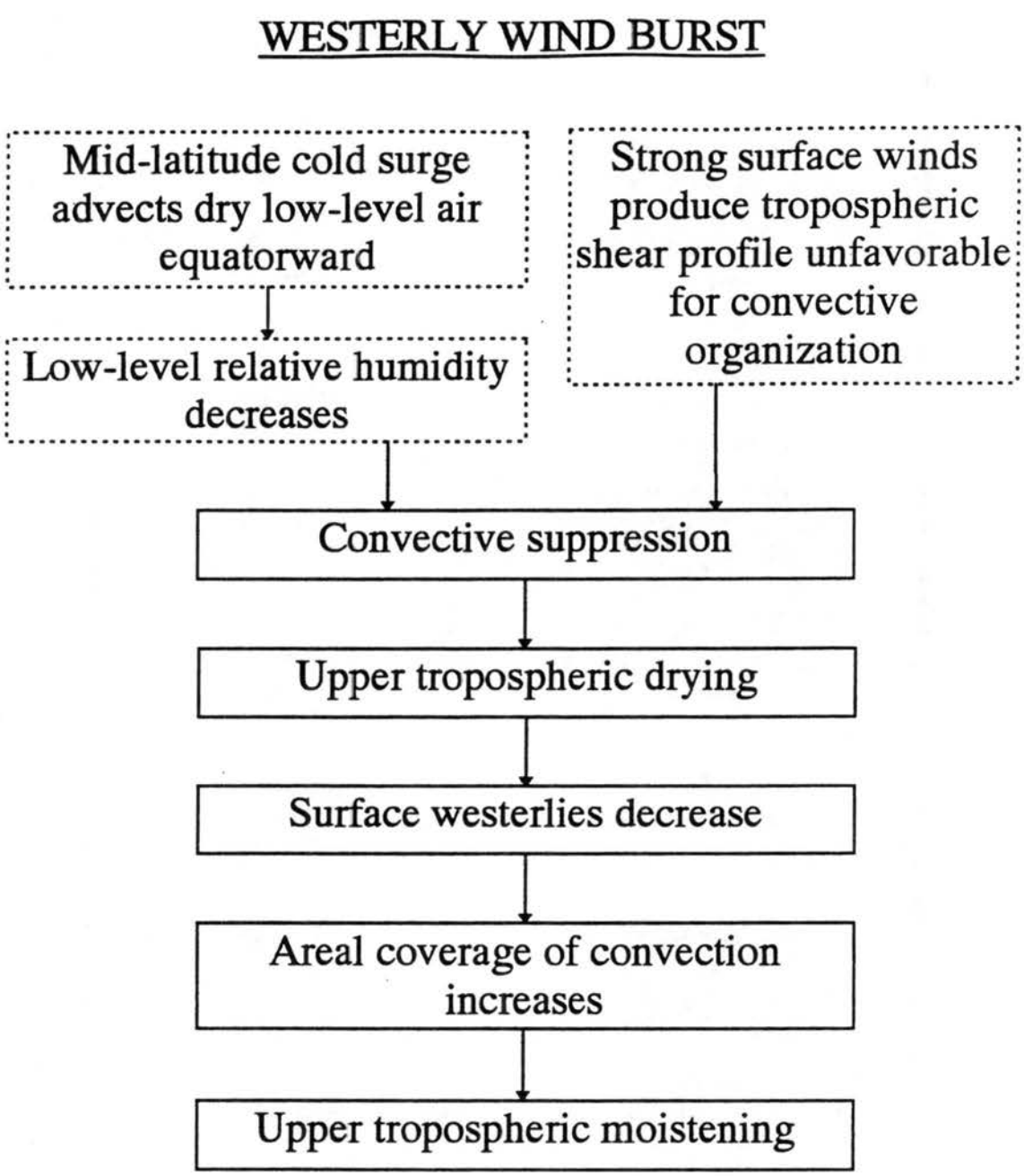

Fig. 4.17 As in Fig. 4.15, but for a WWB event. Drying associated with WWBs may originate with either or both of the events in the dashed-outlined boxes.

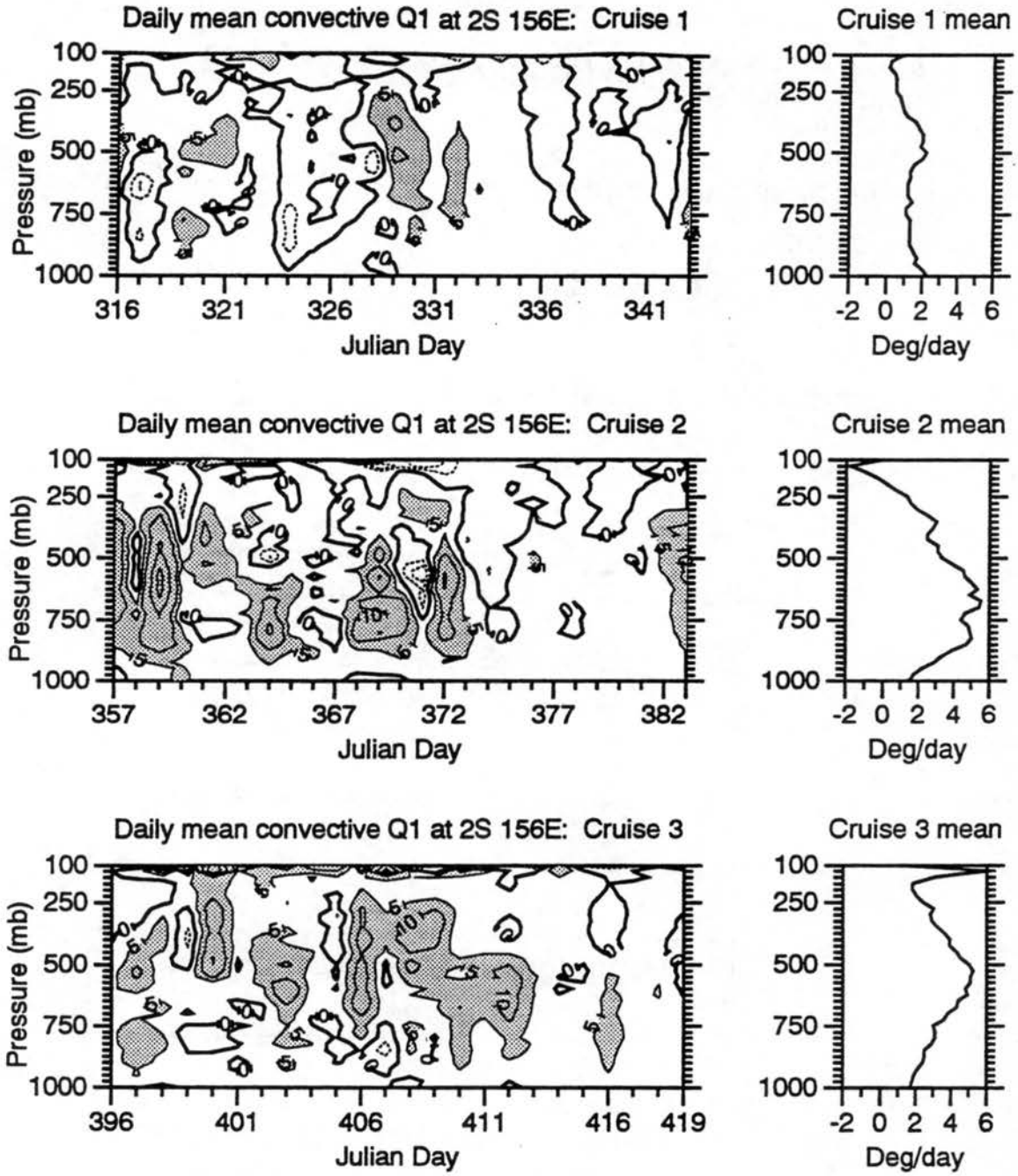

Fig. 4.18 Time series of convective diabatic heating (Q_{1c}) profiles (left panels) and mean Q_{1c} profiles averaged over each cruise. Heating rates are in °C day^{-1} and are contoured at -20, -10, -5, 0, 5, 10, 20, and 30 °C day^{-1}. The 0°C day^{-1} contour is drawn with a heavier line and heating rates $\geq$ 5°C day^{-1} are shaded.

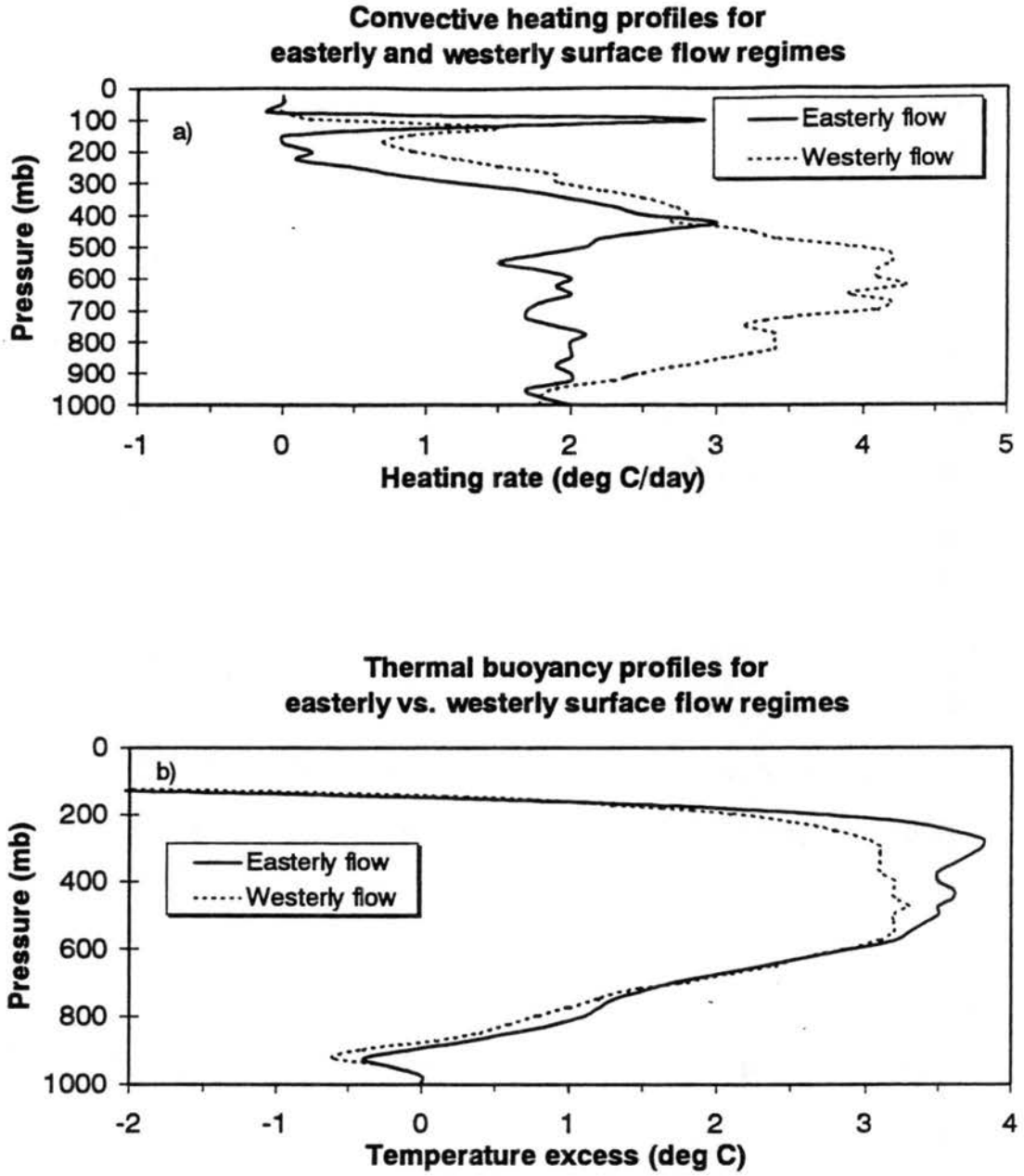

Fig. 4.19 Vertical profile of a) convective heating (Q_{1c}) and b) thermal buoyancy for easterly and westerly surface flow regimes. Q_{1c} profiles are not normalized by rainfall rate.

Chapter 5

DISCUSSION AND CONCLUSIONS

In Sections 1 and 2 of this chapter, results presented in Chapters 3 and 4 are discussed in terms of their implications for TRMM and in terms of controls of convective activity in a potentially buoyant environment, respectively. Potential avenues of future research are discussed in Section 3, and a summary is given in Section 4.

5.1 Implications for TRMM

5.1.1 Convective feature size vs. resolution of TRMM payload

One of the primary techniques for estimating rainfall from the TRMM satellite will be via the interpretation of passive microwave brightness temperatures from five different microwave frequencies. The TRMM Microwave Imager (TMI) will measure upwelling microwave radiation at 10.65, 19.35, 21.3, 37.0, and 85.5 GHz at vertical and horizontal polarizations for all but the 21.3 GHz channel. The half-power beamwidth footprints of these channels are elliptically shaped and increase in size with decreasing frequency, ranging from 7.2 km at 85.5 GHz to 63.2 km at 10.65 GHz (major axis dimension). Because rainfall retrievals based on emission techniques have been proven effective over the ocean, which is a weak and nearly constant emitter at microwave wavelengths (i.e., Wilheit *et al.*, 1977; Spencer *et al.*, 1989), data from the two emission channels (10.65 and 19.35 GHz) will be the primary input for retrieval algorithms during TRMM.

For a beam completely filled with precipitating cloud, brightness temperatures at these two lowest frequency channels are directly related to the mass of water below the freezing level, and therefore appear to be good indicators of rainfall reaching the surface. However, the large surface

footprints of these two channels introduce two types of beam-filling problems into the rainfall retrieval process. The first of these problems arises when a footprint is only partially filled with precipitation and the radiatively cold ocean background will reduce that pixels brightness temperature. This problem should be particularly acute during the inactive phases of the MJO where precipitation is most often characterized by isolated individual cells with dimensions usually smaller than the emission channel footprints (i.e., Rickenbach, 1995).

The second type of beam filling problem that arises occurs when a footprint is completely filled with precipitation, but it is a mix of both convective and stratiform types. Since the ultimate goal of TRMM is to infer diabatic heating profiles, it will be necessary to estimate the relative amounts of convective and stratiform precipitation. To investigate what percentage of convective rainfall may be resolved by the TMI, Figs. 3.28 and 3.29 were modified and are presented in Fig. 5.1. This figure shows the fraction of convective rainfall produced by features with different vertical structure characteristics (dotted lines) and the equivalent mean feature diameter as a function of vertical structure characteristic (solid lines). The contours have been chosen to correspond to the mean resolution of TMI footprints at nadir. As the dotted lines indicate, most of the convective rainfall falls from features that are large enough to be resolved by 19 GHz channel (mean resolution 24.4 km), although much of the convective precipitation is associated with features smaller than this. Furthermore, it is important to note that *precipitation identified as convective, based on emission channel brightness temperatures, will be biased toward the deeper and more intense convection*, which could result in artificially increasing the level of inferred maximum convective heating.

Table 5.1 summarizes the resolution characteristics of the TMI and the percentages of convective rainfall that can be resolved by each channel. It should be noted that these figures actually represent an upper limit to the fraction of resolvable convective rainfall, since large convective features are often long thin lines and, even though their equivalent diameters are large, they still may not completely fill the footprint. For each cruise of the R/V Vickers, only about two thirds of the convective rainfall would have been resolved by the TMI. The results presented in Table 5.1 suggest that higher

frequency channels should be used to improve the accuracy of convective/stratiform rainfall estimates over that which could be obtained from the emission channels alone. Heymsfield and Fulton (1994) have demonstrated that the difference between horizontally and vertically polarized brightness temperatures at 85.5 GHz tend to increase in regions characterized by stratiform precipitation and decrease in more convective regions due to a more preferred horizontal orientation of ice particles in stratiform precipitation compared to convective precipitation. The fine resolution of the 85.5 GHz channel combined with its sensitivity to particle orientation could be used to improve the convective and stratiform rainfall contributions. A similar improvement could be accomplished by using the TRMM precipitation radar to identify the fractional footprint area characterized by radar bright band signatures. It should be noted, however, that any improvements gained in better resolving convective features will be limited by the accuracy with which brightness temperatures at these frequencies are related to surface precipitation rates.

Table 5.1 TRMM Microwave Imager (TMI) footprint sizes and the fraction of convective rainfall associated with convective features that are resolved by each channel. *a* is the major axis dimension of the elliptically shaped footprint, while *b* is the minor axis dimension.

TMI Channel (GHz)	$(a + b)/2$ (km)	Cruise 1	Cruise 2	Cruise 3	IOP mean
10.65	50.75	13.7	4.3	1.0	6.3
19.35	24.4	63.3	69.5	68.8	67.2
21.3	19.05	84.4	88.9	89.2	87.5
37.0	12.85	94.8	99.8	98.6	97.73
85.5	5.8	99.5	99.9	99.3	99.6

5.1.2 TRMM orbital characteristics vs. vertical structure variability time scales

The orbital characteristics of the TRMM satellite are such that a 5×5 degree latitude-longitude grid box will be visited approximately twice at each hour of the day over an approximately one month period. This strategy allows for the study of the diurnal cycle of tropical rainfall from a non-geostationary platform. A drawback to this approach however, is that that large scale convective behavior may vary over time scales significantly shorter than the 1-month diurnal sampling cycle. Furthermore, Lin (1995) has shown that the diurnal cycle of diagnosed vertical motion can shift by 180°

between what he defines as disturbed and suppressed conditions. To the extent that diagnosed vertical motion profiles are related to surface rainfall, this result would suggest that the diurnal cycle of rainfall also shifts between disturbed and suppressed conditions[1]. It may therefore be necessary to stratify the TRMM rainfall data into disturbed and undisturbed regimes to effectively study the diurnal cycle of tropical oceanic convection.

5.2 Convective intensity vs. frequency of intense convection

As was discussed in Chapter 4, there is an apparent inconsistency between the mean convective reflectivity profile, mean thermal buoyancy profile, and contribution to convective rainfall as a function of feature height during Cruise 1. To summarize, the greatest thermal buoyancy and most vertically intense convection is observed during Cruise 1, but this cruise is also characterized by the largest contribution to total convective rainfall by shallow convective features. These two seemingly conflicting statements become less paradoxical when convective activity is considered in terms of its *potential* intensity (i.e., CAPE) and in terms of its *initiation* (or inhibition, as the case may be).

Because mean thermal buoyancy during Cruise 1 is almost no different than the buoyancy profile for days with at least 5 mm of precipitation (Fig. 3.2), the tropical atmosphere during Cruise 1 was, on average, always capable of supporting deep intense convection from a thermodynamic perspective. However, because so much of the convection observed during this cruise was scattered and relatively shallow, it may be concluded that other factors acted to suppress convective development or sufficiently strong "triggering" or forcing mechanisms were not present during this period. One possible limit to convective activity is convective inhibition (CIN), which can prohibit the development of convective activity since it represents an energy barrier that first must be overcome before the reservoir of CAPE can be realized. However, as seen in Fig. 3.2b, mean CIN varied little from one cruise to the next. In addition to CIN—and as was discussed at length in Chapter 4—two types of convective

[1] The diurnal cycle of rainfall was computed for the days that Lin described as disturbed and convective using the MIT radar data. However, because the ship was in port during all but six of the "disturbed" days, the data sample was not large enough to reduce the noise associated with systems propagating into and out of the study area, so a statistically significant average could not be obtained.

inhibitions were often present during Cruise 1. The first type of inhibitor was low-level intrusions of dry subtropical air whose bases were typically located 1.5-2 kilometers above the surface, which generally suppressed the vertical development of convection. The fact that at least a few deep convective cells were always present suggests that surface conditions favorable to deep convective development (i.e., high moisture contents, low-level convergence produced by convective outflows) were still present on highly localized scales, but on average, convection was not able to develop to the extent of fully realizing the available CAPE. Entrainment of the anomalously dry low- to mid-level air was probably the greatest inhibitor to extensive vertical development during these periods, since the entrained air would reduce the moisture content of the rising parcel, as well as the difference between the environmental and parcel potential temperatures, thereby reducing parcel buoyancy.

The second factor that may have limited convective vertical development during Cruise 1 was the unusually light surface winds associated with the inactive phase of the ISO in late November to early December. These light wind regimes are associated with very weak low-level shear (Rickenbach, 1995), which reduces the possibility of developing a favorable feedback between convective outflows and low-level shear for enhancing the vertical development of convection (Rotunno *et al.*, 1988). Therefore, there is greater chance that descending precipitation cores will fall through updraft cores, reducing their updraft strength and thereby limiting convective vertical development. Furthermore, the presence of the trade inversion in the thermal buoyancy plots (Figs. 3.2 and 4.19) is noted at about 800 mb and may play a relatively more important role in suppressing convection during light wind regimes associated with the inactive phase of the ISO as compared to those periods with strong surface winds.

5.3 Directions for future research

5.3.1 Comparisons with GATE convection

The convection observed during COARE occurs over the warmest ocean temperatures on the planet. Determining how these high surface temperatures impact convection, however, remains a difficult task, primarily due to differences in analysis techniques and temporal sampling between this

study and those performed using GATE data. For instance, Cheng and Houze (1979) produced histograms of convective rainfall contributions as a function of *maximum* echo top height, rather than *instantaneous* heights as was done in this study. Furthermore, their analysis is based on only a subset of the GATE data[2], whereas this study utilizes all data at 20-minute resolution. Some of the most meaningful comparisons between COARE and GATE convection would involve the intensity of rainfall and the contribution to total convective area as a function of echo top height for each region. Unfortunately, the only published description of such information for GATE is produced from a single case study (Leary, 1984) based on a manual identification and analysis of convective echo.

With the recent development of automated convective identification algorithms (i.e., Steiner and Houze, 1993; DeMott *et al.*, 1995; Steiner *et al.*, 1995) the GATE data could be reanalyzed using the same methods that were used in this study, thereby allowing meaningful direct comparisons between the two datasets. Such a task was initially explored for inclusion in this study, but was hampered by problems in locating GATE data, determining if the 9-track tapes on which it is stored are still useable, and putting the data into a format suitable for present day interpolation and analysis packages. Despite these obstacles, a re-examination of the GATE radar data is possible and the potential benefits are substantial in terms of assessing how convective structure varies over the globe and in estimating how it may evolve in a global warming scenario.

A second, and potentially more feasible, comparison between COARE and GATE convection could be accomplished by identifying periods during COARE where the large-scale convective controls were similar to those presented in Leary (1984). The convective system analyzed by Leary occurred in the trough of an easterly wave and lasted for approximately 25 hours. Reed and Recker (1971) have described the structure of easterly waves in the western Pacific and their presence was observed during COARE. Although identifying "synoptically similar" periods in the COARE data would involve

[2] Cheng and Houze (1979) tracked only those convective echoes that were present at 1200 UTC for each day during GATE. These echoes were tracked backward and forward in time to ascertain their maximum height and area, but echoes that appeared before or after 1200 UTC were not included in the sample. Therefore, their results may be subject to a diurnal bias.

subjective judgments, a carefully selected group of cases could result in more meaningful comparisons between the two data sets than was possible herein.

5.3.2 Further exploration of the role of dry tongues and convective activity on tropospheric moistening

Because water vapor is an important greenhouse gas, processes that regulate its distribution throughout the atmosphere are of interest in efforts devoted to examining the response of the global circulation to global warming. The relationship of "drying processes" on convective activity and upper tropospheric moistening has been explored qualitatively based on the few instances that such interactions were observed during COARE. Three scenarios describing how these processes interact were proposed, but they are based on only a few observations. One approach to determining how realistic (or possibly unrealistic) these scenarios may be is to model the effects of dry tongues, low surface wind speeds, and WWBs on convective activity and tropospheric moistening with either a mesoscale model or a global scale model driven by observations of temperature, humidity, and winds.

5.3.3 Verification and improvement of passive microwave retrieval algorithms

The descriptions of convective clouds, their rainfall rates, and temporal variability as described in this study offer a unique "ground truth" database for the development and improvement of rainfall retrieval algorithms based on the passive microwave inversion problem. Algorithms that may particularly benefit from this type of information are those that return estimates of both surface rainfall rate *and* the vertical structure of precipitation. An example of such an algorithm is that described by Kummerow and Giglio (1994), which estimates the vertical structure of hydrometeors by choosing from a database of likely vertical structures that which produces multispectral brightness temperatures closest to those observed. The representativeness of the profiles chosen by the algorithm could be tested by computing radar reflectivities based on the selected hydrometeor types and concentrations followed by comparison to the observed profiles. Alternatively, the relationship between vertical reflectivity structure on upwelling microwave brightness temperatures could also be studied in an effort to quantify the impact

of large ice and/or supercooled liquid water above the freezing level on scattering at higher microwave frequencies.

5.4 Summary

Tropical convection is an important component of the general circulation due to its role in driving large scale circulations which redistribute energy received at the equator to higher latitudes. The behavior of these large scale circulations is sensitive to the vertical distribution of diabatic heating produced by mesoscale precipitation systems, which are driven by precipitation formation processes. TRMM has been designed to study the frequency and variability of tropical precipitation, as well as to infer the shape of the diabatic heating profile resulting from the rainfall. Background and ground-truth information for TRMM has been drawn from several tropical locations, one of which is the recently completed TOGA COARE. This study used radar data collected during COARE to address two main goals: 1) to determine the characteristic distributions of convective echo during COARE and their variability over time, and 2) to relate observed variations of convective vertical structure to larger scale environmental variables. This study focuses solely on convective echo rather than both convective and stratiform since more than half of tropical precipitation falls from convective towers, and since the production of stratiform rainfall is often linked to interactions of convective towers with their environment.

TOGA COARE was conducted in the western Pacific warm pool region and was designed to identify processes which couple the tropical ocean and atmosphere and organize convection, understand the oceanic response to buoyancy and wind-stress forcing, and understand multiple-scale interactions that extend the influence of the warm pool region to other parts of the globe. The western Pacific warm pool is characterized by sea surface temperatures in excess of 28°C and annual rainfall amounts in excess of 4 m. Modulation of convective activity occurs on temporal scales as long as the 30-60 day intraseasonal oscillation, to 4-5 day easterly waves, to 2-day and diurnal oscillations.

During the COARE intensive observing period (November 1992 through February 1993), three passages of the convective/westerly wind burst phases of the ISO were sampled. More frequent observations of shorter time scale disturbances were also encountered. The R/V Vickers, equipped with the continuously operating MIT 5-cm Doppler radar, was deployed for three approximately 30-day cruises during the IOP during which it recorded full-volume radar scans at 10-minute resolution. Using every other full radar volume, the data were interpolated to a Cartesian grid and partitioned into convective and stratiform components using an automated partitioning algorithm. A database of individual convective features (which may be composed of one or more convective cells) was constructed and includes information on feature height, area, mean rainfall rate, 30 dBZ contour height, and rain volume. Variations in the distributions of convective properties were compared to environmental conditions observed as determined by the interpolated TOGA COARE sounding data.

Consistent with previous studies, distributions of echo top height are approximately lognormally distributed. On average, taller and larger (in an areal sense) features tend to rain harder than shorter, smaller features, although the range of rainfall rates observed for features of a given height is quite large. Rainfall rate varied less when features were characterized by 30 dBZ contour height, suggesting that this variable would provide a better estimate of surface rainfall rate than cloud top height.

The most intense convection—as observed by mean convective reflectivity profiles—occurred in environments with the greatest thermal buoyancy experienced by parcels lifted from the surface. These conditions were most often present during periods of easterly flow, which were most often associated with the "inactive" phase of the ISO. However, these periods were also often characterized by strong inhibitors to convective vertical development, such as subtropical dry air intrusions, or low surface wind speed regimes. The result of these two competing controls on convective development is vertically intense convection during relatively infrequent periods of widespread rainfall, but a large contribution to convective rainfall by shallow convective elements. In contrast, convection associated with the convective portion of the ISO was vertically less intense than that occurring in easterly flow and was also associated with smaller thermal buoyancy values. The more frequent and widespread rainfall

characteristic of these regimes, however, suggests that there were few inhibitors to convective initiation and development during this regime.

Convective heating profiles were computed using a combination of radar-derived rainfall information and sounding-derived total (convective plus mesoscale) heating profiles. The results show that the vertical location of maximum convective heating varied in a manner consistent with the variations in vertical reflectivity and thermal buoyancy profiles. Namely, the less vertically intense convection of Cruise 2 was associated with a lower convective heating maximum than was observed during Cruises 1 and 3. This result supports the assertions of Zipser and LeMone (1980) that convection with weaker updraft structures produces most of its rainwater—and therefore heating—via condensation and collision-coalescence below the freezing level. The more vigorous updrafts that were occasionally attained during Cruise 1 lofted greater amounts of supercooled liquid water above the freezing level thereby increasing the heating in that region as water drops froze and vapor deposited onto existing ice particles.

These results collectively point to other possible avenues of research, including a rigorous comparison of convective characteristics between the COARE and GATE regions, modeling studies of the influence of low-level dry air on convective activity and its relation to tropospheric drying, and testing and refinement of passive microwave rainfall retrieval algorithms.

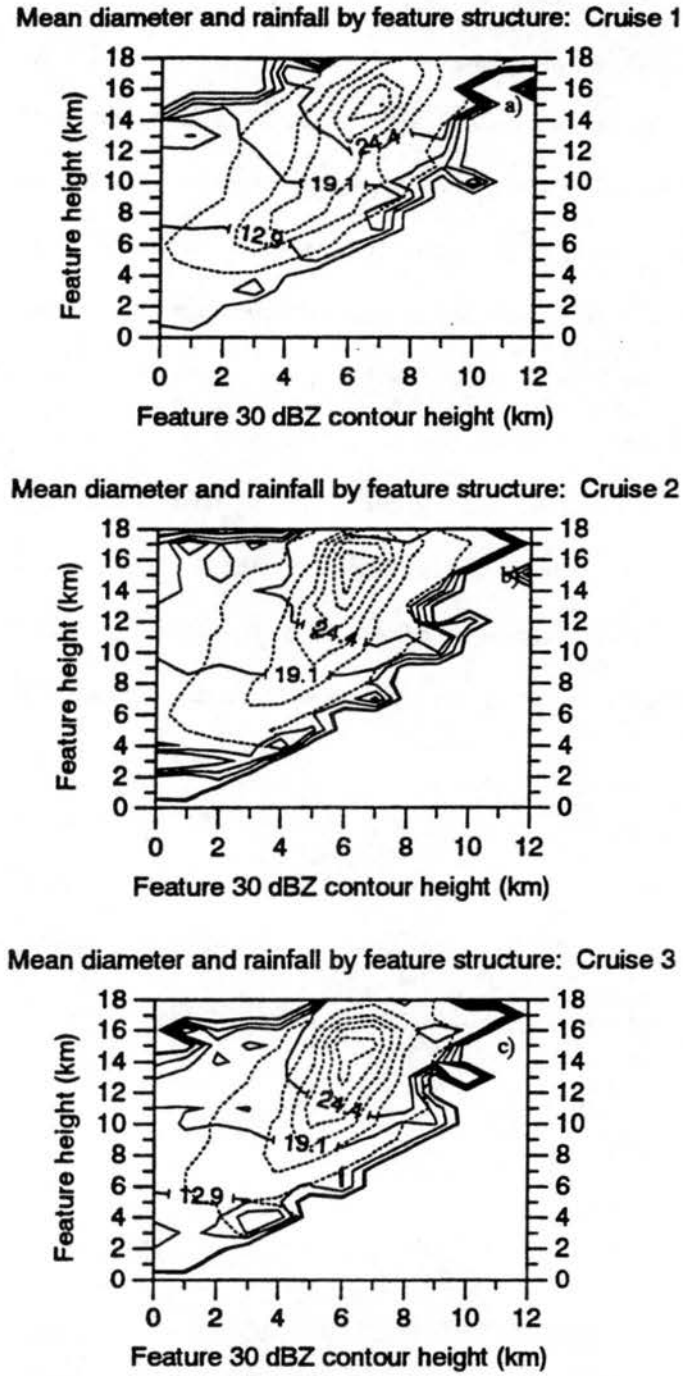

Fig. 5.1 Distribution of the relative contribution to convective rainfall (dotted lines) and mean equivalent feature diameter (solid lines) as a function of feature height and 30 dBZ contour height. Relative rainfall frequencies are contoured at 0.1, 1, 2, 3, 4, 5, and 6%. Mean equivalent diameter is contour values are 50.8, 24.4, 19.1, 12.9, and 5.8 km, which respectively correspond to the mean footprint size of the 10.65, 19.35, 21.3, 37.0, and 85.5 GHz channels of the TMI.

REFERENCES

Ackerman, T. P., K.-N, Louis, F. P. J. Valero, and L. Pfister, 1988: Heating rates in tropical anvils. *J. Atmos. Sci.*, **45**, 1606-1623.

Atlas, D. and T. L. Bell, 1992: The relation of radar to cloud area-time integrals and implications for rain measurements from space. *Mon. Wea. Rev.*, **120**, 1977-2008.

Barnes, S. L., 1964: A technique for maximizing details in numerical weather map analysis. *J. Appl. Meteor.*, **3**, 396-409.

Barnes, S. L., 1973: Mesoscale objective map analysis using weighted time-series observations. NOAA Tech Memo. ERL NSSL-62, Norman, OK, 60 pp.

Byers, H. R. and R. R. Braham, 1949: The thunderstorm project. US Weather Bureau, US Dept. of Commerce, Washington, DC, 287 pp. [NTIS PB234515].

Chen, S. S., R. A. Houze, Jr., and B. E. Mapes, 1995: Multiscale variability of deep convection in relation to large-scale circulation in TOGA COARE. Submitted to *J. Atmos. Sci.*

Cheng, C.-P., and R. A. Houze, Jr., 1979: The distribution of convective and mesoscale precipitation in GATE radar echo patterns. *Mon. Wea. Rev.*, **107**, 1370-1381.

Churchill, D. D. and R. A. Houze, Jr., 1984: Development and structure of winter monsoon cloud clusters on 10 December 1978. *J. Atmos. Sci.*, **41**, 933-960.

Cifelli, R., S. A. Rutledge, D. J. Bocippio, and T. Matejka, 1996: Horizontal divergence and vertical velocity retrievals from Doppler radar and wind profiler observations. *Accepted to J. Atmos. Ocean. Tech.*

Cox, S. K. and K. T. Griffith, 1979: Estimate of radiative divergence during Phase III of the GARP Atlantic Tropical Experiment: Part II. Analysis of the Phase III results. *J. Atmos. Sci.*, **36**, 586-601.

Cunning, J. B., 1988: Taiwan Area Mesoscale Experiment: Daily operations summary. NCAR Tech. Note, NCAR/TN-305+STR, 361 pp.

DeMaria, M., 1985: Linear response of a stratified tropical atmosphere to convective forcing. *J. Atmos. Sci.*, **42**, 1944-1959.

DeMott, C. A., R. Cifelli, and S. A. Rutledge, 1995: An improved method for partitioning radar data into convective and stratiform components. Preprint volume, *27th Conf. on Radar Meteorology*, Amer. Meteor. Soc., Vail, Colorado, 233-236.

Doneaud, A. A., S. I. Niscov, D. L. Priegnitz, and P. L. Smith, 1984: The area-time integral as an indicator for convective rainf volumes. *J. Climate Appl. Meteor.*, **23**, 555-561.

Gill, A. E., 1982: *Atmosphere-Ocean Dynamics.* Academic Press. 662 pp.

Gray, W. M., and R. W. Jacobson, Jr., 1977: Diurnal variation of deep cumulus convection. *Mon. Wea. Rev.*, **105**, 1171-1188.

Haertel, P. T. and R. H. Johnson, 1996: Two-day disturbances in the equatorial western Pacific. Submitted to *Q. J. R. Meteorol. Soc.*

Hayes, S. P., L. J. Mangum, J. Picaut, A. Sumi, and K. Takeuchi, 1991: TOGA-TAO: A moored array for real-time measurements in the tropical Pacific Ocean. *Bull. Amer. Meteor.*, **72**, 339-347.

Hartman, D. L., H. H. Hendon, and R. A. Houze, Jr., 1984: Some implications of the mesoscale circulations in tropical cloud clusters for large-scale dynamics and climate. *J. Atmos. Sci.*, **41**, 113-121.

Hendon, H. H. and B. Liebmann, 1991: The structure and annual variation of antisymmetric fluctuations of tropical convection and their association with Rossby-gravity waves. *J. Atmos. Sci.*, **48**, 2127-2140.

Heymsfield, G. M. and R. Fulton, 1994: Passive microwave and infrared structure of mesoscale convective systems. *Meteor. and Atmos. Phsy.*

Holland, G. J., J. L. McBride, R. K. Smith, D. Jasper, and T. D. Keenan, 1986: The BMRC Australian Monsoon Experiment: AMEX. *Bull. Amer. Meteor.*, **67**, 1466-1472.

Houze, R. A. Jr., 1982: Cloud clusters and large-scale vertical motions in the tropics. *J. Meteorol. Soc. Jap.*, **60**, 396-410.

Houze, R. A. Jr., 1989: Observed structure of mesoscale convectiv esystems and implications for large-scale heating. *Q. J. R. Meteorol. Soc.*, **115**, 425-461.

Houze, R. A., Jr., and C.-P. Cheng, 1977: Radar characteristics of tropical convection observed during GATE: Mean properties and trends over the summer season. *Mon. Wea. Rev.*, **105**, 964-980.

Hudlow, M. D., 1979: Mean rainfall patterns for the three phases of GATE. *J. Appl. Meteor.*, **18**, 1656-1669.

Johnson, R. H., 1984: Partitioning tropical heat and moisture budgets into cumulus and mesoscale components: Implications for cumulus parameterization. *Mon. Wea. Rev.*, **112**, 1590-1601.

Johnson, R. H., P. E. Ciesielski, and K. A. Hart, 1996: Tropical inversions near the 0°C level. Accepted to *J. Atmos. Sci.*

Johnson, R. H., and G. S. Young, 1983: Heat and moisture budgets of tropical mesoscale clouds. *J. Atmos. Sci.*, **40**, 2138-2147.

Jorgensen, D. P. and M. A. LeMone, 1988: Taiwan Area Mesoscale Experiment: P-3 aircraft operations summary. NCAR Tech. Note, NCAR/TN-305+STR, 71 pp.

Jorgensen, D. P. and M. A. LeMone, 1989: Vertical velocity characteristics of oceanic convection. *J. Atmos. Sci.*, **46**, 621-640.

Kummerow, C., and L. Giglio, 1994: A passive microwave technique for estimating rainfall and vertical structure information from space. Part I: Algorithm description. *J. Appl. Meteor.*, **33**, 3-18.

Lau, K.-M., and L. Peng, 1987: Origin of low-frequency (intraseasonal) oscillations in the tropical atmosphere. Part I: Basic theory. *J. Atmos. Sci.*, **44**, 950-972.

Lau, K.-M., L. Peng, C. H. Sui, and T. Nagazawa, 1989: Dynamics of super cloud clusters, westerly wind bursts, 30–60 day oscillations and ENSO: A unified view. *J. Meteor. Soc. Japan*, **67**, 205-219.

Leary, C. A., 1984: Precipitation structure of the cloud clusters in a tropical easterly wave. *Mon. Wea. Rev.*, **112**, 313-325.

Leary, C. A., and R. A. Houze, Jr., 1979a: The structure and evolution of convection in a tropical cloud cluster. *J. Atmos. Sci.*, **36**, 437-457.

Leary, C. A., and R. A. Houze, Jr., 1979b: Melting and evaporation of hydrometeors in precipitation from the anvil clouds of deep tropical convection. *J. Atmos. Sci.*, **36**, 669-679.

LeMone, M. A., and E. J. Zipser, 1980: Cumulonimbus vertical velocity events in GATE. Part I: Diameter, intensity and mass flux. *J. Atmos. Sci.*, **37**, 2444-2457.

Lily, D. K., 1988: Cirrus outflow dynamics. *J. Atmos. Sci.*, **45**, 1594-1979.

Lin, X., 1995: Diurnal variations of convection over the western Pacific warm pool region during the TOGA COARE IOP. Preprints: *21st Conf. on Hurricanes and Tropical Meteorology*. Miami, Florida. Amer. Meteor. Soc., 91-93

Lin, X. and R. H. Johnson, 1996a: Kinematic and thermodynamic characteristics of the flow over the western Pacific warm pool during TOGA COARE. Submitted to *J. Atmos. Sci.*

Lin, X. and R. H. Johnson, 1996b: Heating, moistening and rainfall analysis over the western Pacific warm pool during TOGA COARE. Submitted to *J. Atmos. Sci.*

López, R. E., 1977: The lognormal distribution and cumulus cloud populations. *Mon. Wea. Rev.*, **105**, 865-872.

Lucas, C., E. J. Zipser, and M. A. LeMone, 1994: Vertical velocity in oceanic convection off tropical Australia. *J. Atmos. Sci.*, **51**, 3183-3193.

Madden, R. A. and P. R. Julian, 1971: Description of a 40-50 day oscillation in the zonal wind in the tropical Pacific. *J. Atmos. Sci.*, **28**, 702-708.

Madden, R. A. and P. R. Julian, 1972: Description of global-scale circulation cells in the tropics with a 40-50 day period. *J. Atmos. Sci.*, **29**, 1109-1123.

Madden, R. A. and P. R. Julian, 1994: Observations of the 40–50-day tropical oscillation—A review. *Mon. Wea. Rev.*, **122**, 814-837.

Mapes, B. E., 1993: Gregarious tropical convection. *J. Atmos. Sci.*, **50**, 2026-2037.

Mapes, B. E. and R. A. Houze, Jr., 1993: Cloud clusters and superclusters over the oceanic warm pool. *Mon. Wea. Rev.*, **121**, 1398-1415.

Mapes, B. E. and P. Zuidema, 1996: Radiative-dynamical consequences of dry tongues in the tropical troposphere. Accepted to *J. Atmos. Sci.*

Matsuno, T., 1966: Quasi-geostrophic motions in the equatorial area. *J. Meteor Soc. Japan*, **44**, 25-43.

Nakazawa, T., 1986: Intraseasonal variations of OLR in the tropics during the FGGE year. *J. Meteor. Soc. Japan*, **64**, 17-34.

Nakazawa, T., 1988: Tropical super clusters within intraseasonal variations over the western Pacific. *J. Meteor. Soc. Japan*, **66**, 823-839.

Numaguti, A., R. Oki, K. Nakamura, K. Tsuboki, N. Misawa, T. Asai, and Y.-M. Kodama, 1995: 4–5-day-period variation on low-level dry air observed in the equatorial western Pacific during the TOGA COARE IOP. *J. Meteor. Soc. Japan*, **73**, 267-290.

O'Brien, J. J., 1970: Alternative solutions to the classical vertical velocity problem. *J. Appl. Meteor.*, **9**, 197-203.

Olson, W. S., 1989: Physical retrieval of rainfall rates over the ocean by multispectral microwave radiometry: Application to tropical cyclones. *J. Geophys. Res.*, **94**, 2267-2280.

Parson, D., W. Dabberdt, H. Cole, T. Hock, C. Martin, A.-L. Barret, E. Miller, M. Spowart, M. Howard, W. Ecklund, D. Carter, K. Gage, and J. Wilson, 1994: The integrated sounding system: description and preliminary observations from TOGA COARE. *Bull. Amer. Meteor. Soc.*, **75**, 553-567.

Payne, S. W. and M. M. McGarry, 1977: The relationship of satellite inferred convective activity to easterly waves over West Africa and the adjacent ocean during Phase III of GATE. *Mon. Wea. Rev.*, **105**, 413-420.

Petersen, W. A., S. A. Rutledge, and R. E. Orville, 1996: Cloud-to-ground lightning observations from TOGA COARE: Selected results and lightning location algorithms. Accepted to *Mon. Wea. Rev.*

Peixoto, J. P. and A. H. Oort, 1992: *Physics of Climate.* American Institute of Physics. New York, NY. 520 pp.

Reed, R. J. and E. E. Recker, 1971: Structure and properties of synoptic-scale wave disturbances in the equatorial western Pacific. *J. Atmos. Sci.*, **28**, 1117-1133.

Reeves, R. W., C. F. Ropelewski, and M. D. Hudlow, 1979: Relationships between large-scale motion and convective precipitation during GATE. *Mon. Wea. Rev.*, **107**, 1154-1168.

Rickenbach, T., 1995: Rainfall production from the spectrum of convection observed by shipboard radar during TOGA COARE. Preprints: *21st Conference on hurricanes and tropic meteorology.* Miami, FL, Amer. Meteor. Soc., 116-118.

Rotunno, R., J. B. Klemp, and M. L. Weisman, 1988: A theory for strong, long-lived squall lines. *J. Atmos. Sci.*, **45**, 463-485.

Rutledge, S. A., R. Cifelli, C. DeMott, W. Petersen, T. Rickenbach, J. Lutz, R. Bowie, M. Strong, E. Williams, 1993: The shipboard deployment of the MIT C-band radar during TOGA COARE. Preprint volume, *26th Intl. Conf. on Radar Meteor.*, Amer. Met. Soc., Norman, Oklahoma, 371-373.

Rutledge, S. A. and R. A. Houze, Jr., 1987: A diagnostic modeling study of the trailing stratiform region of a midlatitude squall line. *J. Atmos. Sci.*, **44**, 2640-2656.

Rutledge, S. A., E. R. Williams, and T. D. Keenan, 1992: The down under doppler and electricity experiment (DUNDEE): Overview and preliminary results. *Bull. Amer. Meteor. Soc.*, **73**, 3-16.

Shin, K.-S. and G. R. North, 1987: Sampling error study for rainfall estimates by satellite using a stochastic model. Preprint volume, *Tenth Conference on Probability and Statistics in Atmospheric Science.* Amer. Met. Soc., Edmonton, Alberta, Canada

Sheu, R.-S. and G. Liu, 1995: Atmospheric humidity variations associated with westerly wind bursts during Tropical Ocean Global Atmosphere (TOGA) Couple Ocean Atmosphere Response Experiment (COARE). *J. Geophys. Res.* **100**, 25759-25768.

Simpson, J., R. F. Adler, and G. R. North, 1988: A proposed tropical rainfall measuring mission (TRMM) satellite. *Bull. Amer. Meteor. Soc.*, **69**, 278-295.

Smith, E. A., A. Mugnai, H. J. Cooper, G. J. Tripoli, and X. Xiang, 1992: Foundations for statistical-physical precipitation retrieval from passive microwave satellite measurements. Part I: Brightness-temperature properties of a time-dependent cloud-radiation model. *J. Appl. Meteor.*, **31**, 506-531.

Song, J.-L. and W. M. Frank, 1983: Relationships between deep convection and large-scale processes during GATE. *Mon. Wea. Rev.*, **111**, 2145-2160.

Spencer, R. W., H. M. Goodman, and R. E. Hood, 1989: Precipitation retrieval over land and ocean with the SSM/I: Identification and characteristics of the scattering signal. *J. Atmos. Ocean. Tech.*, **6**, 254-273.

Steiner, M. and R. A. Houze, Jr., 1993: Three-dimensional validation at TRMM ground truth sites: Some early results from Darwin, Australia. Preprints, *26th Int. Conf. on Radar Meteorology,* Norman, OK, Amer. Meteor. Soc., 417-420.

Steiner, M., R. A. Houze, Jr., and S. E. Yuter, 1995: Climatological characterization of three-dimensional storm structure from operational radar and rain gauge data. *J. Appl. Meteor.*, **34**, 1978-2007.

Sui, C.-H. and K.-M. Lau, 1992: Multiscale phenomena in the tropical atmosphere over the western Pacific. *Mon. Wea. Rev.*, **120**, 407-430.

Szoke, E. J. and E. J. Zipser, 1986: A radar study of convective cells in mesoscale systems in GATE. Part II: Life cycles of convective cells. *J. Atmos. Sci.*, **43**, 199-218.

Szoke, E. J., E. J. Zipser, and D. P. Jorgensen, 1986: A radar study of convective cells in mesoscale systems in GATE. Part I: Vertical profile statistics and comparison with hurricanes. *J. Atmos. Sci.*, **43**, 181-197.

Takayabu, Y. N., K.-M. Lau, and C.-H. Sui, 1996: Observation of quasi two-day wave during TOGA COARE. Submitted to *Mon. Wea. Rev.*

Takayabu, Y. N. and T. Nitta, 1993: 3–5-day-period disturbances coupled with convection over the tropical Pacific ocean. *J. Meteor. Soc. Japan*, **71**, 221-246.

Thiele, O. W., D. A. Short, J. C. Gerlach, D. B. Wolff, M. J. McPhaden, and J. C. Wilkerson, 1994: TOGA COARE ocean precipitation morphology. Preprints: *6th Conference on Climate Variations*, Nashville, TN, Amer. Meteor. Soc., J72-J75.

Thompson, R. M., S. W. Payne, E. E. Recker, and R. J. Reed, 1979: Structure and properties of synoptic-scale wave disturbances in the intertropical convergence zone of the eastern Atlantic. *J. Atmos. Sci.*, **36**, 53-72.

Udelhofen, P. M. and D. L. Hartmann, 1995: Influence of tropical cloud systems on the relative humidity in the upper troposphere. *J. Geophys. Res.* **100**, 7423-7440.

Ushiyama, T., S. Sath, and K. Takeuchi, 1995: Time and spatial variations of mesoscale rainfalls and their relation to the large-scale filed in the western tropical Pacific. *J. Meteor. Soc. Japan*, **73**, 379-391.

Velden, C. S. and J. A. Young, 1994: Satellite Observations during TOGA COARE: Large-scale descriptive overview. *Mon. Wea. Rev.*, **122**, 2426-2441.

Vincent, D. G. and J. M Schrage, 1994: Climatology of the TOGA COARE and adjacent regions (1985-1900). Vol. 1: Kinematic variables. Department of Earth and Atmospheric Sciences, Purdue University, West Lafayette, IN 47907, 104 pp.

Vincent, D. G. and J. M. Schrage, 1994: Climatology of the TOGA COARE and adjacent regions (1985-1900). Vol. 2: Thermodynamic and moisture variables. Department of Earth and Atmospheric Sciences, Purdue University, West Layette, IN 47907, 123 pp.

Webster, P. J. and R. A. Houze, Jr., 1991: The Equatorial Mesoscale Experiment (EMEX): An overview. *Bull. Amer. Meteor.* **72**, 1481-1505.

Webster, P. J. and R. Lukas, 1992: TOGA COARE: The coupled ocean-atmosphere response experiment. *Bull. Amer. Meteor.*, **73**, 1377-1417.

Webster, P. J., and G. L. Stephens: 1980: Tropical upper-tropospheric extended clouds: Inferences from winter MONEX, *J. Atmos. Sci.*, **37**, 1521-1541.

Weller, R. A. and S. P. Anderson, 1995: Surface meteorology and air-sea fluxes in the western equatorial Pacific during the TOGA Couple Ocean Atmosphere Response Experiment. Submitted to *J. Climate.*

Weisman, M. L. and J. B. Klemp, 1982: The dependence of numerically simulated convective storms in vertical wind shear and buoyancy. *Mon. Wea. Rev.*, **110**, 504-520.

Wilheit, T. T., A. T. C. Chang, M. S. V. Rao, E. B. Rodgers, and J. S. Theon, 1977: A satellite technique for quantitatively mapping rainfall rates over the oceans. *J. Appl. Meteor.*, **16**, 551-560.

Williams, E. R., S. G. Geotis, N. Renno, S. A. Rutledge, E. Rasmussen, and T. Rickenbach, 1992: A radar and electrical study of tropical "hot towers." *J. Atmos. Sci.*, **49**, 1386-1395.

Willis, P. T., R. A. Black, R. D Marks, Jr., and D. Baumgardner, 1995: Airborne rain drop size distributions in TOGA COARE. Preprint volume, *21st Conf. on Hurricanes and Tropical Meteorology*. Amer. Meteor. Soc., Miami, Florida, 431-433.

Wong, T., G. L. Stephens, and P. W. Stackhouse, Jr., 1993: The radiative budgets of a tropical mesoscale convective system during the EMEX-STEP-AMEX experiment. Part II: Model results. *J. Geophys. Res.*, **98**, 8695-8711.

Wyrtki, K., 1982: The southern oscillation, ocean-atmosphere interaction, and El Niño. *Marine Technol. Soc. J.*, **16**, 3-10.

Yanai, M. S. Esbensen, and J. H. Chu, 1973: Determination of bulk properties of tropical cloud clusters from large-scale heat and moisture budgets. *J. Atmos. Sci.*, **30**, 611-627.

Yoneyama, K. and T. Fujitani, 1995: The behavior of dry westerly air associated with convection observed during the TOGA-COARE R/V Natsushima cruise. *J. Meteor. Soc. Japan*, **73**, 291-304.

Yuter, S. E. and R. A. Houze, Jr., 1995: Three-dimensional kinematic and microphysical evolution of Florida cumulonimbus, Part II: Frequency distributions of vertical velocity, reflectivity and differential reflectivity. *Mon. Wea. Rev.*, **123**, 1941-1963.

Zipser, E. J., 1994: Deep cumulonimbus cloud systems in the tropics with and without lightning. *Mon. Wea. Rev.*, **122**, 1837-1851.

Zipser, E. J. and M. A. LeMone, 1980: Cumulonimbus vertical velocity events in GATE. Part II: Synthesis and model core structure. *J. Atmos. Sci.*, **37**, 2458-2469.

Zipser, E. J. and K. R. Lutz, 1994: The vertical profile of radar reflectivity of convective cells: a strong indicator of storm intensity and lightning probability? *Mon. Wea. Rev.*, **112**, 1751-1759.

Appendix A

PARTITIONING RADAR ECHO INTO CONVECTIVE AND STRATIFORM COMPONENTS

The basis for the partitioning algorithm developed herein was first presented by Churchill and Houze (1984), who partitioned gridded radar-derived rainfall rates at an altitude of 3 km into convective and stratiform components based on horizontal gradients of rainfall rate. In that study, grid points having a rainfall rate at least twice as high as the average taken over the surrounding 400 km^2 were identified as convective cores. For each identified core, the surrounding 150 km^2 was also considered convective. Furthermore, any radar echo in excess of 40 dBZ was also identified as a convective core. One drawback to this approach is that rainfall rates must be computed before any partitioning is performed. However, there is a growing body of evidence to suggest that convective and stratiform precipitation should be characterized by separate reflectivity-rainfall rate (Z-R) relationships (i.e., Thiele *et al.*, 1994; Willis *et al.*, 1995) where a given reflectivity value will produce a rainfall rate in convective precipitation that is nearly double that that would be computed for stratiform precipitation.

Steiner and Houze (1993; hereafter SH93) adapted the Churchill and Houze partitioning algorithm to gridded reflectivity data, so that once a volume was partitioned, separate Z-R relationships could be applied to the data if their use was deemed appropriate. The modification essentially consisted of specifying a reflectivity difference threshold of 4.5 dBZ—which corresponds to approximately a factor of 2 rainfall rate difference—between the grid point in question and the mean background reflectivity value. Therefore, once the radar data were interpolated to a Cartesian grid, the algorithm systematically scanned every data point to determine if it was a local maximum. If a local maximum, the (linear) mean reflectivity of all the data points within the background area was computed (the local maxima was excluded from the calculation). If the reflectivity difference between the point being tested and the mean

background reflectivity exceeded 4.5 dBZ, the point in question as well as all points lying within the specified convective area were tagged as being convective. Steiner and Houze further utilized the partitioned radar dataset by extrapolating the 3 km convective and stratiform echo areas vertically and compiled mean reflectivity profiles of each precipitation type.

After the SH93 algorithm was applied to several volumes of radar data collected during COARE and a few volumes from the PRE-STORM project for which dual-Doppler analyzed winds were available, several low-level CAPPIs and vertical cross sections from a variety of convective situations were examined in an effort to assess its performance. While the algorithm performed quite well overall, it was felt that the algorithm could be improved in two ways. First, the algorithm frequently misclassified smaller and/or weaker convective elements as stratiform when those elements were within the background radius of a more intense convective cell. Second, for convection that was tilted by wind shear, extrapolating near-surface convective areas throughout the troposphere resulted in "clipping" convective echo at higher altitudes, so that it was classified as stratiform.

Two modifications to the SH93 algorithm were implemented to address these shortcomings. First, the background area was modified to exclude those points that would lie in the convective area surrounding a potential convective core. This modification effectively "masked" the presence of nearby intense convective elements from the background reflectivity computation and allowed more weaker and areally smaller convective cells to be included in the convective partition. This modification is depicted schematically in Fig. A.1.

The second modification to the SH93 algorithm involved adapting it to operate at all vertical levels of a radar volume, and not just at a level located near the surface. This adaptation required two modifications to the convective test criteria: 1) because reflectivity decreases with height, but at different rates for different conditions, an absolute threshold of 40 dBZ was no longer appropriate for an "absolutely" convective test, and 2) because the index of refraction for ice is so much lower than it is for water, the threshold for the background reflectivity difference had to be decreased above the melting level.

The first adaptation was accomplished by using the statistical distribution of radar reflectivity in a volume to determine the "absolutely" convective threshold. As was illustrated in Yuter and Houze (1995), volumetric distributions of radar reflectivity are more broad for volumes characterized by a large number of convective cells than for volumes consisting of primarily stratiform echo. In each case, however, provided that at least some convective echo is present, the highest reflectivities at any given altitude are associated with convective cells. The absolute convective threshold, therefore, can be derived from the statistical distribution of echo in a volume. Selection of this absolutely convective threshold was accomplished by first constructing a contoured frequency by altitude diagram (CFAD; Yuter and Houze 1995) of radar reflectivity for each volume. Reflectivity values corresponding to frequency contours at the high end of the reflectivity scale at each vertical level were tested to determine which frequency resulted in the most satisfying and consistent partitioning of echo. An example of such a CFAD is illustrated in Fig. A.2. Subjective assessment of many volumes and cross sections (as well as distributions of dual-Doppler derived vertical velocity distributions) led to the selection of the upper 2% frequency contour as the absolute convective echo threshold.

The width of radar reflectivity distributions, and therefore the horizontal gradient of reflectivity, above the freezing level decreases compared to that below the freezing level, primarily due to the decrease in the refractive index of ice compared to that of water. It was therefore necessary to reduce the background reflectivity difference threshold for those local maxima that did not pass the absolutely convective test, since not doing so would result in a drastic and unrealistic decrease in convective area above the freezing level and an unrealistically large population of convective cells that terminated at the freezing level. The background reflectivity difference threshold above the freezing level was determined by adjusting the difference to eliminate large decreases in convective feature widths when cross sections of convective only (i.e., partitioned) echo were examined. Based on examination of several cross sections from several different convective situations, it was determined that the background reflectivity difference threshold should be reduced to 2.5 dBZ above the freezing level. The steps performed in the modified partitioning algorithm are presented schematically in Fig. A.3.

It should be noted that the subjective judgments made in developing this algorithm are no more frequent or common than those employed in any of the above-mentioned algorithms. Some authors (i.e., Steiner and Houze, 1993; Steiner *et al.*, 1995) refer to these algorithms as "objective" techniques for partitioning radar echo into convective and stratiform components, but in reality, *such algorithms are merely an objective application of subjective impressions.*

It is possible, however, to perform at least partly objective tests on the performance of various algorithms. Using the basic definition of startiform rainfall described in Steiner *et al.* (1995) (i.e., $v_t \gg |w|$), the algorithm was evaluated based on the width of the distribution of stratiform vertical velocities. In other words, the narrower the distribution of stratiform vertical velocities, the better the algorithm was performing. Fig. A.4 presents CFADs of stratiform vertical velocity for the SH93 algorithm and the revised algorithm described herein. The improved algorithm both reduces the width of the envelope of vertical velocities (width of the 0.1% frequency contour), as well as the distribution width for the bulk of data points, as indicated by the 5% frequency contour. The greatest improvement is seen at upper levels where convection that has been tilted by shear is properly classified as convective, therefore eliminating those large vertical velocities from the stratiform partition.

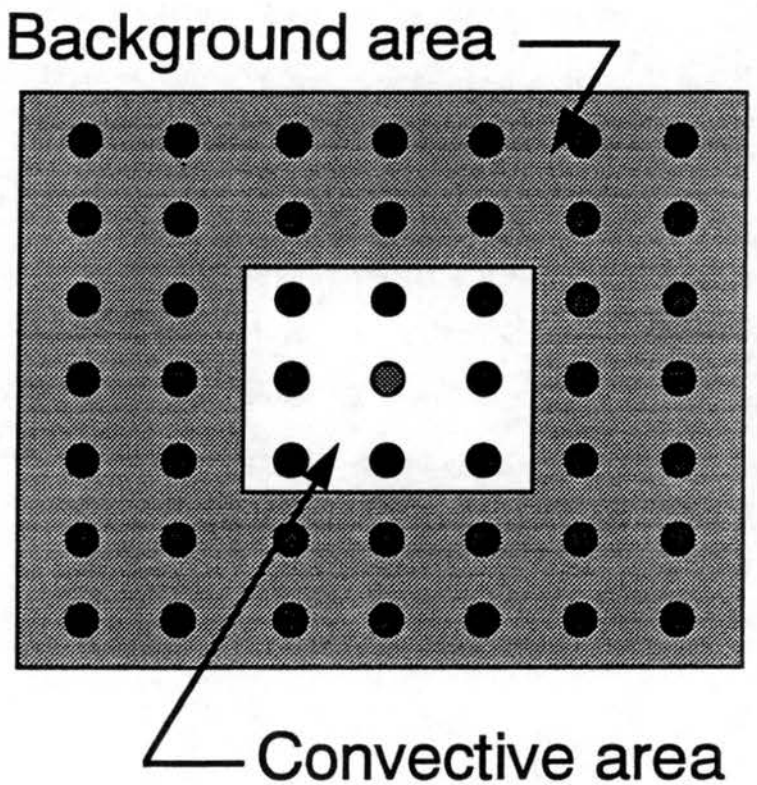

Fig. A.1 Schematic illustration of the geometry used for testing whether a gridded reflectivity value should be classified as convective or stratiform. The point in question, located in the center of the white convective area is compared to the (linear) mean reflectivity of all points within the gray background area. If the reflectivity difference between the point being tested and the mean background reflectivity is $\geq$ 4.5 dBZ ($\geq$ 2.5 dBZ above the freezing level), then the point and all of those within the convective area are tagged as convective. Background area dimensions are 22×22 km^2 and the convective area dimensions are 10×10 km^2.

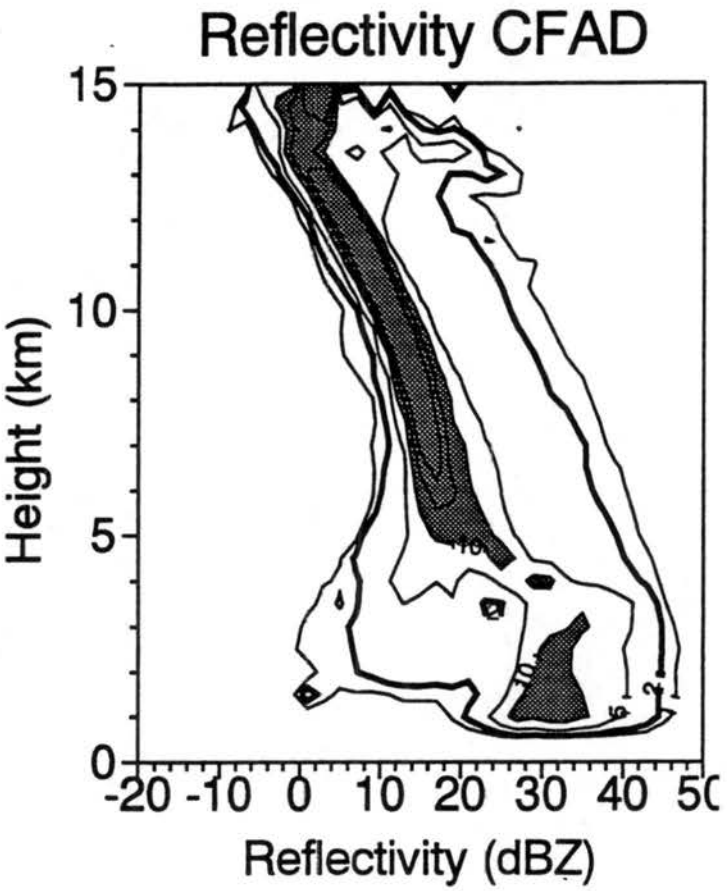

Fig. A.2 Contoured frequency by altitude diagram (CFAD) of radar reflectivity for the 1140 UTC 28 May 1985 PRE-STORM volume. The "absolute" convective threshold varies with height and is determined by the location of rightmost 2% frequency contour, indicated by the heavy line. Relative frequencies greater than 10% are shaded.

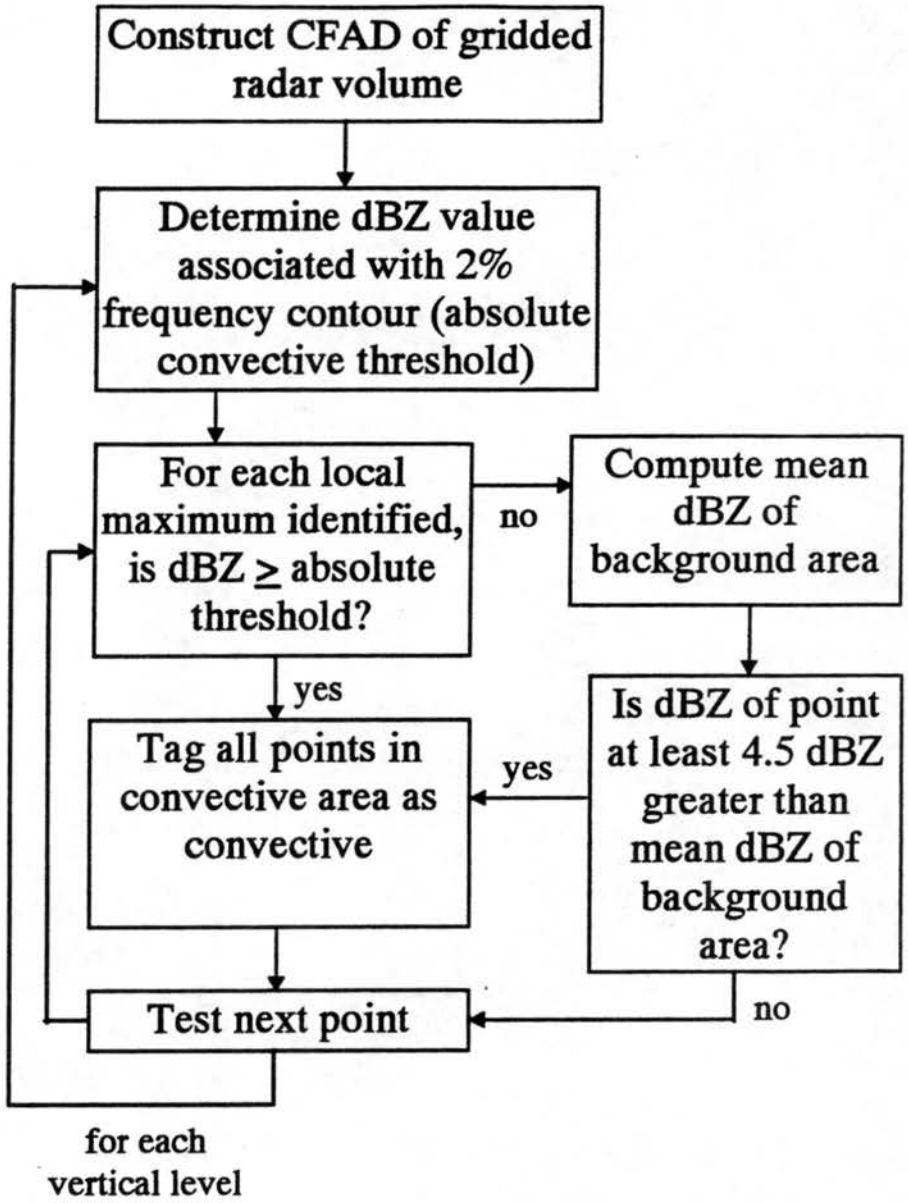

Fig. A.3 Flow chart illustration of algorithm for partitioning gridded radar data into convective and stratiform components.

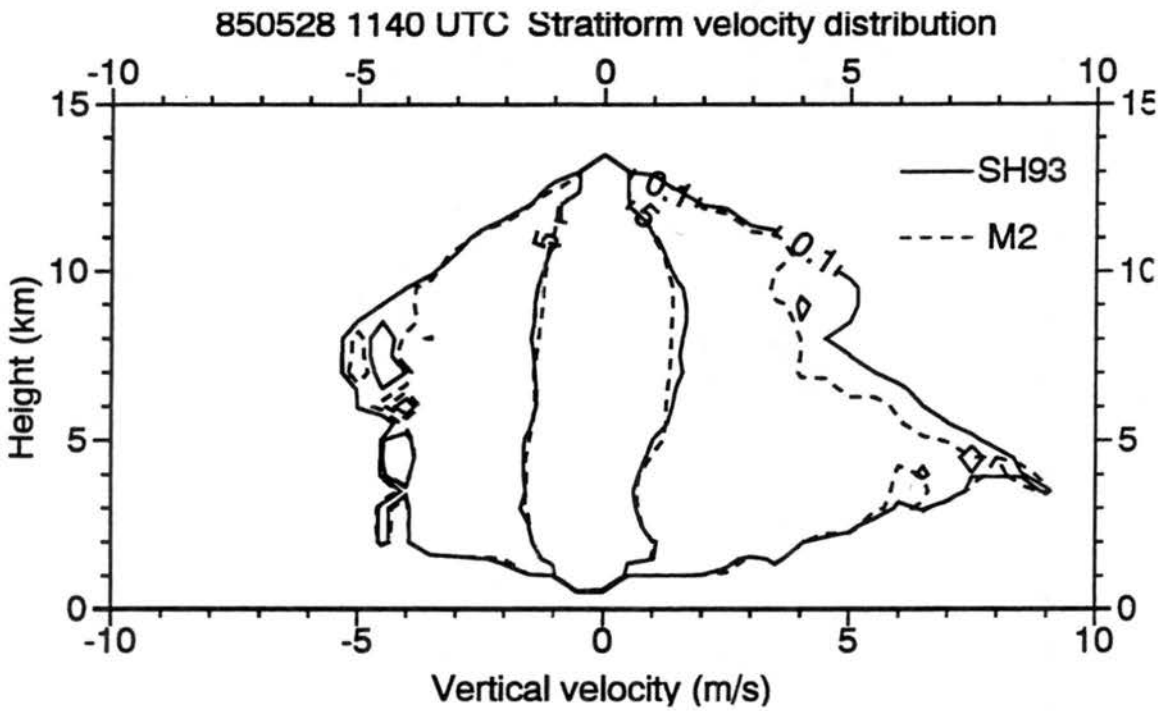

Fig. A.4 CFAD of stratiform vertical velocities as determined by SH93 (solid line) and the modified algorithm described herein (dotted line). The 0.1% and 5% frequencies are contoured.